

**A Study of Deformation in Metal Matrix Composites
at Room- and Elevated Temperature Using Neutron Diffraction**

by

Christian Lund

S.B., Massachusetts Institute of Technology (1996)

Submitted to the Department of Materials Science and Engineering
in Partial Fulfillment of the Requirements for the Degree of

Master of Science

at the

MASSACHUSETTS INSTITUTE OF TECHNOLOGY

February 1997

Copyright 1997 Massachusetts Institute of Technology. All rights reserved.

Signature of Author
Department of Materials Science and Engineering, January 17, 1997

Certified by
Professor David C. Dunand
AMAX Associate Professor of Materials Engineering
Thesis Supervisor

Accepted by
Professor Linn W. Hobbs
John F. Elliott Professor of Materials
Chairman, Departmental Committee on Graduate Students

MASSACHUSETTS INSTITUTE
OF TECHNOLOGY

JUN 16 1997 Science 1

LIBRARIES

**A Study of Deformation in Metal Matrix Composites
at Room- and Elevated Temperature Using Neutron Diffraction**

by

Christian Lund

Submitted to the Department of Materials Science and Engineering
on January 17, 1997 in Partial Fulfillment of the Requirements for the Degree
of Master of Science in Materials Science and Engineering

ABSTRACT

A metal matrix composite consisting of pure copper reinforced with 15% pure molybdenum particles by volume, was fabricated from powders using hot isostatic pressing. The microstructure of this material was investigated using optical metallography, showing some particle clustering but few voids. Conventional mechanical testing yielded stress-strain curves showing significant strengthening compared to unreinforced copper. Neutron diffraction experiments were carried out during in-situ loading of the composite at room temperature and at 300 and 350°C. At elevated temperature the neutron diffraction measurement was conducted during in-situ creep testing at constant applied stress. Elastic phase strains obtained yielded unique information on the load sharing and load transfer characteristics in the composite. Efficient elastic as well as plastic load transfer was seen at room temperature. At elevated temperature the plastic load transfer is reduced significantly. The composite exhibits high stress exponents (13-14) and activation energy (183-243 kJ/mol). The stress exponents are not reduced significantly when the applied stress is substituted with the matrix phase stress, thus indicating that the high values are caused by the matrix properties and not load transfer. Numerical modeling using finite element analysis provides good agreement with axial phase strains at room and elevated temperature. Some discrepancies may have been caused by the idealization of the microstructure by the finite element mesh. The strengthening in the composite is significantly underpredicted by the model. The most likely cause of the additional strengthening is a distribution of molybdenum precipitates in the matrix caused by a slight solubility in copper at the processing temperature.

Thesis Supervisor: Dr. David C. Dunand

Title: AMAX Associate Professor of Materials Engineering

CONTENTS

LIST OF FIGURES	5
LIST OF TABLES	7
ACKNOWLEDGMENTS	8
1. INTRODUCTION	9
2. BACKGROUND	12
2.1 Creep in Metal Matrix Composites	12
2.1.1 Metal Matrix Composites	12
2.1.2 Creep	15
2.1.3 Previous Work on Creep in Metal Matrix Composites	19
2.1.3.1 Experimental Studies	19
2.1.3.2 Analytic Studies	22
2.1.3.3 Finite Element Analysis	23
2.1.3.4 Summary of Previous Work	25
2.2 Characterization of Residual Stress in Composites Using Neutron Diffraction	26
2.2.1 Measuring Strain Using Neutron Diffraction.....	26
2.2.2 Measuring Internal Phase Stresses in Metal Matrix Composites Using Neutron Diffraction	30
3. EXPERIMENTAL PROCEDURE	34
3.1 Materials, Processing, and Microstructure	34
3.1.1 Materials System	34
3.1.2 Sample Fabrication	36
3.1.3 Metallography	37
3.2 Description of Apparatus.....	38
3.2.1 Facility.....	38
3.2.2 Instrument.....	38
3.2.3 Heating System.....	40
3.3 Description of Experiment	41
3.3.1 Room Temperature Neutron Diffraction Experiments	41
3.3.2 High Temperature Neutron Diffraction Experiments	42
3.3.3 Neutron Diffraction Data Analysis.....	44
3.3.4 Conventional Mechanical Testing at Room Temperature	45
3.3.5 Conventional Creep Testing	45

4. EXPERIMENTAL RESULTS.....	62
4.1 Room Temperature Experiments.....	62
4.1.1 Macroscopic Properties from Conventional Mechanical Testing	62
4.1.2 Microscopic Properties from Neutron Diffraction Experiments.....	62
4.2 High Temperature Experiments.....	64
4.2.1 Macroscopic Creep Properties Obtained During Neutron Diffraction Experiments.....	64
4.2.2 Microscopic Properties from Neutron Diffraction Experiments.....	65
4.2.3 Macroscopic Properties from Conventional Creep Testing	67
5. NUMERICAL MODELING	88
5.1 Description of Finite Element Model.....	88
5.2 Comparison of Finite Element Model and Experimental Results	89
6. DISCUSSION	104
6.1 Room Temperature Behavior.....	104
6.1.1 Macroscopic Behavior.....	104
6.1.2 Microscopic Behavior.....	107
6.2 High Temperature Behavior.....	108
6.2.1 Macroscopic Behavior.....	108
6.2.2 Microscopic Behavior.....	111
7. CONCLUSION.....	117
8. SUGGESTIONS FOR FUTURE WORK.....	119
Appendix 1: Determining the Steady-State Creep Stress Exponent and the Activation Energy.....	120
Appendix 2: Calculation of Critical Strain for Power Law Breakdown.....	121
Appendix 3: Creep Curves Collected During Neutron Diffraction Experiments.....	122
Appendix 4: Creep Curves from Conventional Creep Testing.....	127
Appendix 5: Experimental Data Tables	132
BIBLIOGRAPHY	135

LIST OF FIGURES:

2.1	Schematic creep curve	33
3.1	Cu-Mo phase diagram	47
3.2	Photograph of empty and fully densified HIP cans	48
3.3	Photograph of fully densified HIP cans	48
3.4	Sample dimensions	49
3.5	Micrograph, 1 cm = 50 μ m	50
3.6	Micrograph, 1 cm = 20 μ m	50
3.7	Beam interaction with sample and position of detectors	51
3.8	Photograph of stress rig	52
3.9	Technical drawing of stress rig	53
3.10	Photograph of lose-up view of heaters and sample	54
3.11	Photograph of heat shields mounted on stress rig	55
3.12	Schematic of constant-load creep testing apparatus	56
3.13	Schematic of extensometer arrangement	56
3.14	Schematic of data acquisition system	57
3.15	Neutron diffraction pattern	58
4.1	Applied stress vs. macroscopic sample strain for pure Cu and Cu-15%Mo	69
4.2a	Applied stress vs. axial elastic phase strain for Cu-15%Mo at room temperature	70
4.2b	Applied stress vs. axial elastic phase strain for Cu-15%Mo at room temperature, showing two separate experiment cycles	71
4.3a	Applied stress vs. transverse elastic phase strain for Cu-15%Mo at room temperature	72
4.3b	Applied stress vs. transverse elastic phase strain for Cu-15%Mo at room temperature, showing two separate experiment cycles	73
4.4	Steady-state creep strain rate vs. applied stress for data collected during neutron diffraction	74
4.5	Applied stress vs. axial elastic phase strain for Cu-15%Mo at 300°C ..	75
4.6	Applied stress vs. transverse elastic phase strain for Cu-15%Mo at 300°C	76
4.7	Applied stress vs. axial elastic phase strain for Cu-15%Mo at 350°C ...	77
4.8	Applied stress vs. transverse elastic phase strain for Cu-15%Mo at 350°C	78
4.9	Applied stress vs. axial elastic phase stress at room temperature and at 300°C	79
4.10	Applied stress vs. axial elastic phase stress at 300°C and 350°C	80
4.11	Applied stress vs. transverse elastic phase stress at room temperature and at 300°C	81
4.12	Applied stress vs. transverse elastic phase stress at 300°C and 350°C .	82
4.13	Creep data at 300°C for conventional testing and from neutron diffraction experiments	83
4.13	Creep data at 350°C for conventional testing and from neutron diffraction experiments	83

4.15	Creep data at 300°C for conventional testing of composite and theoretical values for pure Cu	84
4.16	Creep data at 350°C for conventional testing of composite and theoretical values for pure Cu	84
4.17	Plot of strain verse inverse absolute temperature, yielding activation energies	85
5.1	Two-dimensional axisymmetric finite element mesh	92
5.2	Numerical prediction and experimental results of room temperature stress-strain behavior	93
5.3	Numerical prediction and experimental results of axial elastic phase strains at room temperature	94
5.4	Numerical prediction and experimental results of transverse elastic phase strains at room temperature	95
5.5	Numerical prediction and experimental results of axial elastic phase strains at 300°C	96
5.6	Numerical prediction and experimental results of transverse elastic phase strains at 300°C	97
5.7	Numerical prediction and experimental results of axial elastic phase strains at 350°C	98
5.8	Numerical prediction and experimental results of transverse elastic phase strains at 350°C	99
6.1	Ellingham diagram showing the standard free energy of formation of selected oxides.....	113
6.2	Deformation-mechanism map for pure copper of grain size 0.1 mm.....	114
6.3	Applied stress vs. copper matrix phase stresses at elevated temperature	115
6.4	Strain rate vs. applied stress at 300°C showing a reduced stress exponent by omitting high stress levels.....	115
6.5	Strain rate vs. copper matrix phase stress at 300°C.....	116
6.6	Strain rate vs. copper matrix phase stress at 350°C.....	116

LIST OF TABLES:

3.1	Properties of the Pure Metals Cu and Mo from Literature.....	59
3.2	Targeted Loads, Mean Loads, and Elapsed Times for Room Temperature Neutron Experiments	60
3.3	Temperatures, Applied Loads, Elapsed Times and Sample Numbers for High Temperature Neutron Experiments.....	61
4.1	Room Temperature Mechanical Properties of Cu and Cu15%Mo	86
4.2	Changes in Elastic Modulus with Temperature and Experimental Errors	86
4.3	Creep properties of Cu and Mo	87
5.1	Materials Properties Used in Finite Element Model	100

ACKNOWLEDGMENTS

I would like to express my sincerest appreciation to Prof. David C. Dunand, my thesis advisor, for giving me freedom in defining the topic of this thesis, for strongly supporting me in my endeavors, and for providing me with challenge and inspiration. His advice and knowledge has helped me improve my understanding of the topics involved.

My deepest appreciation goes to Dr. Mark A. Bourke, my internship supervisor at the Manuel Lujan Jr. Neutron Scattering Center (MLNSC) at the Los Alamos National Laboratory. His advice and experimental expertise were invaluable in conducting the neutron diffraction experiments and evaluating the results.

Dr. Christian Verdon helped with conducting the conventional creep testing, and performed TEM experiments. I am most sincerely grateful for drawing upon his time and expertise. I am also indebted to T.A. Venkatesh, for preparing equipment for these tests. Dr. Ann Jansen was also very helpful in sharing her experiences in creep testing.

I would also like to thank Dr. Mark Daymond and Guiru Liu-Nash, for assisting in conducting the numerical modeling associated with this thesis. Dr. Daymond's advice regarding the execution of the neutron diffraction experiments was also much appreciated.

I would also like thank the other members of my research group at MLNSC for providing advice and being such great friends. I am also grateful for the support from the members of the Dunand research group.

I am deeply grateful for all the help I received from the MLNSC mechanical and electrical teams in preparing my neutron diffraction experiments. I especially would like to mention Mike McCormick, Ross Sanchez, John Sandoval, and Rudy Valdez.

Last but not least I would like to thank my parents, Unni and Sverre Lund; my sister Elisabeth; and Gwen Crevensten; for doing more than anyone to keep me motivated.

1. INTRODUCTION

The strong interest in MMCs is largely due to the promise of this materials group to provide enhanced mechanical properties as compared to the unreinforced material. By incorporating a high strength reinforcement into a ductile alloy matrix, a combination of properties may be achieved. The reinforcement provides strength and stiffness while the matrix provides the ductility often lacking from the high strength reinforcement in question. Another attractive aspect of a composite material is the ability to choose constituents and their proportions so as to tailor the overall properties of the composite, e.g. electrical, thermal or wear properties.

Particulate reinforced metal matrix composites offer cost advantages over continuous fiber and whisker reinforced metal matrix composites. The cost advantage arises from the fact that most particulate metal matrix composites can be processed using conventional techniques such as casting and extrusion with only minor processing adaptations. Also their properties are more isotropic than continuous fiber reinforced MMCs. Currently, particulate reinforced composites are being developed for advanced structural applications, such as aerospace structures and engine components. As elevated temperature conditions are often encountered, the need to understand the high temperature mechanical properties of this materials group is evident. Creep is an important property in such applications, and creep-limited applications for MMCs have been identified (Davis and Allison 1995). The strength and stiffness retention of MMCs at high temperatures makes them candidates for replacing components often made out of denser materials.

Most information published so far on creep in MMCs is empirical and specific to a given MMC system (Dunand and Derby 1993). Some modeling studies have been undertaken (Dunand and Derby 1993), but the results are again relevant only to the specific system studied. There is a strong need to study fundamental phenomena associated with creep in MMCs, and thereby to obtain a more general understanding of creep mechanisms in these materials systems.

Neutron diffraction is a unique experimental tool available to materials scientists. Among other things, it allows for simultaneous characterization of stresses in each phase in multiphase materials during in-situ loading. For composite systems, load sharing and subsequently load transfer characteristics can be studied with this technique.

In the present study, neutron diffraction was used to characterize these phenomena in a copper-molybdenum composite, during both room temperature static loading and high temperature creep. The neutron diffraction experiments were supplemented by conventional room temperature mechanical testing, and by high temperature creep experiments to yield overall macroscopic properties. Structural characterization was performed using optical metallography. Numerical modeling provided predictions for overall macroscopic properties as well as microscopic phase properties.

The next chapter (Chapter 2) reviews creep in metal matrix composites. The use of neutron diffraction to characterize internal stresses in materials is also presented, along with a literature survey of previous work on determining internal stresses in MMCs using this technique. The next two chapters (Chapters 3 and 4) present experimental procedure and results,

respectively. The numerical model and its results are then presented and compared with the experimental data in Chapter 5. Chapter 6 provides a discussion of the results. Chapter 7 summarizes the findings and finally Chapter 8 provides suggestions for future work.

2. BACKGROUND

2.1. Creep in Metal Matrix Composites

2.1.1. Metal Matrix Composites

The development of metal matrix composites has been motivated by the enhancement of mechanical properties offered by the composite in comparison with the unreinforced matrix material. The principal benefits of MMCs over the unreinforced alloy include increased strength and stiffness per unit density, leading to enhanced performance and reduced structural weight; and a decrease in the coefficient of thermal expansion (CTE), reducing thermal strains in thermal cycling applications. Some systems also exhibit increased wear resistance due to the presence of the ceramic reinforcement. MMCs with lightweight matrix alloys such as aluminum provide increased thermal and electrical conductivity and enhanced corrosion resistance as compared to the ferrous alloys they often seek to replace. Furthermore, one attribute of a composite material is the ability to vary the composition of the composite in order to tailor the properties to meet the requirements for a specific application.

Reinforcements in MMCs have a higher specific strength and stiffness than the metallic matrix, thus resulting in composite strengthening at low temperatures. The reinforcement melting temperatures are higher, and their coefficients of thermal expansion are lower, thus implying that for a given operating temperature the reinforcement will be at a lower homologous temperature than the metallic matrix. Thus at elevated temperatures the reinforcement will creep at a lower rate than the matrix. Thus composite

strengthening at elevated temperatures may be attributed to the increased creep resistance of the reinforcement.

Residual stresses are inherent in most MMCs (Bourke et al 1993). The residual stresses arise most often from the differences in coefficients of thermal expansion (CTE) of the matrix and the reinforcement. Due to the high temperatures, often 1000°C or higher, experienced in the processing of MMCs, the thermal expansion mismatch can induce large stresses upon cooling to room temperature. Since the reinforcement most often is a ceramic with a much higher melting point than the matrix, its CTE will be smaller than that of the matrix. Consequently, upon cooling, the matrix will contract more than the reinforcement, resulting in a tensile stress in the matrix and a compressive stress in the reinforcement, if there is good interface bonding. In a service or test situation this stress will be additive to the applied stress. For example, as the composite is put in tension, the matrix phase stress will be higher than the applied stress. The matrix may therefore yield before the applied stress reaches the expected yield stress. In some cases the matrix will have a thermal residual stress large enough to induce matrix micro-yielding even when unloaded.

Most MMC applications are in the automobile and aerospace industries (Koczak et al. 1993). Current and potential automotive applications include brake components, drive shafts, engine block components, connecting rods, and pistons. Aerospace applications include helicopter rotor components, turbine engine components, and landing gear component (Koczak et al. 1993). A wide range of applications in the sporting goods, biotechnology and nuclear industries have also been found. Particulate reinforced aluminum is currently being used in high performance mountain bike frames and golf club

heads (Koczak et al. 1993). In the marine/fishing industry, winch catheads also made out of particulate reinforced aluminum are available commercially (Sørheim 1994).

Load sharing between the matrix and the reinforcing phase is a key concept in the study of the mechanical behavior of composites. The volume average of the load in each phase indicates the proportion of the total applied load carried by each phase. The weighted sum of the volume averaged loads in each phase must at any time, given equilibrium, be equal to the applied load.

In the elastic regime, the proportion of the load carried by each phase, the load partitioning, remains the same. The load partitioning is known to be influenced by volume fraction reinforcement, shape and orientation of the reinforcement, and on the elastic properties of the two phases in the composite (Clyne and Withers 1993).

An efficient composite material is designed to have the reinforcement carrying a large proportion of the applied load. As the term "reinforcement" implies, this phase is usually stronger and stiffer than the matrix, and naturally is capable of carrying much higher loads than the matrix.

The origin of strengthening is usually attributed to two main factors. First, the introduction of a reinforcing phase may cause in-situ strengthening of the matrix. Second, load transfer from the matrix to the reinforcing phase will cause strengthening of the composite provided that an appropriate reinforcing phase is chosen.

Metallurgical theory and microstructural evaluation may be used to explain the matrix in-situ strengthening. This strengthening is often caused

by work-hardening due to the induction of dislocations from the addition of the second phase.

The Eshelby technique is a numerical technique for the prediction of load partitioning and transfer in two-phase materials (Clyne and Withers 1993). Finite element analysis can often provide numerical predictions for load transfer in composite materials. Diffraction techniques are used to measure the elastic strains in each phase. From the elastic strains, the load partitioning may be inferred. Using diffraction during in-situ loading, the strain evolution may be deduced and the load transfer can be characterized (Bourke et al. 1993).

When the phase stress in the matrix reaches the point where the matrix starts to yield, the ability of the matrix to carry load is reduced dramatically. The reinforcement now has to carry a higher proportion of the load. A curve of applied stress versus phase stress will be linear until the matrix microyield is reached. At this point, the curve will kink and no longer be linear. The reinforcement phase stress will increase more rapidly than before and the matrix phase stress less rapidly than before (Clyne and Withers 1993).

2.1.2. Creep

Creep is by definition time-dependent deformation under load. Due to the fact that the deformation mechanisms for creep are thermally activated, creep is typically only evident at elevated temperatures. In most metals this corresponds to an absolute temperature of 30 - 40% of the melting point.

The evolution of creep strain with time, under constant load, generally

takes the shape of the curve shown in Figure 2.1. Three stages are identified. Stage I, or primary creep, is an initial stage during which creep rates are high, but decreasing. During stage II, or secondary or steady state, the creep rate is constant. Finally, during stage III, or tertiary or breakdown, strain rates are increasing, eventually leading to failure. The stages may have different durations depending on the materials system. Some systems do exhibit a very short steady state regime, actually so short that it is more appropriate to use the term minimum rather than steady state creep rate. (Clyne & Withers 1993).

Three basic agents of deformation can be identified. There is dislocation glide, dislocation climb and vacancy creep. Dislocation glide signifies plastic deformation. Dislocation climb can be either controlled by the vacancy motion along a core of dislocation, or by the motion of dislocation through the lattice. Vacancy creep is a diffusional process in which the motion of vacancies account for deformation, and is either controlled by diffusion along grain boundaries or diffusion through the bulk.

When dislocation climb is the dominant deformation mechanism, the strain rate is observed to obey by the following relationship:

$$\dot{\gamma} = AD_{\text{eff}} \frac{\mu b}{kT} \left(\frac{\sigma_s}{\mu} \right)^n \quad (1)$$

where $\dot{\gamma}$ is the shear strain rate, A is a constant, μ is the shear modulus, b is the Burger's vector, k is the Boltzmann constant, T is the absolute temperature, σ_s is the shear stress, and n is the stress exponent. D_{eff} the effective diffusion coefficient and is given by the following relationship:

$$D_{\text{eff}} = D_v \left[1 + \frac{10a_c}{b^2} \left(\frac{\sigma_s}{\mu} \right)^2 \frac{D_c}{D_v} \right] \quad (2)$$

where a_c is the cross-sectional area of the dislocation core, D_c is the core diffusion coefficient, and D_v is the volume diffusion coefficient. At high temperature, volume diffusion is dominant, while at low temperature, core diffusion is dominant. Thus at low temperature, the stress exponent is no longer n , but $n+2$. Theoretical arguments have predicted stress exponents of 3 or 4 (Clyne and Withers 1993), but much higher stress exponents are often observed.

Under low applied stresses, dislocation mobility is reduced and consequently dislocation climb becomes very slow. Vacancy creep now becomes the dominant mechanism. Mass transport by the diffusion of vacancies thereby becomes the agent of deformation. Vacancies may either diffuse along grain boundaries or through the volume. If both diffusion routes are permitted, the following rate equation for diffusional flow may be developed:

$$\dot{\gamma} = D_{\text{eff}} \frac{42\sigma_s\Omega}{kTd^2} \quad (3)$$

where d is the grain size, and Ω is the atomic volume. D_{eff} is now given by

$$D_{\text{eff}} = D_v \left[1 + \frac{\pi\delta D_b}{dD_v} \right] \quad (4)$$

where D_b is the grain boundary diffusion coefficient, and d is the effective thickness of the grain boundary. As with power-law rate equations, two

different regimes can be identified. In a high temperature regime, known as Nabarro-Herring creep, volume diffusion is dominant. In a low temperature regime, known as Coble creep, grain boundary diffusion becomes dominant. Thus at high temperature, the strain rate is proportional to D_v/d^2 , whereas at low temperature it is proportional to D_b/d^3 (Frost & Ashby 1982).

At high stresses, the power law relation no longer holds. The measured strain rates become larger than predicted by Eqn. 1. This regime is called power law breakdown, and is evidence of a transition from climb-controlled to glide-controlled flow (Frost and Ashby 1982). Empirical description of the breakdown phenomenon yield an exponential rate equation, implying that the strain rate dependence on stress is exponential rather than power law. Frost & Ashby (1982) proposes the following rate equation for power law creep and power law breakdown:

$$\dot{\gamma} = A_2 \frac{D_{\text{eff}} \mu b}{kT} \left[\sinh \left(\alpha' \frac{\sigma_s}{\mu} \right) \right]^n \quad (4b)$$

where $A_2 \alpha'^n = A_1$. At stresses below $\sigma_s \approx \mu / \alpha'$, this equation reduces to become identical to the power law equation. In other words the transition from power law creep to power law breakdown occurs when $\sigma_s \approx \mu / \alpha'$.

2.1.3. Previous Work on Creep in Metal Matrix Composites

2.1.3.1. Experimental Studies

A wide variety of systems and their creep properties have been studied. Matrix materials are usually commercial aluminum alloys. Reinforcements are most commonly carbides, such as silicon carbide (SiC) and titanium carbide (TiC); or oxides, such as alumina (Al_2O_3). Tungsten reinforced copper has also been studied, along with the model systems bronze reinforced lead and nickel reinforced lead. The following review will describe selected studies in more detail.

Mohamed et al. (1992) have provided a review of the creep data for discontinuous SiC-Al composites. They conclude that the creep behavior of these composites exhibits two main characteristics. Firstly, the stress exponent describing the stress dependence of the steady state creep rate is high and variable. Secondly, the creep activation energy, which provides a measurement of the temperature dependence of the steady state creep rate, is much larger than for the aluminum alloy matrix. Mohamed et al. (1992) finds that the creep behavior of SiC-Al composites is similar to that of dispersion strengthened alloys, as illustrated by high stress exponents and high activation energies.

Nieh (1984) studied the tensile creep behavior of SiC whisker and particle reinforced aluminum alloy 6061 between 232°C and 332°C. He reported that both composites exhibited steady state creep, indeed the data for 20% volume fraction reinforcement could be fitted to one power-law equation (Eqn. 1) with $n_c=20.5$ and $Q_c=390$ kJ/mol. When the volume fraction of particulates was increased to 30%, the same high stress exponent was

obtained. However, the creep resistance now dropped below that of the alloy reinforced with 20% whiskers. This behavior was attributed to the difference between load bearing capabilities and the relative strengths of the two types of composite reinforcement. A threshold stress was not observed.

Nieh et al. (1988) studied the creep behavior of a SiC particulate reinforced Al alloy 2124 at 20 % reinforcement by volume. The tests were performed at 350°C-450°C. Specimens were tested using a double shear configuration, yielding strains on the order of 40%; strains much higher than any of the aforementioned studies. They concluded that the creep curve of the composite exhibits a very short steady state range; a minimum creep rate, rather than a steady state creep rate, exists. The minimum creep rate depends strongly on temperature and the applied stress; the activation energy was found to be 400 kJ/mol, and the stress exponent to be about 9.5. This activation energy is almost three times that for self diffusion in aluminum.

Pickard and Derby (1989) performed creep tests on Al alloy 1100 with 20% SiC particulate reinforcement at temperatures ranging from 150°C-350°C. A high value of n equal to about 20 was found at all temperatures. No threshold stress was observed. Fracture was studied in some detail, and found to occur by necking at all temperatures. Some voids were found originating at the particle-matrix interface.

Mishra and Pandey (1990) again found a threshold stress after reanalyzing previous data by Nieh (1984) and Morimoto et al. (1988). A good fit was found using the following phenomenological equation introduced by Sherby et al. (1977):

$$\dot{\epsilon} = A'' \frac{D_L \lambda^3}{b^3} \left(\frac{\sigma - \sigma_R}{E} \right)^n \quad (5)$$

where A'' is a constant, D_L the lattice diffusivity, λ the subgrain size, b the Burgers vector length, and E Young's modulus. By substituting in the temperature dependence of D_L , Equation 5 becomes:

$$\dot{\epsilon} = A''' \frac{\lambda^3}{b^3} \left(\frac{\sigma - \sigma_R}{E} \right)^8 \exp\left(-\frac{Q}{RT}\right) \quad (6)$$

where $A''' = A'' D_{oL}$, a constant. This equation requires constant substructure and lattice diffusion controlled creep. As pointed out by Mishra and Pandey (1990), the average spacing between the reinforcements could control the subgrain size, and that the reinforcing phase could pin dislocation motion and thereby stabilize the subgrain size. They found a threshold stress that decreases with increasing temperature, thus implying that the complete temperature dependence does not appear explicitly in Equation 6. They attributed this feature to the temperature dependence of the elastic modulus.

Krajewski et al. (1993) studied the creep properties of 2219 aluminum reinforced with 15% titanium carbide (TiC) particulates by volume, in the temperature range 150°C-250°C. At the lower temperatures, reinforcement led to an increase in creep strength, whereas at the higher temperatures studied, the reinforced and the unreinforced alloy exhibited essentially identical creep behavior. The role of microstructure was studied, and it was found that the precipitate spacing in the matrix was the predominant influence on the minimum creep rate in both the reinforced and unreinforced materials. The absence of creep strengthening due to the reinforcement at the high temperatures was attributed to diffusional relaxation processes. Stress exponents ranged from 7.9 to 13.3.

2.1.3.2. Analytic Studies

Much less analytic work has been done on metal matrix composites with particulate reinforcement than with whisker or fiber reinforcement. The micromechanical modeling is much more complicated, and only recently have modeling tasks been undertaken, and then mostly by numerical means such as finite element analysis. A continuum mechanics treatment has however been attempted by Ravichandran and Seetharaman (1993).

Ravichandran and Seetharaman (1993) has developed a simple model based on continuum mechanics to predict the steady state creep rates of composites containing coarse and rigid reinforcements from the matrix creep behavior. A unit cell was idealized and simplified to a pattern of cubic inclusions uniformly distributed in a continuous creeping matrix. It was assumed that the composite creep is primarily due to the matrix while the reinforcements are considered rigid and undeformable.

Their approach is a combination of the rule of mixtures approach used for fibrous composites and the approach used to predict creep rates in transversely loaded bimaterial laminates; using the relevant isostrain rate and isostress configurations. A simple analytical equation was derived to predict the overall composite creep rate from the matrix creep behavior. The creep rate was given by the following expression:

$$\dot{\epsilon}_c = K_m \left[\frac{\sigma_c (1+c)^2}{\left(1 + \frac{0.3}{c}\right) \left(\frac{1+c}{c}\right)^{1/n_m} + (1+c)^2 - 1} \right]^{n_m} \quad (7)$$

where c is the ratio of interparticle matrix thickness to the mean particle diameter. K_m is a constant simply given by the matrix power law expression: $\dot{\epsilon}_m = K_m \sigma_m^n$, where K_m is temperature dependent. Good agreement was found with systems containing a high volume fraction of reinforcement.

2.1.3.3. Finite Element Analysis

Sørensen (1992) modeled the creep in particulate reinforced MMCs using finite element analysis. He studied the effect of reinforcement shape on creep properties such as hardening behavior, dynamic recovery and steady state creep of the matrix phase. He assumed a plane strain configuration, and the problem could therefore be analyzed in two dimensions. A square inclusion represented a unit cylinder, while a circular inclusion represented a sphere. An internal variable constitutive model was used to describe the creeping matrix. The reinforcement was assumed to be elastic and not creeping. No interfacial decohesion was allowed in the model.

The material with circular inclusions was found to give much less creep strength than a square inclusion at a given volume fraction. Sørensen (1992) proposed that as a rough estimate the volume fraction of circular inclusions would have to be twice that of the square inclusion to provide the same creep strength.

Atkins and Gibeling (1995) used a two dimensional axisymmetric unit cell finite element model to study creep in particulate reinforced MMCs. They studied the system of aluminum alloy 8009 reinforced with 11 volume percent silicon carbide. The emphasis of the investigation was the primary creep regime, as this regime was found to represent a significant portion of the overall creep strain. The inclusion of primary creep into the model did

not affect the final distribution of stresses and strains, but a significant primary creep transient was revealed by the overall creep response of the model.

Strain gradients were present in the matrix. This result contradicts the Eshelby model, which assumes uniform plastic strain fields throughout the matrix. The stress contours in the matrix indicate that strengthening occurs by load transfer from the matrix to the reinforcement via a shear stress, in correspondence with the shear-lag model, as described in Section 2.1.1. It was also found that after steady state creep is reached, the stress distribution in the matrix and the particulate reinforcement remains constant.

Davis and Allison (1995) used an axisymmetric unit cell model with spherical reinforcements to study a system based on TiC particles in a aluminum alloy 2219 matrix. They found that the steady state creep rate is independent of the particle elastic modulus and the elastic and plastic properties of the matrix, and only dependent on the matrix creep rate and the volume fraction reinforcement.

Comparisons with experimental results of the same material (Krajewski et al. 1992) found that the composite creep strengthening predicted from the finite element model is larger than measured. The continuum mechanics finite element model assumes that the properties of the matrix do not change upon the addition of a reinforcing phase. The overestimation of the creep strength by this model leads the researchers to suggest that the matrix properties do change, thereby violating this assumption. These changes could be related to microstructure, dislocation density, or creep mechanism. The presence of such changes in matrix properties is also supported by different time dependencies of the primary creep rates.

2.1.3.4. Summary of Previous Work

Systems described range from commercial aluminum alloys reinforced with ceramic materials to metal-metal systems studied primarily as ideal systems to facilitate otherwise complicated analytic and numerical modeling.

Most experimental studies are performed on reinforced aluminum alloys. In such studies, the stress exponent and the creep activation energy, are found to be very high as compared to unreinforced matrix values. However for metal-metal systems the stress exponents and activation energies are much closer to the unreinforced matrix values.

The high stress exponent has led to the introduction by some researchers of phenomenological equations incorporating a threshold stress, an approach analogous to the one devised for dispersion strengthened alloys. Most researchers have however not observed a threshold stress. Dunand and Derby (1993) suggests that this apparent threshold stress may be due to the solid state process route used in the studies reporting them. This process route is known to lead to a fine dispersion of oxide particles in the matrix, thus leading to dispersion strengthening as well as composite strengthening, the former giving rise to a threshold stress. Most metal-metal systems studied have much lower oxidation tendencies than aluminum. Such composites should not contain dispersoids due to oxidation, and accordingly a threshold stress is not observed.

Particulate reinforced composite creep has also been studied analytically in a few articles, but the results tend to be specific to a given system and less conclusive. An expression for the creep rate as a function of sphere diameter, interparticle spacing and applied stress has been derived from continuum mechanics principles, and agrees with some experimental

data. Finite element analysis indicates that cylindrical reinforcements with unity aspect ratio provide enhanced creep strength over spherical inclusions. Primary creep is also predicted to affect the overall creep response of a material. After steady state creep is reached, the stress distribution in the matrix and the particle reinforcement remains constant. Comparisons of modeling with experimental results, and the discrepancies that sometimes are evident, suggest that matrix properties in the reinforced state indeed are different from those of the unreinforced state, thus violating a basic assumption of most analytic work.

The issue of creep in discontinuously reinforced composites is very complicated and the underlying processes are not yet fully understood, although the role of some mechanisms and phenomena are understood and accepted. The variety of materials and the range of matrix-reinforcement compositions and shapes have led to much experimental data. Modeling and analytic treatments can only rarely be generalized to all or most cases involving composite creep. Further work in the discipline is driven by the need to develop models and analytic expressions from first principle that are more generally valid than those available today, and that fit a wide range of data.

2.2 Characterization of Residual Stress in Composites Using Neutron Diffraction.

2.2.1 Measuring Strain Using Neutron Diffraction

Diffraction is the technique of choice when studying residual stresses in MMCs because it allows a distinction between the strain in the matrix and the reinforcement. (Bourke et al 1993). The two principal diffraction techniques available are neutron and X-ray diffraction. Using either technique, elastic internal strains in each phase are determined by measuring changes in interatomic spacings. However the techniques differ because X-rays scatter from interaction with electrons, whereas neutrons scatter from interaction with atomic nuclei. Accordingly, X-rays have a penetrative depth several orders of magnitude less than that of neutrons. Due to its penetration characteristics, neutron diffraction is a non-destructive depth technique while X-ray diffraction is limited to surfaces and vulnerable to machining stresses and surface finishes. Largely because of its nondestructive depth capability, neutron diffraction is generally considered superior to X-ray diffraction in measuring phase strains in MMCs. Neutron diffraction was used for this experiment, and therefore the following treats only this technique.

Residual strain measurements can be made using monochromatic (single wavelength) neutrons, associated with reactor sources, or polychromatic (multiple wavelength) neutrons, associated with pulsed spallation sources. Changes in wavelength at a pulsed source can be less than 0.002 Å. Given these small changes, high resolution diffractometers are required. With the neutron intensities currently available, count times are on the order of hours. Pulsed sources have a big advantage in that they allow for the measurement of strains simultaneously in two or more directions by the appropriate positioning of the detector banks. For example, in a tensile test, axial and transverse strains can be measured.

Since crystals are symmetrical arrays of atoms organized in planes and rows of high atomic density, they act as three-dimensional diffraction gratings. For successful diffraction, the distance between atoms must be close to the wavelength of the scanning beam. When neutrons strike atoms in an array, they are scattered in all directions, but in some directions constructive interference occurs. The condition for constructive interference in crystals is known as Bragg's law,

$$n\lambda = d\sin\theta \tag{8}$$

where n is an integer, λ is the neutron wavelength, d is the lattice plane spacing, and θ is the angle of incidence or reflection of the neutron beam.

At a spallation source, neutrons are produced in pulses consisting of a continuous spectrum of energies, or wavelengths. In an experiment, the energy, or wavelength of a detected neutron is determined from its time of flight (TOF) from creation at the target to its detection following interaction with the sample. The detector is at a constant scattering angle, thus making the wavelength in Bragg's law the variable that is scanned. From the following simple relationships, it is clear that the time of flight is proportional to the wavelength. From the de Broglie relationship:

$$\lambda = \frac{h}{mv} \tag{9}$$

where λ is the neutron wavelength, h is Planck's constant, m is the neutron mass, and v is the neutron velocity; and from the kinematic relationship:

$$s = vt_{OF} \tag{10}$$

where s is the distance traveled, and t_{OF} is the time of flight of the neutron; it follows that

$$t_{OF} = \left(\frac{sm}{h} \right) \lambda \tag{11}$$

As the angle is fixed, Bragg's law can be used to find the d-spacings for wavelengths that are associated with peaks in the scan. Given the measured d-spacings, and a choice of an appropriate reference, or unstressed d-spacing, d_{REF} , strain ϵ can be determined as follows:

$$\epsilon = \frac{d - d_{REF}}{d_{REF}} \tag{12}$$

Using single peaks, strain along different lattice planes can be determined. One can also determine the lattice parameter for each run by averaging over all peak positions. This is usually done using specialized statistical analysis software. Subsequent changes in lattice parameters will yield bulk strains.

2.2.2 Measuring Internal Phase Stresses in Metal Matrix Composites Using Neutron Diffraction

Using neutron diffraction to measure internal phase strains is a fairly new technique, first appearing in the early 1980s (Krawitz and Schmank, 1982, Allen et al. 1985). Since then its use has increased dramatically. The first studies performed characterizations of residual stresses in samples without applying an external load.

Two recent studies on aluminum reinforced with silicon carbide has compared residual strains obtained by neutron diffraction with numerical predictions (Povirk et al. 1991/1992). They applied Eshelby equivalent inclusion and finite element analyses respectively. Neutron diffraction provided a method for validating the predictions of thermal residual stress and the effect of plastic deformation.

Neutron diffraction has been used to measure the evolution of elastic strain with the application of an external load. Small stress rigs are used that fit into the limited space available to neutron diffractometers in the neutron flight path. The anisotropic strains resulting from the elastic anisotropy of the different lattice planes in different orientations can be measured (Hutchings 1990, Allen et al .1988). The evolution of elastic strain in each phase can also be measured this way, and such shared-load experiments in the Al/SiC system was performed by Allen et al. (1987), and Withers et al. (1989). Recently there has been considerable interest in making measurements of strain in composites during in situ-loading at high temperatures (Bourke et al. 1993).

A wide variety of experiments studying a number of different systems confirm that upon cooling, tensile and compressive phase stresses develop in

the matrix and the reinforcement, respectively, in both the axial and transverse directions. (Bourke et al. 1993). Relaxation of residual stress during heating has also been studied using neutron diffraction (Majumdar et al. 1991). The temperature at which the residual stresses were completely relaxed was determined for a variety of systems.

Allen et al. (1987) used neutron diffraction during in-situ tensile uniaxial loading to determine the evolution of elastic strain. The materials systems used were Al/SiC whisker and particulate composites. The initial thermal stress state prior to loading was used as zero-strain state for each phase. After unloading, the axial phase strains returned to zero. However, in the transverse direction, compressive and tensile lattice strains were observed in the matrix and reinforcement, respectively. The data was compared to analytic Eshelby models.

Shi and Arsenault (1991) and Shi et al. (1992a) performed similar measurements on Al/SiC whisker composites before and after tensile loading and compressive loading. Initially, after either compressive or tensile loading, the tensile residual stress in the matrix was reduced. After applying higher loads, in the case of a tensile load, the tensile residual stress in the matrix continued dropping. However in the case of a compressive load, the tensile residual stress increased. The transverse stresses showed much less response to the axial loading conditions.

Povirk et. al (1991) and (1992) also studied the Al/SiC whisker and particulate composite systems. The initial post-fabrication residual stresses were much lower than in the materials used by Shi et al. (1991) and (1992b). Both tensile and compressive loading was undertaken. After tensile loading, the axial residual stresses in both the matrix and the reinforcement changed signs, and the matrix was therefore left in compression while the

reinforcement was in tension. In the transverse direction, the stresses were much smaller and of the opposite sign of those in the axial direction. This change of signs of the stresses was not observed after compressive loading.

Chapter 2 Figures

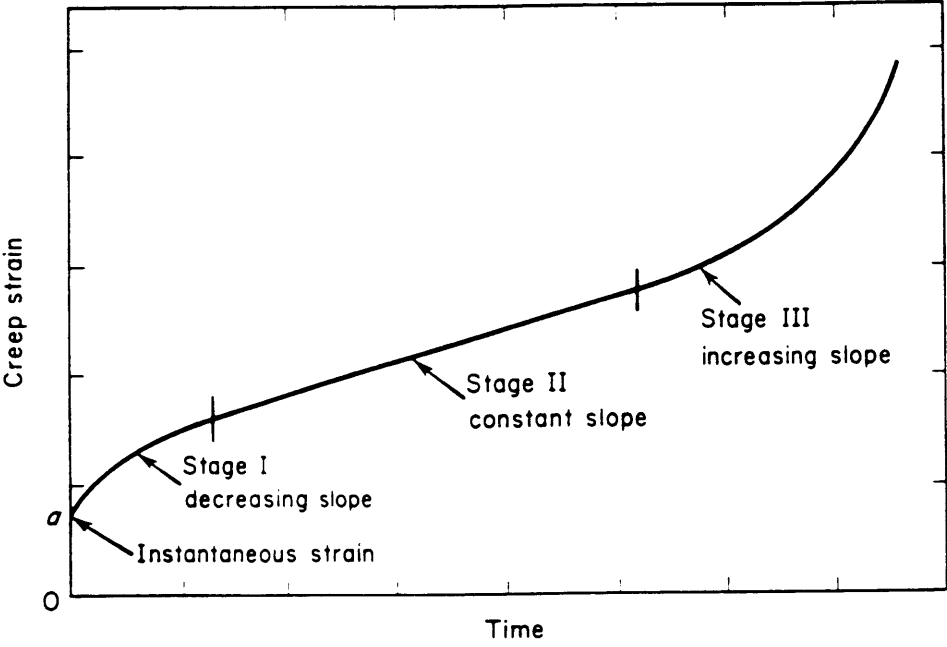


Figure 2.1: Schematic creep curve. As can be seen, there are three distinct creep regimes, Stages I, II, and III; describing regions of primary, steady-state and tertiary creep, respectively. The initial region has a decreasing slope, while Stage II has a constant slope and Stage III a rapidly increasing slope and failure.

3. EXPERIMENTAL PROCEDURE

3.1 Materials, Processing and Microstructure

3.1.1 Materials System

A system of pure copper (Cu) reinforced with pure molybdenum (Mo) particulate was chosen for this study. Some property data for these two metals are listed in Table 3.1. In addition to the favorable properties of this system described in what follows, Cu-Mo composites are commercially interesting. The high melting temperature and high strength of the Mo reinforcement give these composites a high resistance to welding, mechanical wear and deformation. The Cu matrix provides very good electrical and thermal conduction and a low contact resistance. The main commercial use of this composite is as a contact material in heavy-duty electrical switching applications. The Cu-Mo composites are also being used in resistance welding, electrical discharge machining, electro-chemical machining, and as semiconductor bases with low thermal expansion.

According to the Cu-Mo phase diagram, shown in Figure 3.1., this system shows no solubility in the solid state (Subramanian and Laughlin 1990). At room temperature the mutual solubilities were reported as 0.0 %. From the phase diagram, at equilibrium, no liquid will appear below 1084.87°C, at which point the solubility of Mo in Cu is 0.0% and that of Cu in Mo only 0.063%. Using neutron diffraction, insoluble systems are less complicated to analyze over a range of temperatures than systems with finite and consequently temperature-dependent solubilities

Load transfer in a composite is largely driven by the difference in stiffness between the two components. The larger the difference, the more pronounced the load transfer (Clyne and Withers 1993). Ideally one would want as stiff a reinforcement as possible. However, the stiffer the reinforcement, the smaller the elastic phase strain at a given phase stress. Smaller phase strains are harder to detect with neutron diffraction; strains smaller than 50 microstrain can not be detected. This difference between Cu and Mo in elastic moduli is smaller than in several more common composite systems, such as Al/SiC. The Al matrix is weaker than the Cu matrix and the SiC reinforcement is stiffer than the Mo reinforcement. Accordingly, larger strains should develop in the reinforcement of a Cu/Mo system than in the reinforcement of an Al/SiC system, thus improving the accuracy of the neutron strain measurement.

Both Cu and Mo crystallize in the cubic system. More complicated crystal structures would complicate the neutron diffraction strain measurements. The strong metallic bonding at the Cu-Mo interface should also lead to improved load transfer characteristics.

Based on a simple Eshelby calculation for transformation stresses, presented by Clyne & Withers (1993), a volume fraction of 15% Mo in Cu was chosen. This was seen to give a sufficient strain difference, while yielding detectable reinforcement strains on the order of several hundred microstrain. 15% reinforcement is very commonly used also in commercial systems, thus allowing for comparisons between this model system and commercial systems.

3.1.2 Sample Fabrication

The test specimens were processed from powders. 99.8% pure molybdenum powder was obtained from Aremco Products (Ossining, NY). It was reported to be spherical with diameters between 10 and 44 μm . Upon inspection in the optical microscope, the particulates were found to be irregular, but equiaxed, with the average size close to the lower reported limit. 99.9% pure copper powder was obtained from Atlantic Equipment Engineers (Bergenfield, NJ). This powder was reported to be spherical with a particulate size less than 44 μm (-325 mesh). Upon inspection in the optical microscope, the reported parameters were in agreement with observation.

The powders were compacted to full density by hot isostatic pressing (HIPing), which is a powder metallurgical technique that involves applying high pressure and temperature to a sealed container holding the powder. Under these conditions, the powder will sinter and compact to full density.

Dr. Joe Runkle at Industrial Materials Technology (Andover, MA) was contracted to perform the HIPing. At his plant, copper and molybdenum powder were mixed and blended to contain 15% molybdenum by volume. The blended powders were then cold pressed into steel containers. The steel containers were cylinders of height 21 cm and inner diameter 6.5 cm. The steel wall thickness was 3 mm. Prior to the introduction of the powders, the steel cans were lined with molybdenum foil. The purpose of the foil was to prevent diffusion of carbon from the steel walls into the copper/molybdenum blend during HIPing. Two cans were used. One of the cans had a molybdenum foil separator at half height, below which the powder

blend was pressed, and above which pure copper powder was pressed. The other can was filled entirely with the copper/molybdenum powder blend.

In order to remove any oxide that might have formed on the particulates, the pressed powders in the cans were reduced in an H₂ atmosphere. The powders were heated under vacuum to 850°C. They were then held at this temperature for four hours while being flushed with H₂ gas. Prior to HIPing, the cans were evacuated, helium leak checked, off gassed and sealed. The cans were then HIPed at 900°C, at a pressure of 100 MPa, for 125 minutes. The empty steel can, as well as the fully HIPed ones, are shown in Figures 3.2. and 3.3.

Samples were machined using conventional techniques as well as electric discharge machining. All machining was performed by Laboratory Testing, Inc. (Dublin, PA). Sample dimensions are shown in Figure 3.4. The samples had a total length of 77.7 mm, a gage length of 33 mm. The diameter at the gage length was 6.35 mm. The ends were threaded at 13 threads per inch (13UNC), and a diameter of 12.7 mm.

3.1.3 Metallography

Metallography was performed using conventional techniques at the Los Alamos National Laboratory's Materials Science Lab (MSL). Samples of scraps after machining were cut into small pieces and mounted using a standard Bakelite hot mounting process. The samples were then ground using progressively finer meshes, and polished using 0.3 μm alumina particles in water solution, and a napped cloth polishing wheel. Micrographs were taken in the optical microscope, and two are shown in Figures 3.5. and 3.6.

It can be seen that some clustering took place during processing. The Mo clusters seen throughout the matrix generally ranged in size from 5 μm to 50 μm . Few voids could be seen. Microstructural features of the matrix were difficult to detect.

3.2 Description of Apparatus

3.2.1 Facility

Neutron diffraction experiments were performed at the Manuel Lujan, Jr. Scattering Center (MLNSC) at the Los Alamos National Laboratory in Los Alamos, New Mexico. This facility is a pulsed spallation neutron source equipped with time-of-flight spectrometers for condensed matter research. Together with ISIS in England, MLNSC provides the highest peak neutron beam current in the world.

By accelerating protons along a linear accelerator, and subsequently letting the protons collide with a tungsten target, neutrons are driven from the tungsten nuclei. The proton energy at this facility is 800 MeV in bursts at a rate of 20 Hz. The resulting neutron current hitting the sample is about 70 μA .

3.2.2 Instrument

The experiments were performed on the neutron powder diffractometer (NPD). In this instrument, the sample is irradiated with the pulsed beam of neutrons having a wide spectrum of energies. Scattered neutrons are recorded in banks of detectors located at different angles. The

time of flight of the neutron from generation at the target to the detectors is recorded.

A schematic of the neutron beam's interaction with the sample and the positions of the detectors is shown in Figure 3.7. The detector banks of interest for this experiment are Banks 3 and 4, which are located at a 90° angle on either side of the sample, as shown in the figure. Bank 3 (-90°) records scattering from the lattice planes in the transverse direction, whereas Bank 4 ($+90^\circ$) records those in the axial direction.

The stress rig consists of a servohydraulic, piston-driven, mechanical testing apparatus capable of both compressive and tensile loading. Several different sample dimensions can be accommodated. A picture of the rig, and a technical drawing, are shown in Figures 3.8 and 3.9, respectively. When the sample is mounted in the rig, the loading axis is oriented horizontally. The maximum load capacity is 11,000 lbs, which corresponds to 1540 MPa given the sample diameter used. An Instron 8500+ Controller was used to control the mechanical aspects of the experiment. A 8620 Instron extensometer was used to measure strain. The controller allowed for feedback loop control of position of the actuator arm or applied stress. LabView software was used to record time, strain, actuator arm displacement, applied stress, and temperature. The sample was attached to the load cell post and piston using bored and threaded Curtis joints. The joints threaded into the sample at one end, and into the post or piston on the other end.

3.2.3 Heating System

For the high temperature experiments, heating was provided by two radiation parabolic strip heaters. One was mounted directly above the sample and the other directly below it, as shown in Figure 3.10. The heaters provided infrared heating composed of parallel infrared waves, focused on a rectangular area of 3.8 cm width. This allows for some freedom in positioning the sample within the focused area. By having heaters above and below the sample, the horizontal plane containing the incident and diffracted neutron beams was left unobstructed.

The heaters were supplied by Research, Inc. (Minneapolis, MN). The model number was 5305-2A. It was designed to concentrate high radiant flux energy on a target strip 3.8 cm (1.5") wide. The lamps used were tubular quartz lamps 6.4 cm (2.5") long, providing a lighted length of 6.5 cm (2.56"), with a power rating of 1.0 kW.

An 8710 Dimension Multi-Loop Process Controller and a 663F Power Controller were supplied by the same company. The power controller was controlled automatically with 0-5 V DC signal from the process controller. The system had a digital PID control. A thermocouple input was used to provide closed-loop control of the sample temperature. The controller could be used to set the heaters at a given power level (in percent) using the manual loop mode or at a given temperature using the auto loop mode. For PID settings, a gain of 16.02, a reset of 14.57 r/m, and a rate of 0.00 min. was found to give fairly uniform temperature ramps and little overshooting. The set temperature was then held to within +/- 1.5°C.

The two primary concerns motivating heat containment were the heating and potential subsequent weakening and failure of the Curtis joints, and the general heating of the stress rig and the air in the experimental can. Water cooling was provided to the two heaters and to the piston and the load cell post. Heat was also contained by using a boron nitride shield on each side of the heaters. The shields had windows to allow for unobstructed passage of the incident and diffracted neutron beams. Finally, the Curtis joints were wrapped with thermally insulating non-asbestos paper, as shown in Figure 3.11.

3.3 Description of Experiment

3.3.1 Room Temperature Neutron Diffraction Experiment

Room temperature experiments were performed from July 23 through July 26, 1996. A table of the experiments containing stress levels and durations, is shown in Table 3.2. All stresses applied were tensile. The stress on the sample was applied by controlling the position of the actuator arm. Stress levels were changed by manually changing the position of the actuator arm until the appropriate stress level was obtained. Any undesired time-dependent effects would therefore show up as a relaxation of the applied stress. Strain was recorded using a standard Instron extensometer. Diffracted neutrons were detected at banks recording diffraction from lattice planes oriented in the axial and transverse directions, respectively, of the sample.

An initial experiment was done holding the sample in tension at 5 MPa. The stress levels were then increased in 20 MPa increments to 165 MPa, then unloaded to 85 MPa, and finally brought back to 5 MPa. Each stress level

was held for the time it took to collect a number of neutrons corresponding to 250,000 μA -hours. With generally stable neutron beam delivery, this time was approximately 5 hours. The exact times are given in Table 3.2. The entire sequence of experiments were performed on the same sample.

3.3.2 High Temperature Neutron Diffraction Experiments

For the high temperature experiments, the heaters were mounted as previously discussed in Section 3.2.3. The heat shields were attached using C-clamps. Temperature was monitored by a thermocouple inserted into a hole drilled into the shoulder of the sample. K-type probe thermocouples of diameter 0.02" (0.51 mm) were used, and the holes drilled were a close fit. Preliminary tests had shown that there were no detectable temperature gradients from the shoulder to the middle of the gage length after 10 minutes at 300°C, and the temperature read at the shoulder was considered the temperature throughout the sample during the experiments.

Due to the constraints imposed by the requirement of free passage for the incident, transmitted, and diffracted beams, and additionally by the space taken up by the heaters; no extensometer could be used. Strains were calculated based on the displacement of the actuator arm applying the stress to the sample. The displacement divided by the sample gage length of 33 mm yielded strain values. At constant load, and assuming that only the sample and no other apparatus components creeps, this gives a fairly accurate strain measurement.

In order to successfully determine the phase lattice parameters during steady state creep at constant load, this creep regime has to be maintained for

the time needed to collect the required number of neutrons, i.e.. about five hours. The two parameters that could be varied to achieve the appropriate creep strain rates were applied load and temperature. The temperature was initially chosen as 300°C. Applying this temperature to the sample, initial experiments were performed without the neutron beam to determine the appropriate stress levels. A deformation of 3% on the 33 mm gage length of the sample in 5 hours corresponds to a strain rate of $1.7 \cdot 10^{-6} \text{ s}^{-1}$. After measuring steady-state strain rates at 50, 80, and 110 MPa, the stress levels for the initial neutron experiments were determined.

The high temperature neutron diffraction experiments were performed from November 6 through November 11, 1996. A summary of the experiment sequences and samples used is shown in Table 3.3. All stresses applied were tensile.

Sample #4 was mounted in the stress rig and heat shields were attached. After inserting the stress rig into its position in the neutron flight path, the heaters were set to 300°C. After achieving that temperature throughout the sample, an initial 5 hour experiment was performed at 5 MPa. The stress was then increased to 105 MPa. The neutron collection from the primary and steady state creep regime were done in separate files. After recording a sufficient number of neutrons during the steady state creep experiment, the stress was increased to 125 MPa, and the same sequence of neutron collections was recorded. This time the sample failed after only 26 minutes in steady state.

The next sample (Sample #6) was also heated to 300°C, and was tested in a similar fashion as the previous one, but this time at 85 and 95 MPa, respectively. The sample failed at 95 MPa after 1 hour and 8 minutes of steady

state creep. Another sample (Sample#7) was tested at the same temperature in a similar fashion, at 50, 75, and 115 MPa. The sample failed at 115 MPa after 27 minutes of steady state creep.

For Sample #8, a different sequence of experiments was executed. At each stress level, a room temperature experiment was performed prior to a experiment at a temperature of 350°C. The high temperature experiments were performed similar to the previous ones, with separate neutron collection during primary and steady state creep. The stress levels were 50, 65, and 80 MPa. At 80 MPa the sample failed after 2 hours of steady-state creep.

3.3.3 Neutron Diffraction Data Analysis

The collected neutron data was analyzed using the General Structure Analysis System (GSAS). GSAS is a set of programs for the processing and analysis of neutron diffraction data based on Rietveld analysis. A more detailed description of GSAS can be found in the manual by Larson & Von Dreele (1994). Based on tabulated crystallographic and physical data, GSAS performs a fit of the entire diffraction pattern (Figure 3.15). This initial fit can then be improved by refining certain statistical parameters. When a satisfactory fit is obtained, the lattice spacing is calculated using all peaks in the pattern, for each phase in each experiment. Strains are then determined using the appropriate reference lattice spacing and Eqn. 12. The reference lattice spacings were obtained from the 5 MPa experiments at the appropriate temperatures for the given sample.

3.3.4 Conventional Mechanical Testing at Room Temperature

Using the same stress rig as described previously, conventional mechanical testing without neutrons was performed. Stress-strain curves were obtained for a pure Cu sample and for a Cu/15%Mo sample. The pure Cu and the composite sample were unloaded at approximately 2% and 1% strains, respectively. The samples were thereby preserved for other preliminary testing.

3.3.5 Conventional Creep Testing

Conventional creep testing in a creep frame was performed at MIT. Sample dimensions were the same as previously described, and shown in Figure 3.4. Constant load creep tests were performed in air according to ASTM #E139 on a creep frame with lever arm ratio of approximately 1:9.8 (Figure 3.12). The lever arm ratio had already been determined by placing standard weights on the weight hanger and measuring the load in the load train with a load cell. The creep tests were performed in tension. Attached to the sample shoulders are rods which translate the motion between the upper and lower shoulders outside of the furnace where the displacement can be measured by a linear voltage displacement transducer (LVDT) (Figure 3.13). 60° V-notches (0.92 mm width) were machined into the shoulders to allow for the attachment of the extensometer. The strain was measured by an LVDT attached to an extensometer (ATS Series 4112, 12.7 - 101.6 mm range) (Figure 3.13). The resolution of the LVDT was +/- 2.5µm. The sample temperature was monitored by two thermocouples and maintained within +/- 1°C by a three zone furnace. The position of the LVDT, time and, and temperature

were recorded using customized Macintosh-based Basic data acquisition software (Figure 3.14).

Tests were performed at 300°C (Sample #9) and 350°C (Sample #10), corresponding to the temperatures used during the high temperature neutron diffraction experiments. One sample was used at each temperature.

At 300°C, the stress levels applied were 75, 95, 125, 81, 103, 115, and 120 MPa. After applying 125 MPa, the resulting strain rate was higher than expected based on the power law dependence of the strain rate on the stress, thus indicating that the power law breakdown regime was entered. After measuring a steady state strain rate at 125 MPa, the sample was unloaded and annealed for 10 hours. The stress level sequence described above was then continued. At 350°C, the stress levels applied were 60, 70, 80, and 90 MPa. No annealing or unloading occurred.

Chapter 3 Figures

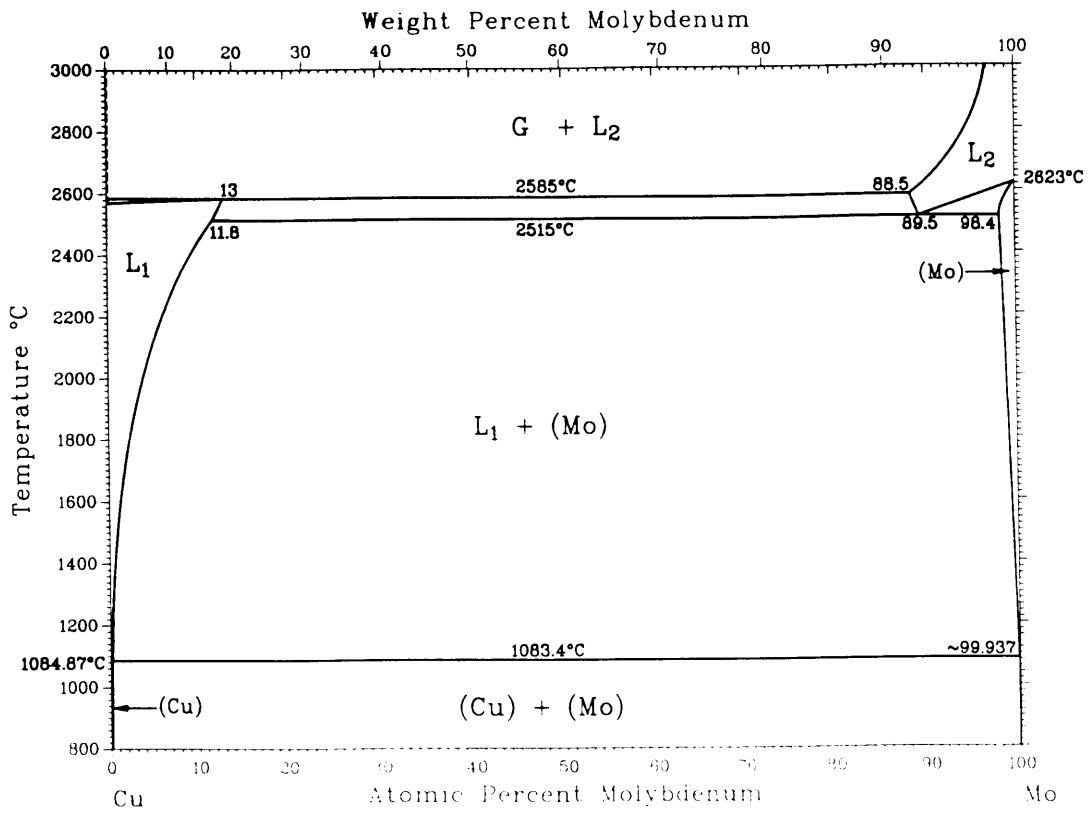


Figure 3.1. Cu-Mo phase diagram. The components are insoluble in the solid state (Subramanian & Laughlin, 1990). Liquid copper appears at 1085°C.

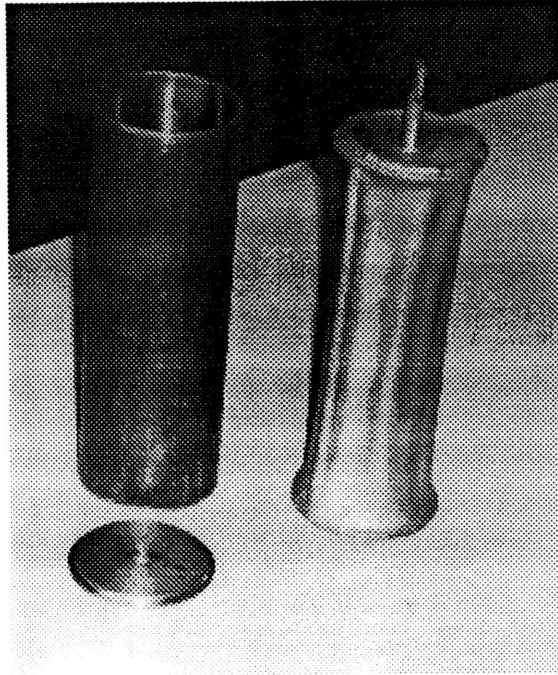


Figure 3.2. Photograph showing an empty steel HIP can together with a fully densified can.

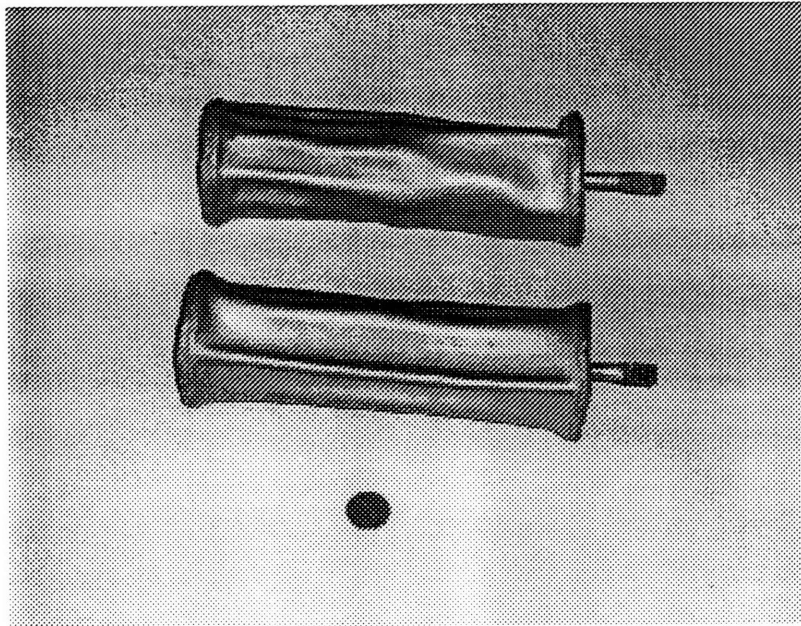


Figure 3.3. Photograph showing the two fully densified HIP cans. These two cans provided all samples for the study.

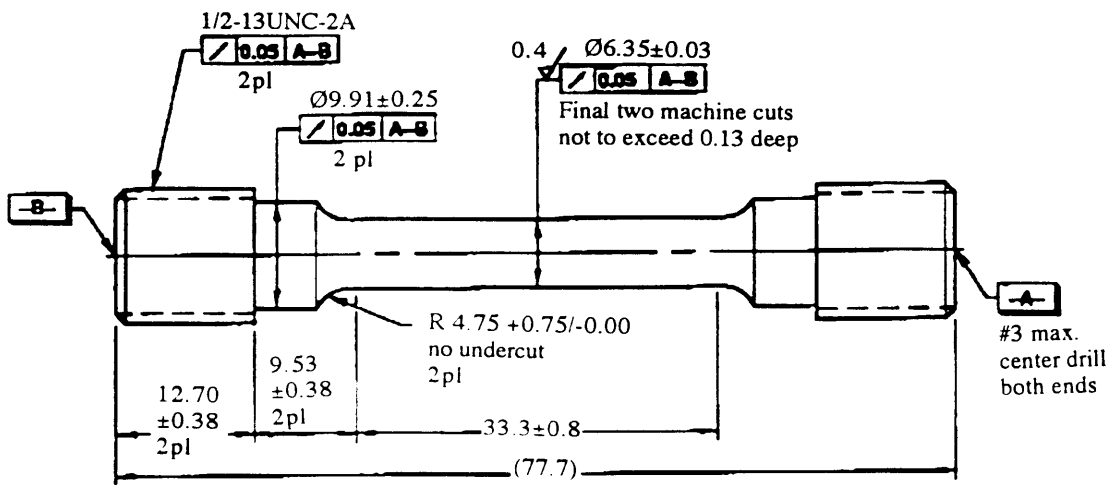


Figure 3.4. Sample dimensions. Sample specimens were machined using EDM. The sample has threaded ends, a 33 mm gage length and a 6.35 mm diameter at the gage.

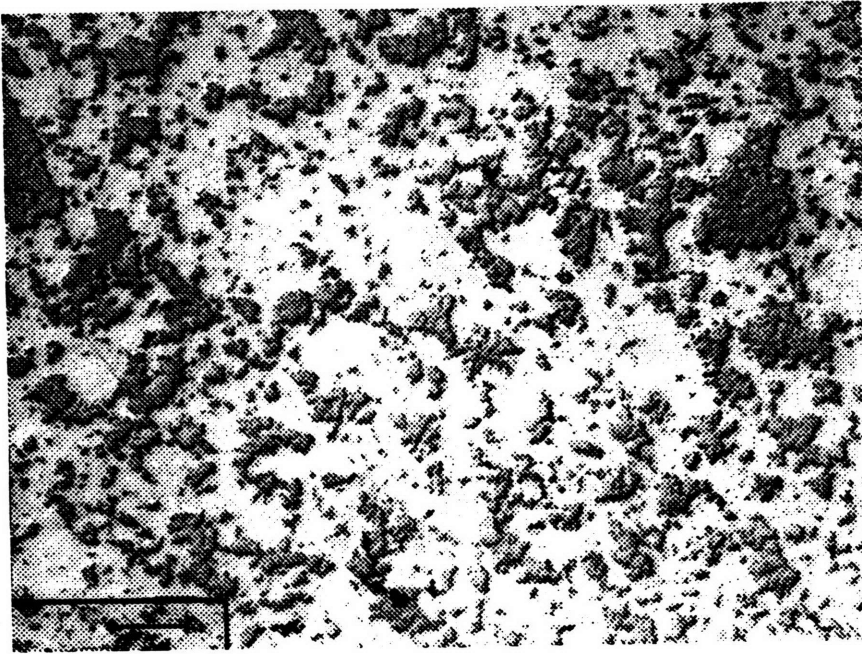


Figure 3.5. Micrograph taken in the optical microscope. 1 cm = 50 μm .

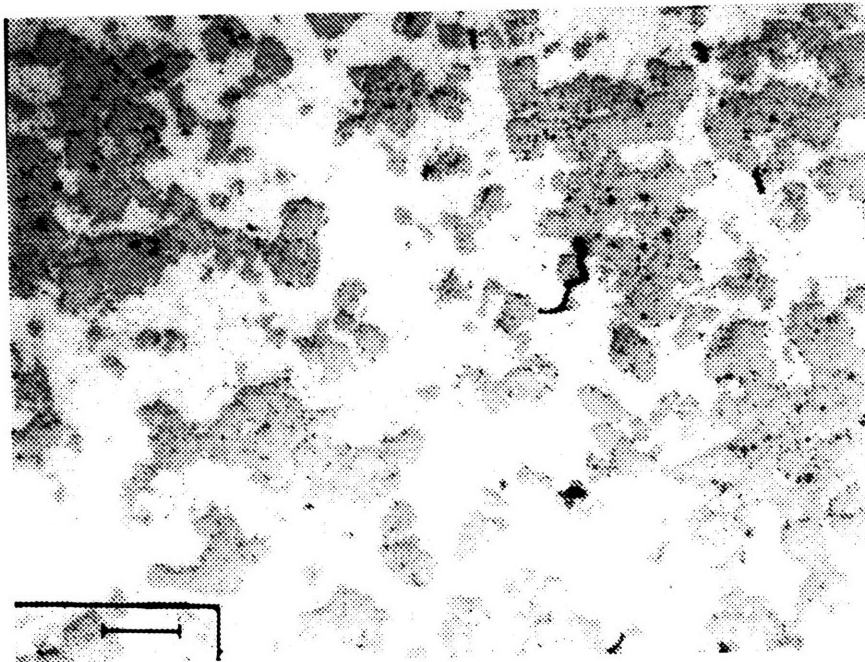


Figure 3.6. Micrograph taken in the optical microscope. 1 cm = 20 μm .

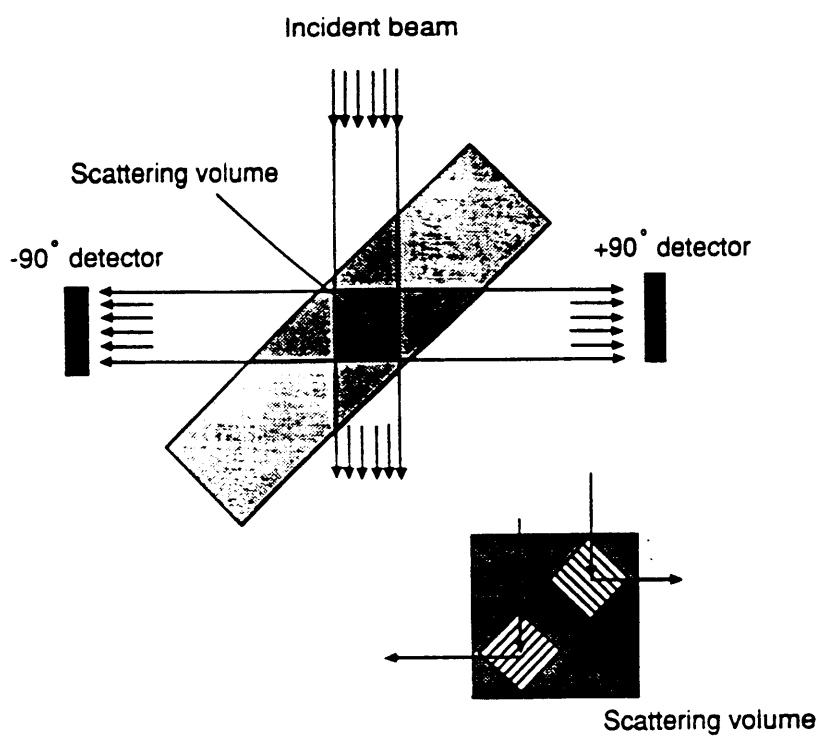


Figure 3.7. Beam interaction with sample and position of detectors.

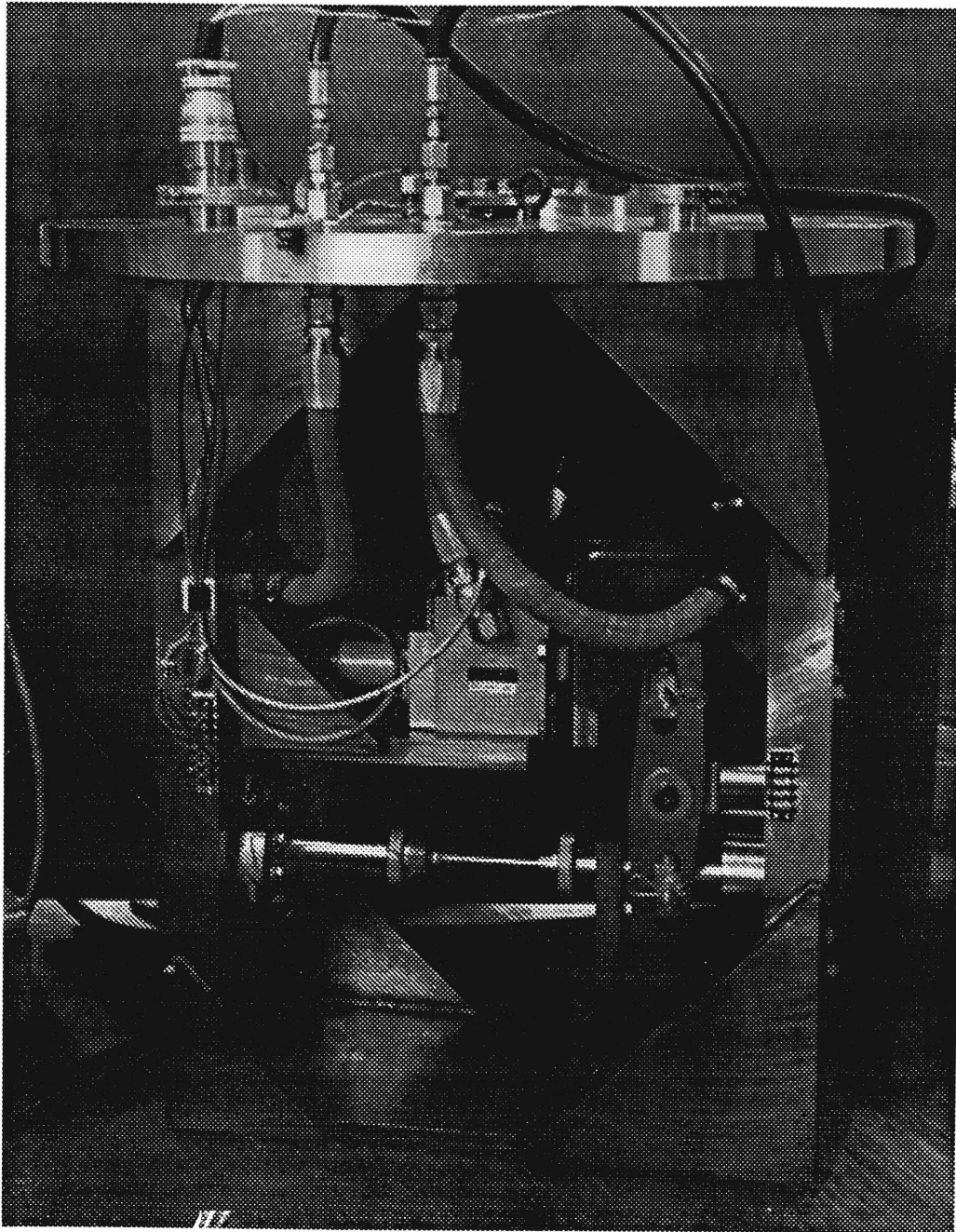


Figure 3.8. Photograph showing the stress rig used for the in-situ loading neutron diffraction experiment.

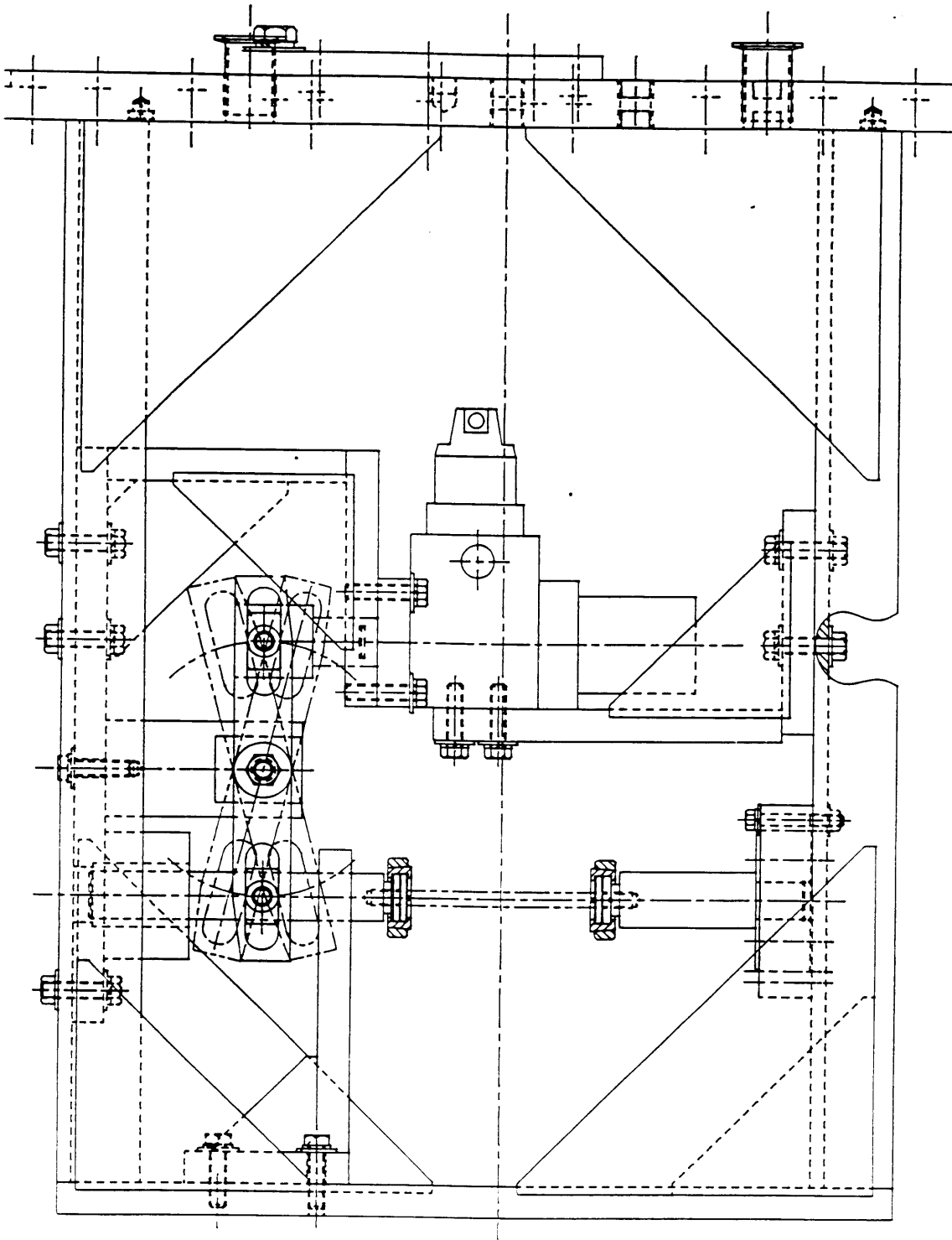


Figure 3.9. Technical drawing showing the stress rig.

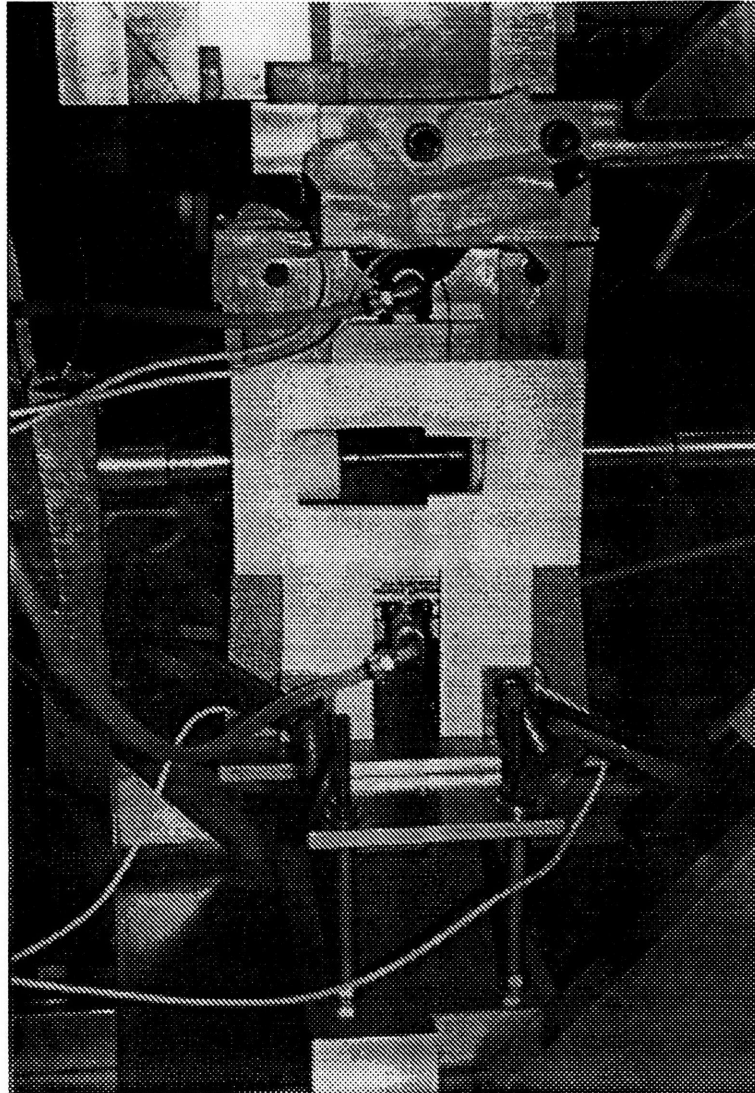


Figure 3.10. Photograph showing close-up view of heaters and sample mounted in stress rig.

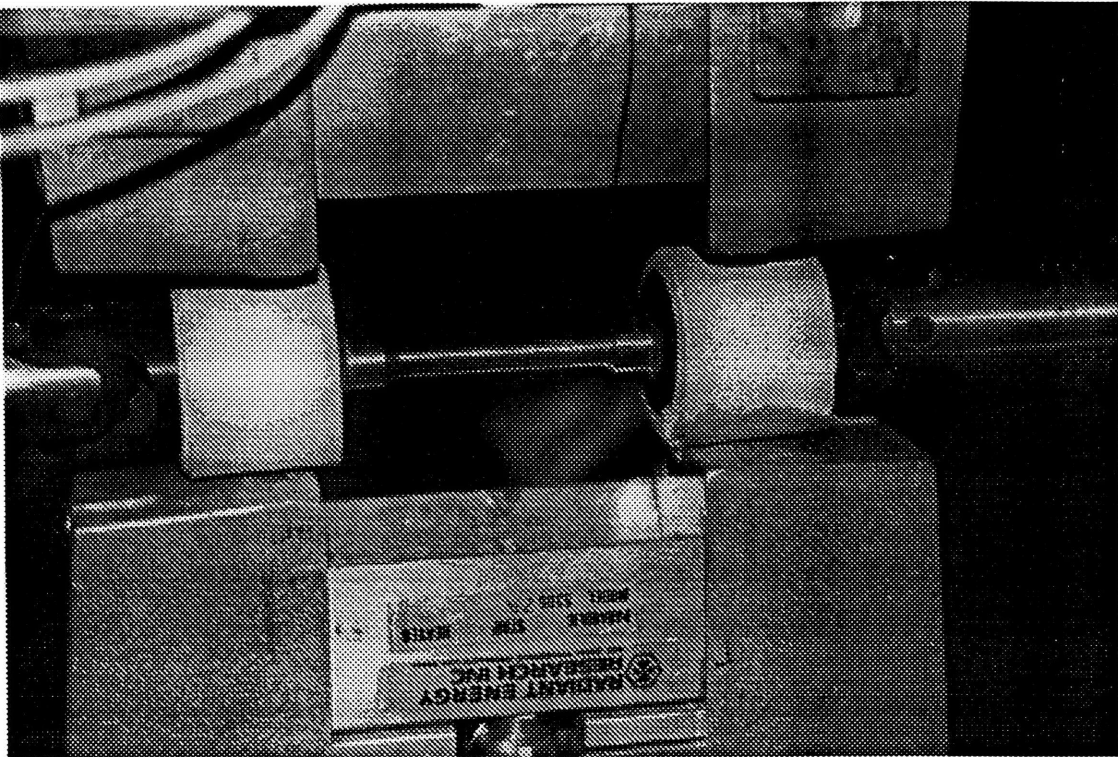


Figure 3.11. Photograph showing heat shields mounted on stress rig.

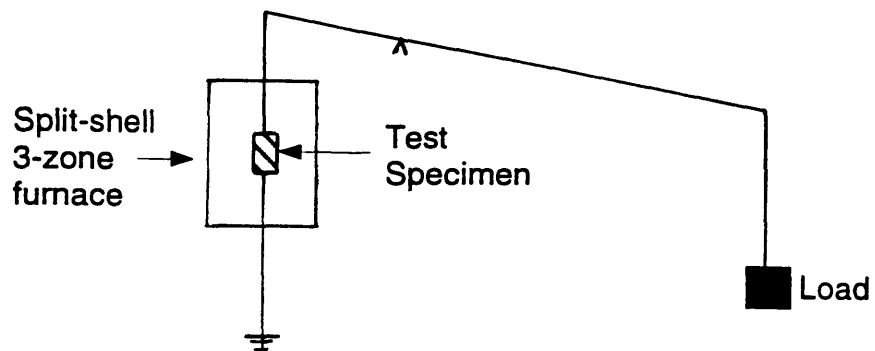


Figure 3.12. Schematic of constant-load creep testing apparatus. (Jansen 1996)

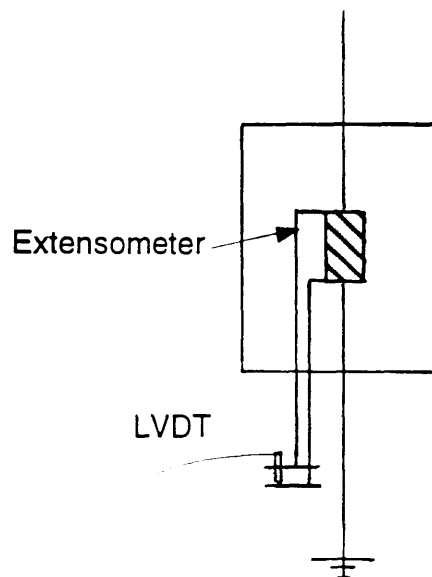


Figure 3.13. Schematic of extensometer arrangement. (Jansen 1996)

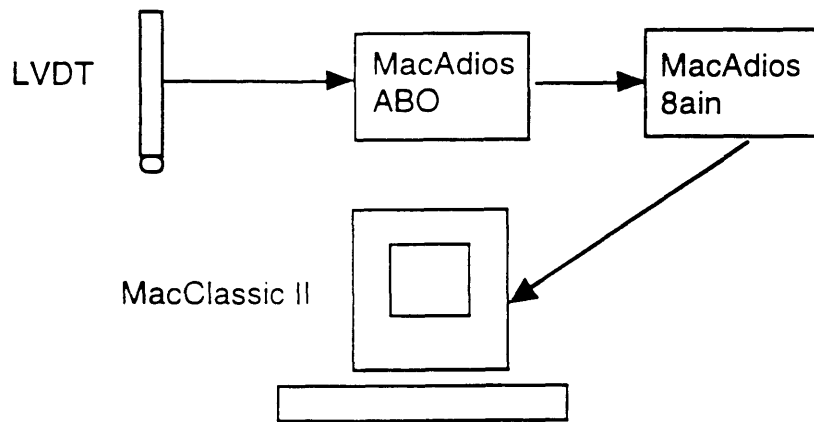


Figure 3.14. Schematic of data acquisition system. (Jansen 1996)

RUN 2334 BANK 4
Bank 4, 2-Theta -90.0, L-S cycle 57 Obsd. and Diff. Profiles

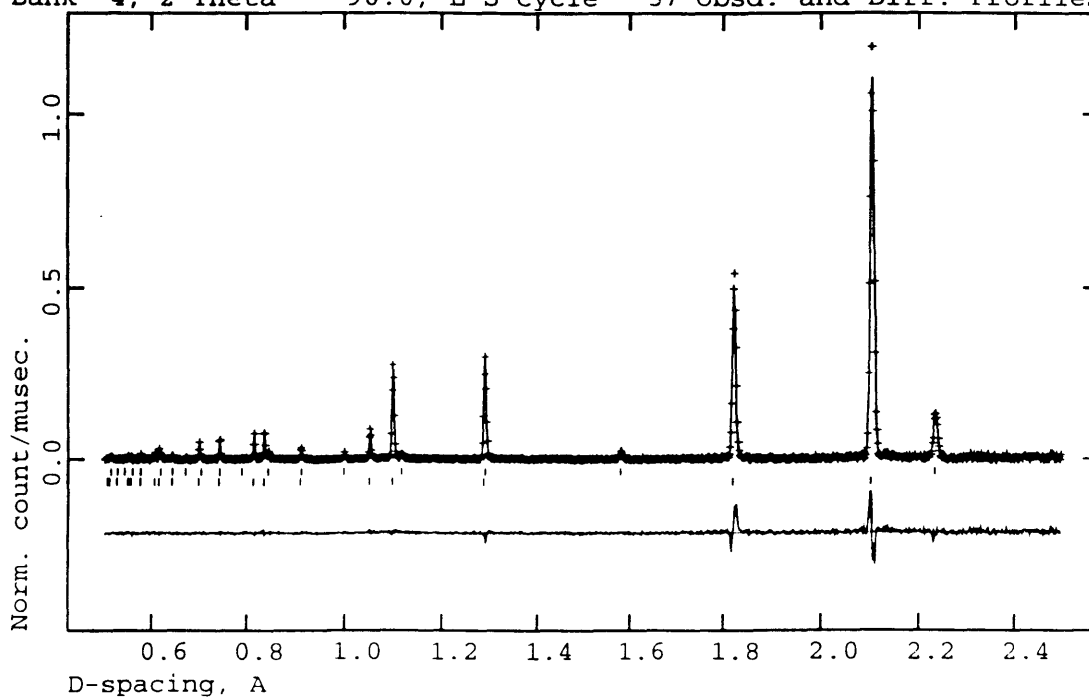


Figure 3.15. Neutron diffraction pattern.

Chapter 3 Tables

Table 3.1. Properties of the Pure Metals Cu and Mo from the Literature.

Property	Cu	Mo
Melting Point (°C)	1085 ¹	2610 ¹
Density (g/cm ³)	8.93 ¹	10.22 ¹
CTE (e-6/°C) at 20°C	16.5 ¹	5 ¹
Crystal System	FCC ¹	BCC ¹
Space Group	Fm3m ¹	Im3m ¹
Lattice Parameter (Å)	3.61509 ¹	3.1468 ¹
Elastic Modulus (GPa)	130 ²	324 ²
Poisson's Ratio	0.343 ²	0.293 ³

Sources: ¹ASM Metals Handbook (1979), ²Smithells (1992), ³Meyers and Chawla (1984).

Table 3.2. Targeted Loads, Mean Loads, and Elapsed Times for Room Temperature Experiments

Targeted Load (MPa):	Mean Load (MPa):	Elapsed Time (hr:min):
5	5.2	4:55
25	25.3	8:51
45	45.5	5:55
65	65.0	5:43
85	84.3	5:54
105	104.0	5:54
125	124.2	5:44
145	141.4	5:35
165	160.5	5:34
85	86.0	6:36
5	5.9	34:43

Table 3.3. Temperatures, Applied Loads, Elapsed Times, and Sample Numbers for High Temperature Experiments

Temperature (°C):	Applied Load (MPa):	Elapsed Time (hr:min)	Sample #:
25	5	6:04	4
300	5	5:17	4
300	105	6:46	4
300	125	0:26	4
300	5	4:54	6
300	85	4:58	6
300	95	1:08	6
300	5	4:55	7
300	50	4:57	7
300	75	5:12	7
300	115	0:27	7
25	5	6:25	8
350	5	6:45	8
25	50	5:52	8
350	50	4:40	8
25	65	4:50	8
350	65	4:47	8
25	80	4:34	8
350	80	2:00	8

4. EXPERIMENTAL RESULTS

4.1 Room Temperature Experiments

4.1.1 Macroscopic Properties from Conventional Mechanical Testing

Conventional mechanical testing yielded stress-strain curves for pure Cu and the Cu-15%Mo composite as shown in Figure 4.1. Table 4.1 shows the elastic moduli and yield strengths for both materials as obtained from the graph in Figure 4.1. The elastic modulus is 121 GPa for pure Cu and 157 GPa for the composite; this corresponds to a stiffness increase of 30% for the composite. The 0.2% yield strength is 65 MPa, and 130 MPa, for pure Cu and the composite, respectively, indicating a 100% increase for the composite. The composite hardening rate is also significantly higher than for pure Cu, as evidenced by the steeper slope in the plastic regime. At about 1% strain, the composite stress is more than twice that seen in the pure Cu.

4.1.2 Microscopic Properties from Neutron Diffraction Experiments

The results from the room temperature in-situ loading experiments are shown in Figure 4.2a, 4.2b, 4.3a, and 4.3b. The macroscopic applied stress is plotted versus the corresponding elastic phase strains determined by diffraction for both reinforcement (Mo) and matrix phase (Cu), in the axial direction in Figure 4.2a and 4.2b, and in the transverse direction in Figure 4.3a and 4.3b. The corresponding data is shown in Appendix 5. The lattice spacings used to determine strain were obtained from a weighted average of all lattice spacings corresponding to peaks in the diffraction pattern. This weighted

average was achieved using Rietveld analysis, briefly described in Section 4.3.3. The 5 MPa experiment was used for this zero strain measurement.

In the axial direction, the reinforcement initially has a lower elastic phase strain than the matrix, due to the higher elastic modulus of the reinforcement. Lines corresponding to the elastic moduli of both Cu and Mo are superimposed in Figure 4.2a; corresponding to the experimentally determined elastic modulus of 121 GPa for Cu (Table 4.1), and the literature value of 324 GPa for Mo from Table 3.1. At low applied stresses, both reinforcement and matrix curves are fairly linear and lie within the region defined by these two moduli lines. In other words, there are higher strains in the reinforcement than in a hypothetical pure Mo sample, and lower strains in the matrix than in pure Cu.

The error bars correspond to a strain error of $2 \cdot 10^{-5}$ in Cu and $8 \cdot 10^{-5}$ in Mo. These values are derived from the average error in lattice parameter as determined by Rietveld analysis. The error is larger in the Mo due to the fact that for any given amount of time a smaller mass of Mo is irradiated by the neutron beam.

For the matrix curve, no obvious kinks are seen, but strong curvature is evident at higher stresses. This curvature implies that the rate of increase of elastic strain in the matrix is reduced. For the reinforcement curve, the curvature is in the opposite sense, indicating that the rate of increase of phase strain is becoming higher.

The highest stress level achieved was 165 MPa. After unloading, the Cu matrix exhibits a compressive residual strain of $-3.4 \cdot 10^{-4}$. The Mo reinforcement shows a tensile residual strain of $5.1 \cdot 10^{-4}$.

In the transverse direction, compressive strains are observed for all values of applied stress, and the compressive strains are larger in the Mo reinforcement than in the Cu matrix (Figure 4.3). One can draw a smooth curve through the error bars, indicating a constant rate of increase of phase strain in each phase. After unloading, the Cu matrix exhibits a tensile residual strain of $1.5 \cdot 10^{-5}$. The Mo reinforcement shows a compressive residual strain of $-2.02 \cdot 10^{-4}$.

During the high-temperature experiment cycle, neutron diffraction data was also collected at room temperature at three stress levels. These three data points for each phase are shown together with the room temperature data in Figures 4.2b, and 4.3b, for the axial and transverse directions, respectively. The data associated with the high temperature cycle are labeled #2, whereas the rest of the room temperature data is labeled #1. For the axial direction, Figure 4.2b shows that the three #2 Cu data points lie on the line of the #1 Cu data. The #2 Mo data points show a similar slope and curvature as the #1 data, but is shifted to lower values of applied stress for the phase strain, but within the error of the measurement. In the transverse direction, the #2 Cu data show significantly lower phase strains than the #1 data for a given applied stress, well beyond the margin of error. The reduction in phase strain ranges from approximately $5 \cdot 10^{-5}$ to $1 \cdot 10^{-4}$. The #2 Mo data are similar to and within the error of the #1 data.

4.2 High Temperature Experiments

4.2.1 Macroscopic Creep Properties Obtained During Neutron Diffraction Experiments

Creep curves showing strain versus time were generated for each stress level, and are shown in Appendix 3. A linear fit to the straight portion of each of the curves yielded the steady-state strain rate for each stress level. In Figure 4.4, steady-state strain rate is plotted versus applied stress on a double logarithmic scale for the experiments at both 300°C and 350°C. A straight line fit of these points yielded the creep stress exponent, which is equal to 6.2 at 300°C, and 8.8 at 350°C. At 300°C, strain rates ranged from $1.4 \cdot 10^{-8} \text{ s}^{-1}$ at 50 MPa to $6 \cdot 10^{-6} \text{ s}^{-1}$ at 125 MPa. At 350°C, they ranged from $8 \cdot 10^{-9} \text{ s}^{-1}$ at 50 MPa, to $4 \cdot 10^{-7} \text{ s}^{-1}$ at 80 MPa. Unexpectedly, for corresponding stress levels, the strain rates recorded are lower at 350°C than at 300°C. However the maximum applied stress achieved at 350°C was 80 MPa as compared to 125 MPa at 300°C. Steady-state strain rates and stress are listed in Appendix.

4.2.2 Microscopic Properties from Neutron Diffraction Experiments

The microscopic phase properties at 300°C are presented in Figures 4.5. and 4.6., in the axial and the transverse direction, respectively. Similar plots for values at 350°C are shown in Figures 4.7. and 4.8. As with the room temperature figures, applied stress is plotted versus elastic phase strains.

In the axial direction at both 300°C and 350°C, as shown in Figures 4.5 and 4.7, respectively, the phase strains in the Cu matrix remains higher than in the Mo reinforcement at all values of applied stress. A straight line can be

fitted through the data for the Mo reinforcement at both 300° and 350°C. The curve for the Cu matrix shows a decreasing slope at 300°C (Figure 4.5). The two curves never intersect as they did at room temperature (Figure 4.2).

In the transverse directions at both 300° and 350°C, a straight line can be fitted through the Mo data. A straight line can be fitted through the Cu data at 300°C and 350°C. At 300°C some variation in the Cu data is beyond the margin of error. At both temperatures, the Mo phase maintains higher compressive strains than the Cu phase for all stress levels.

To compare the results at the three different temperatures, axial phase stresses were obtained using a uniaxial Hooke's law. Stresses were obtained by dividing the axial phase strains by the elastic modulus for the phase at a given stress and temperature. The values of the elastic moduli used at the different temperatures are shown in Table 4.2. Axial phase stresses are shown in Figures 4.9 and 4.10, at room temperature, 300°C, and at 350°C, respectively. The error bars correspond to the errors listed in Table 4.2.

The stress in the Mo phase is larger for all values of stress at all temperatures (Figure 4.9 and 4.10). The Mo curve at room temperature is showing a decreasing slope, whereas the Mo curve at 300°C is showing an approximately constant slope. The Cu curve at room temperature is showing an increasing slope, whereas at high temperature it is decreasing slightly. The Cu phase carries higher stresses at high temperature. Specifically, at an applied stress of 125 MPa, the phase stress in Cu is 112 MPa at 300°C, and 73 MPa at room temperature. Some fluctuations beyond error are seen in the Cu data.

A straight line can be fitted through the Mo data at 350°C as well, and there is little slope difference between the lines at 300° and 350°C (Figure 4.10). The Mo phase stresses at 300°C and 350°C are within the margin of

error and very similar. There is little difference in Cu phase stress at these two temperatures. Some fluctuations beyond error are seen in the Cu data at 350°C as well, but a straight line can be fitted to this data also.

Similarly, transverse phase stresses are shown compared to room temperature values, in Figures 4.11 and 4.12, at 300°C and 350°C, respectively. The stress in the Mo phase is more compressive than the Cu phase stress, for all values of applied stress, and a straight line can be fitted through the Mo data at all temperatures. There is little slope difference between the lines. This indicates that the reinforcement is under higher compressive stresses than the matrix, but that this phase stress distribution does not change much with the three temperatures probed nor with applied stress. Some fluctuations beyond error are seen in the Cu data at all temperatures, but can be approximately fitted with a straight line.

4.2.3 Macroscopic Properties from Conventional Creep Testing

Conventional creep testing at constant load with an extensometer yielded steady-state strain rates at corresponding applied stresses as shown in the double logarithmic plot in Figures 4.13, and 4.14, at 300° and 350°C, respectively. Assuming a power law strain rate dependence on stress, the stress exponent, n , was found by determining the slope of a linear fit to the data. The stress exponent was 13 at 300°C and 14 at 350°C. The strain rates are significantly higher at 350°C as compared to 300°C. Using the linear fit to the data, strain rates at 60, 80, and 125 MPa were plotted separately versus the inverse absolute temperature on natural logarithmic - linear scale (Figure 4.17). The slope of these curves yielded values of the activation energy for

power law creep as outlined in Appendix 1. The activation energies were slightly different at each stress level due to the slightly different stress exponents; they were determined to range from 183 to 243 kJ/mol. All strain rates and corresponding stresses are shown in Appendix 4.

The strain rates measured during the neutron diffraction are superimposed on Figures 4.13 and 4.14. These strain rates show significantly more scattering than the strain rates from conventional creep testing. At 300°C, they are higher by up to an order of magnitude than the strain rates collected during conventional creep testing. The stress exponent is reduced from 13 to 6.4. At 350°C, they are higher by up to half an order of magnitude, and the stress exponent is reduced from 14 to 8.8.

Using the equations and materials property values provided for pure copper in Table 4.3 (Frost & Ashby 1982), theoretical creep rates for unreinforced Cu, assuming power law creep, were determined and are shown together with the experimental values for the Cu-15%Mo, in Figures 4.15 and 4.16, at 300°C and 350°C, respectively. As can be seen from these figures, the composite shows lower creep strain rates for the stress range tested. The composite does however have a higher stress exponent than pure Cu. The pure Cu has a stress exponent of 6.8 at both temperatures, as compared to the composite's stress exponent of 13 at 300°C and 14 at 350°C. The pure Cu stress exponent of 6.8 is evidence of a low temperature $n+2$ power law creep regime (Frost and Ashby 1982). The activation energy was 121 kJ/mol (Figure 4.17), as compared to 183-243 kJ/mol for the composite.

Chapter 4 Figures

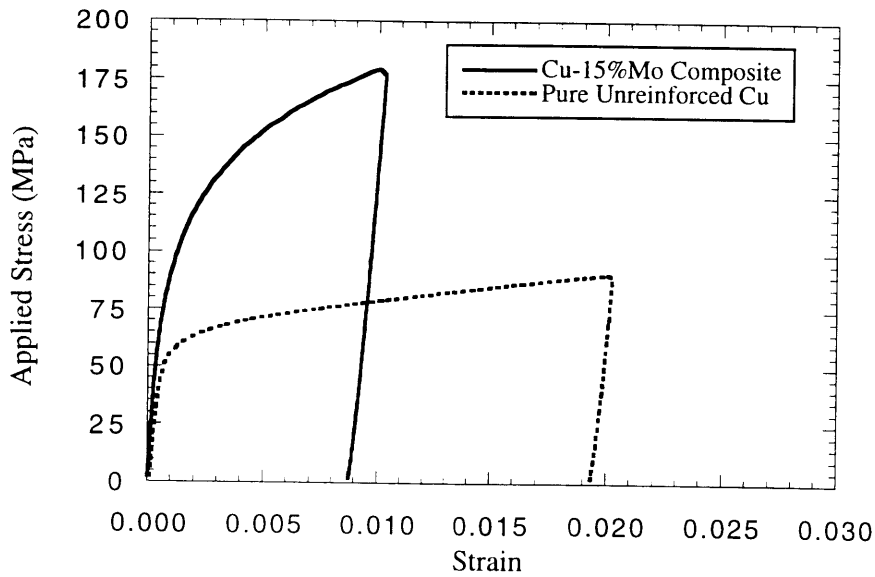


Figure 4.1. Applied stress versus macroscopic sample strain for pure Cu and Cu-15%Mo sample. The elastic modulus is 121 GPa for pure Cu and 157 GPa for the composite. The 0.2% yield strength is 65 MPa, and 130 MPa, for pure Cu and the composite, respectively.

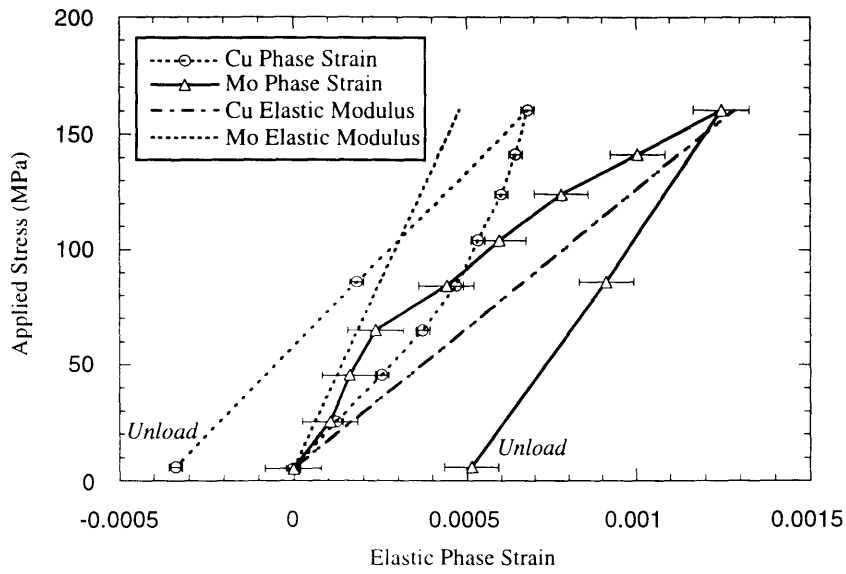


Figure 4.2a. Applied stress versus axial elastic phase strain for Cu-15%Mo composite at room temperature as obtained by neutron diffraction in-situ tensile test. The expected elastic response of each independent material is shown as well.

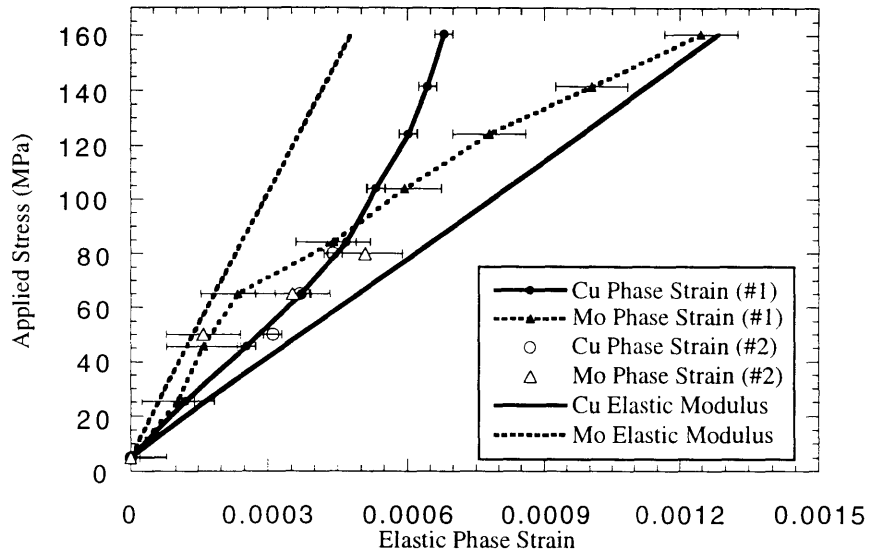


Figure 4.2b. Applied stress versus axial elastic phase strain for Cu-15%Mo composite. Results from the room temperature neutron diffraction experiment cycle (#1) are shown separately from room temperature experiments conducted during the high temperature experiment sequence (#2).

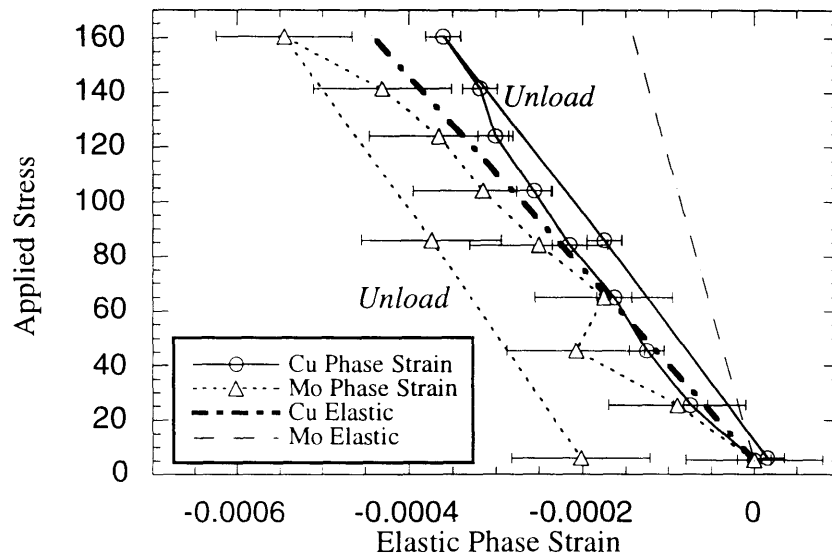


Figure 4.3a. Applied stress versus transverse elastic phase strain for Cu-15%Mo composite at room temperature, as obtained by the neutron diffraction in-situ tensile test. The expected elastic response of each independent material is shown as well.

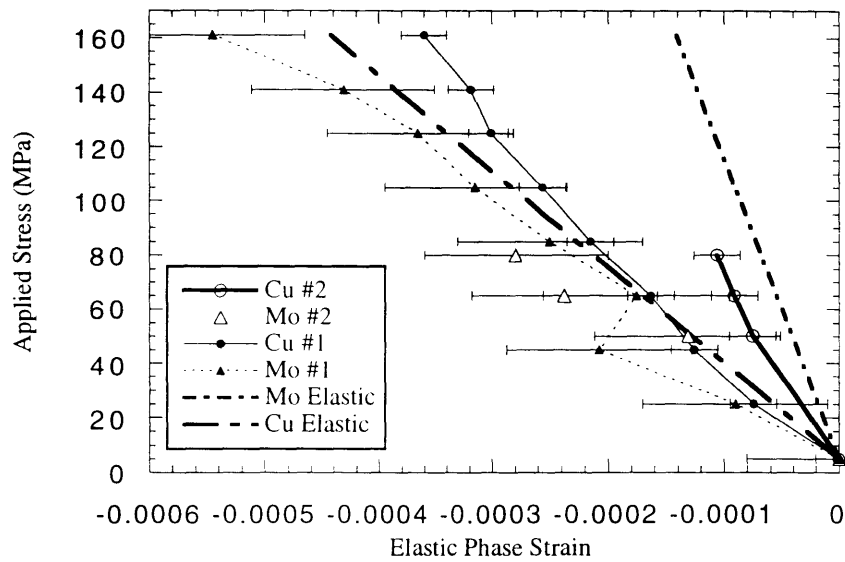


Figure 4.3b. Applied stress versus transverse elastic phase strain for Cu-15%Mo composite at room temperature. Results from the room temperature neutron diffraction experiment cycle (#1) are shown separately from room temperature experiments conducted during the high temperature experiment sequence (#2).

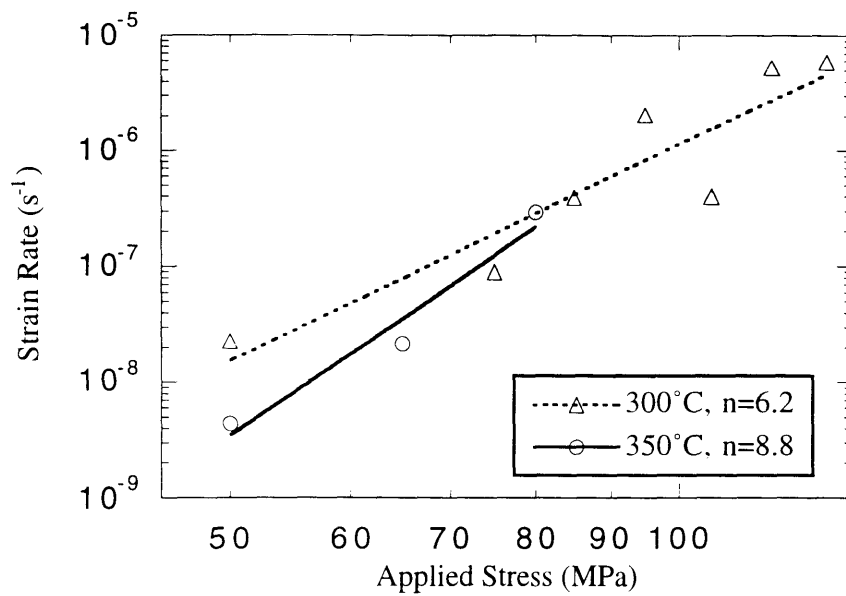


Figure 4.4. Steady state creep strain rate versus applied stress. The data shown was collected during the neutron diffraction experiment without extensometer. The stress exponent was 6.2 at 300°C and 8.8 at 350°C. Unexpectedly, the strain rates measured at 350°C were lower than those at 300°C.

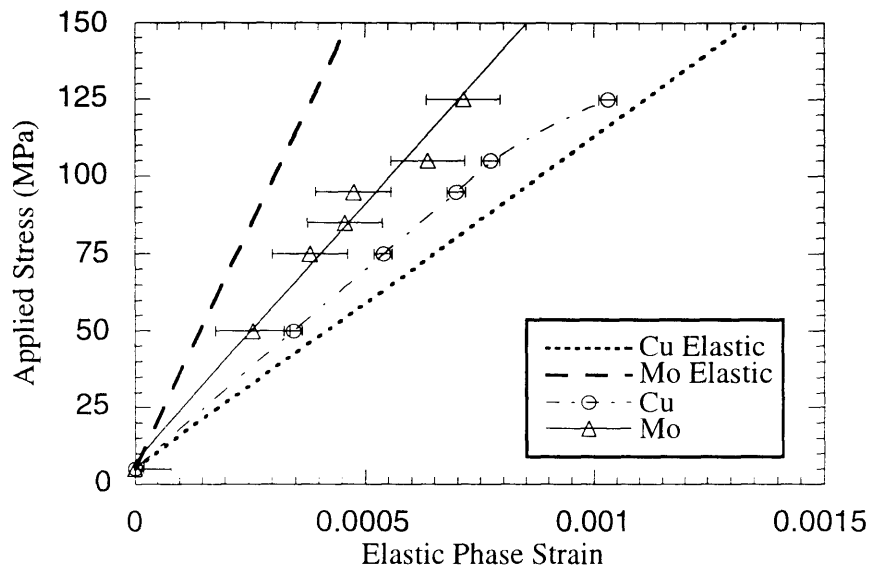


Figure 4.5. Applied stress versus axial elastic phase strain for Cu-15%Mo composite at 300°C, as obtained by the neutron diffraction in-situ creep test. A straight line can be fitted through the data for the Mo reinforcement. The curve for the Cu matrix shows a decreasing slope. The expected elastic response of each independent material at this temperature is shown as well.

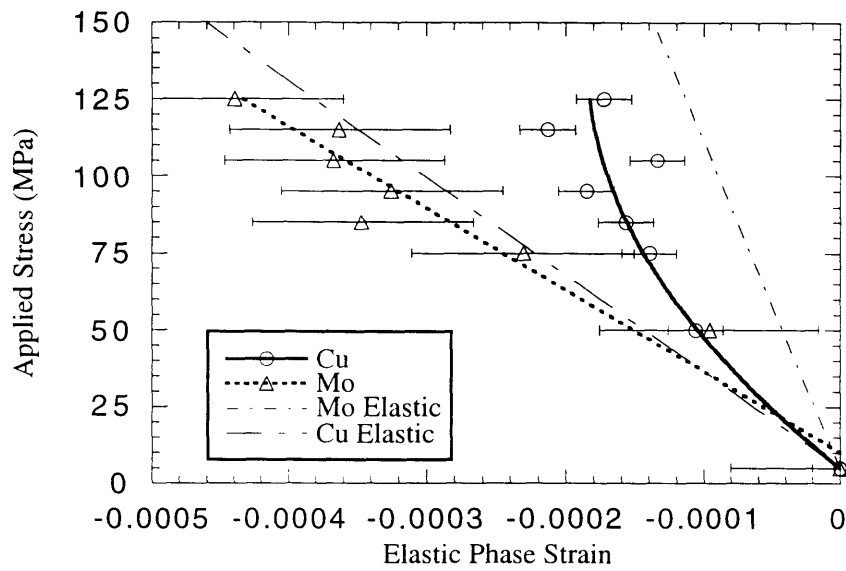


Figure 4.6. Applied stress versus transverse elastic phase strain for Cu-15%Mo composite at 300°C, as obtained by the neutron diffraction in-situ creep test. A straight line can be fitted through the data for the Mo reinforcement. The expected elastic response of each independent material at this temperature is shown as well.

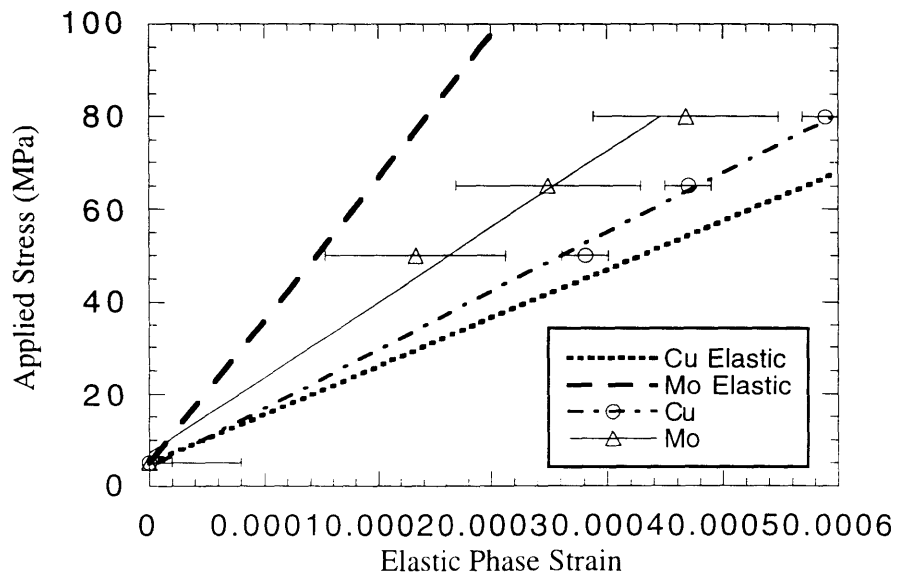


Figure 4.7. Applied stress versus axial elastic phase strain for Cu-15%Mo composite at 350°C, as obtained by the neutron diffraction in-situ creep test. A straight line can be fitted through the data obtained for both Cu and Mo. The expected elastic response of each independent material at this temperature is shown as well.

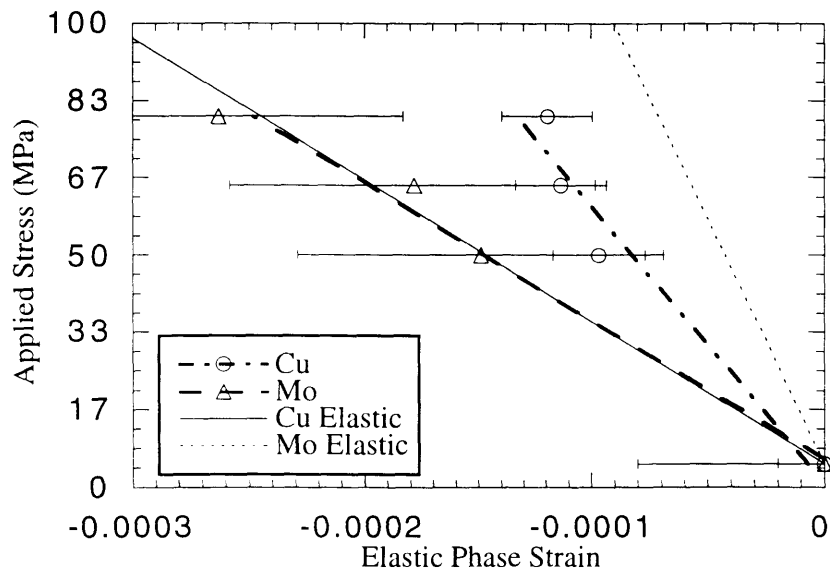


Figure 4.8. Applied stress versus transverse elastic phase strain for Cu-15%Mo composite at 350°C, as obtained by the neutron diffraction in-situ creep test. A straight line can be fitted through the data obtained for both Cu and Mo. The expected elastic response of each independent material at this temperature is shown as well.

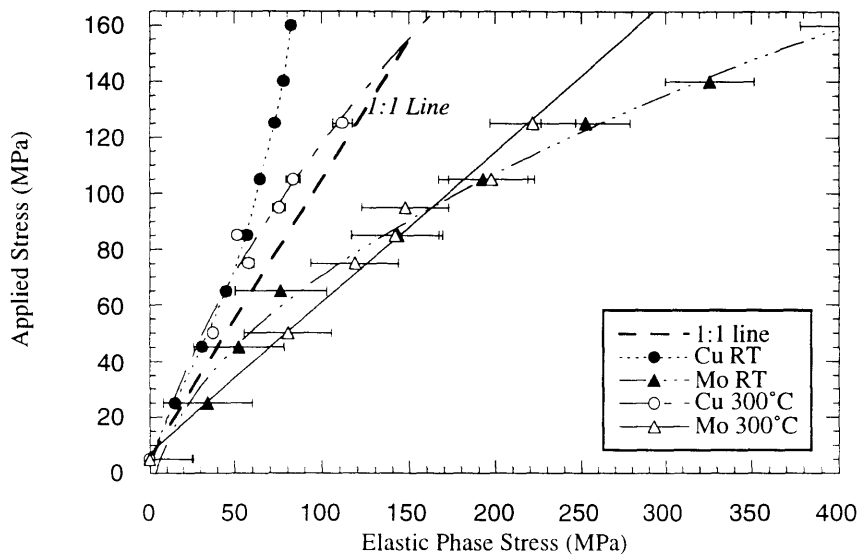


Figure 4.9. Applied stress versus axial elastic phase stress for Cu-15%Mo at room temperature and 300°C. The stress in the Mo phase is larger for all values of stress at both temperatures. The Mo curve at room temperature is showing a decreasing slope, whereas the Mo curve at 300°C is showing an approximately constant slope. The Cu curve at room temperature is showing an increasing slope, whereas at high temperature it is decreasing slightly. The Cu phase carries higher stresses at high temperature.

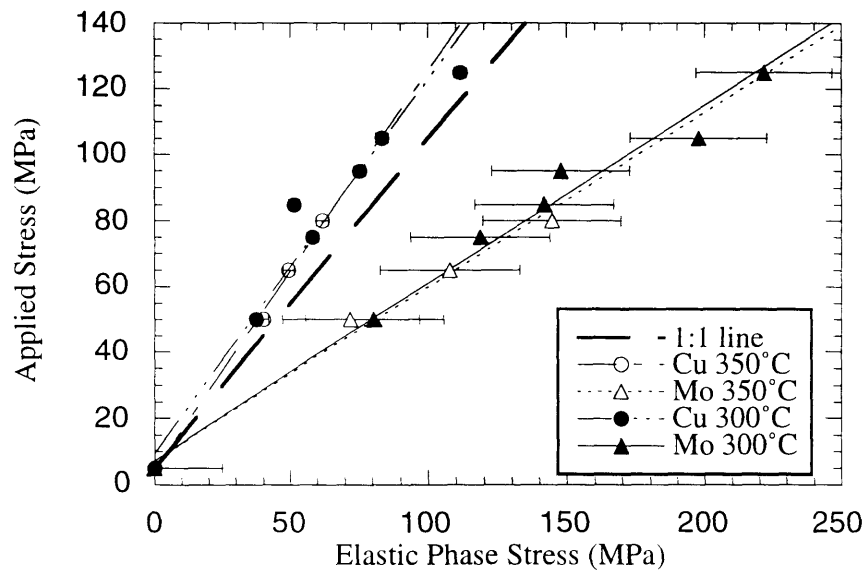


Figure 4.10. Applied stress versus axial elastic phase stress for Cu-15%Mo at 300° and 350°C. The stress in the Mo phase is larger for all values of stress at both temperatures. A straight line can be fitted through the Mo and Cu data at both temperatures.

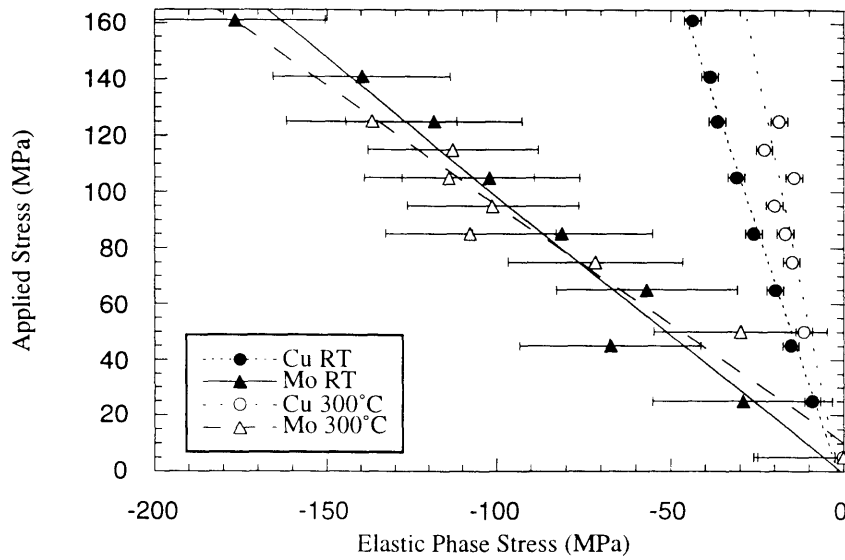


Figure 4.11. Applied stress versus transverse elastic phase stress for Cu-15%Mo at room temperature and 300°C. The stress in the Mo phase is more compressive for all values of stress at both temperatures. A straight line can be fitted through the Mo data at both temperatures, and there is little slope difference between the two lines.

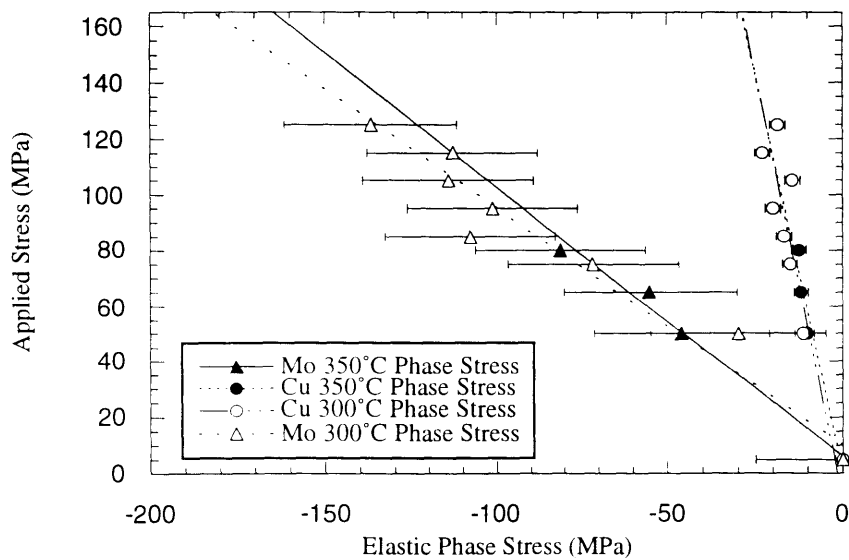


Figure 4.12. Applied stress versus transverse elastic phase stress for Cu-15%Mo at 300° and 350°C. The stress in the Mo phase is more compressive for all values of stress at both temperatures. A straight line can be fitted through the Mo data at both temperatures, and there is little slope difference between the two lines. Some fluctuations beyond error are seen in the Cu data.

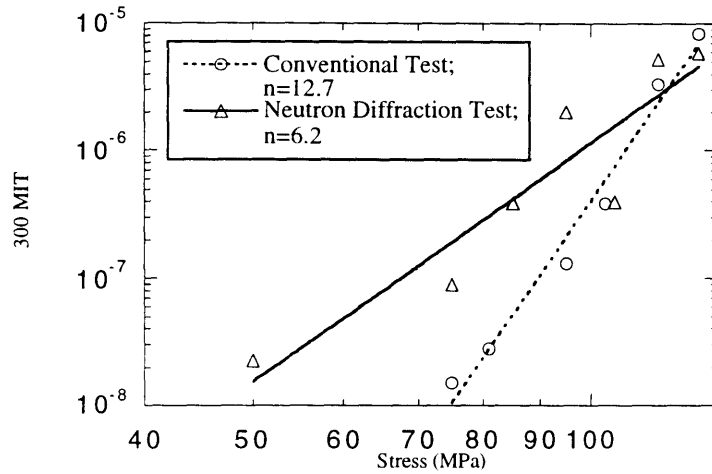


Figure 4.13. Creep data at 300°C from conventional creep testing compared with creep data from neutron diffraction experiments. The latter data is more scattered. Conventional creep testing results show lower strain rates for most stresses and an increased value of the stress exponent.

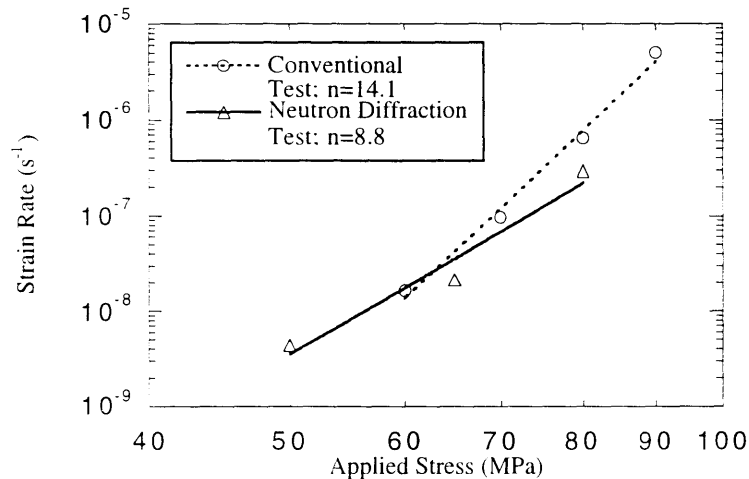


Figure 4.14. Creep data at 350°C from conventional creep testing compared with creep data from neutron diffraction experiments. The latter data is slightly more scattered. Conventional creep testing results show higher strain rates for most stresses and an increased value of the stress exponent.

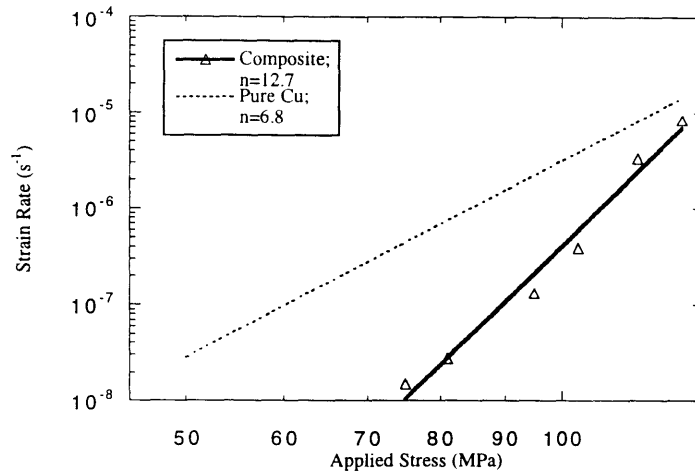


Figure 4.15. Creep data at 300°C from conventional creep testing of composite material compared with theoretical values for pure copper assuming power law creep (Frost & Ashby 1992). The strain rates are higher in Cu for all stresses studied. The stress exponent in pure Cu is 6.8, as compared to 12.7 in the composite.

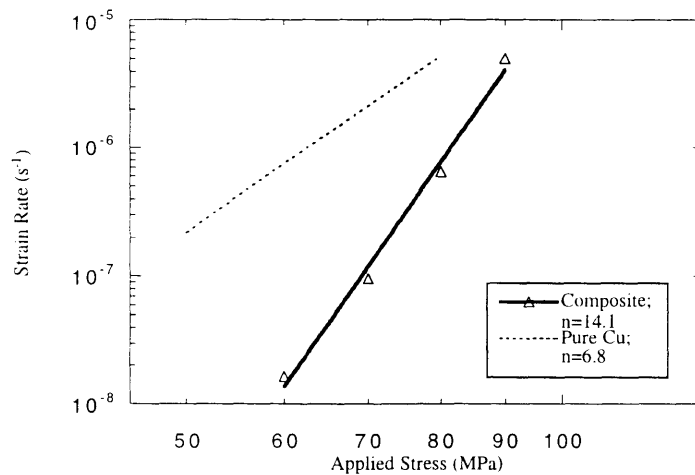


Figure 4.16. Creep data at 350°C from conventional creep testing of composite material compared with theoretical values for pure copper assuming power law creep (Frost & Ashby 1992). The strain rates are higher in Cu for all stresses studied. The stress exponent in pure Cu is 6.8, as compared to 14.1 in the composite.

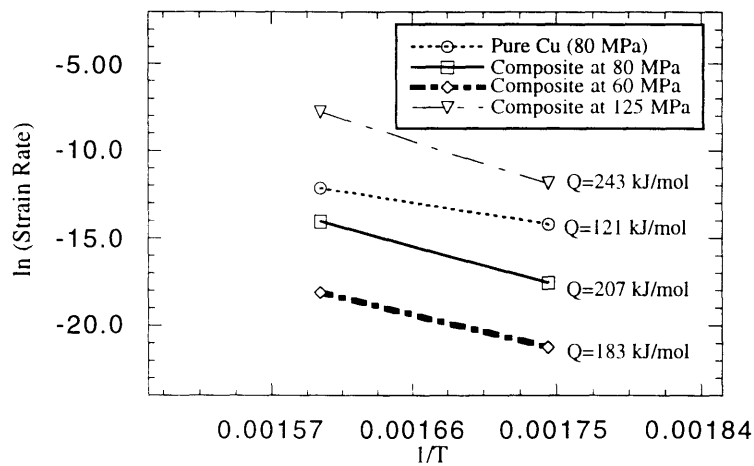


Figure 4.17. Plot of strain rate versus inverse absolute temperature, on a logarithmic-linear scale. The activation energy for Cu was calculated using Frost & Ashby 1992. The activation energy for the composite was found by relating strain rates at 60, 80 and 125 MPa. Since the stress exponents are dissimilar at the two temperatures, the value of the activation energy will range from 183-243 kJ/mol, for the given range of experimental stresses.

Chapter 4 Tables

Table 4.1. Room Temperature Mechanical Properties of Cu and Cu-15%Mo from Experiment.

Property:	Cu:	Cu-15%Mo	Increase
Elastic Modulus (GPa)	121	157	30 %
0.2% Yield Stress (MPa)	65	130	100 %

Table 4.2. Changes in Elastic Modulus with Temperature and Resulting Errors in Stress Calculation Given Strain Errors.

Property:	25°C	300°C	350°C
Cu Elastic Modulus (GPa)	121	108	105
Mo Elastic Modulus (GPa)	324	311	309
Error in Cu neutron strain	$2 \cdot 10^{-5}$	$2 \cdot 10^{-5}$	$2 \cdot 10^{-5}$
Error in Mo neutron strain	$8 \cdot 10^{-5}$	$8 \cdot 10^{-5}$	$8 \cdot 10^{-5}$
Error in Cu neutron stress (MPa)	2.4	2.2	2.1
Error in Mo neutron stress (MPa)	26	25	25

Table 4.3. Creep Properties of Copper and Molybdenum (Frost & Ashby 1982).

Material	Copper	Molybdenum
<i>Crystallographic and thermal data</i>		
Atomic volume, Ω (m ³)	1.18×10^{-29}	1.53×10^{-29}
Burgers vector, b (m)	2.56×10^{-10}	2.73×10^{-10}
Melting temperature, T_M (K)	1356	2883
<i>Modulus*</i>		
Shear modulus at 300 K μ_0 (MN/m ²)	4.21×10^4	1.34×10^5
Temperature dependence of modulus, $\frac{T_M d\mu}{\mu_0 dT}$	-0.54	-0.42
<i>Lattice diffusion†</i>		
Pre-exponential, D_{0v} (m ² /s)	2.0×10^{-5}	5.0×10^{-5}
Activation energy, Q_v (kJ/mole)	197	405
<i>Boundary diffusion†</i>		
Pre-exponential, δD_{0b} (m ³ /s)	5.0×10^{-13}	5.5×10^{-14}
Activation energy, Q_b (kJ/mole)	104	263
<i>Core diffusion†</i>		
Pre-exponential, $a_c D_{0c}$ (m ⁴ /s)	1.0×10^{-24}	1.0×10^{-22}
Activation energy, Q_c (kJ/mole)	117	263
<i>Power-law creep</i>		
Exponent, n	4.8	4.85
Dorn constant, ‡ A	7.4×10^5	1.0×10^8
P-L breakdown, α'	794	
<i>Obstacle-controlled glide</i>		
0 K flow stress, $\bar{\tau}/\mu_0$	6.3×10^{-3}	1.0×10^{-3}
Pre-exponential, $\dot{\gamma}_0$ (s ⁻¹)	10^6	10^6
Activation energy, $\Delta F/\mu_0 b^3$	0.5	0.5

$$* \mu = \mu_0 \left(1 + \frac{(T - 300)}{T_M} \right) \frac{T_M d\mu}{\mu_0 dT}$$

$$\dagger D_v = D_{0v} \exp - \frac{Q_v}{RT}; \delta D_b = \delta D_{0b} \exp - \frac{Q_b}{RT}; a_c D_c = a_c D_{0c} \exp - \frac{Q_c}{RT}$$

‡ This value of A refers to tensile stress and strain-rate. The maps relate shear stress and strain-rate.

5. NUMERICAL MODELING

5.1 Description of Finite Element Model

Finite element analysis was used to model the experimental results. A two-dimensional axisymmetric unit cell (Figure 5.1) was used, with second order focused elements. That implies that the variation of a certain property along a certain direction is quadratic with respect to distance. In order to model the steep stress gradient near the interface between the matrix and the reinforcement, a gradient of element density was introduced. Consequently, the element density was higher near the interface. Modeling the stress gradient accurately becomes particularly important in creep studies. The high value of the stress exponent in such cases indicates that the local deformation will be very sensitive to stress gradient and changes in stress. However, in averaging stresses over the entire volume of each phase, the effect of the stress gradient diminishes, as it is only important near the interface and not throughout the bulk of each phase.

The two-dimensional axisymmetric unit cell mesh is shown in Figure 5.1. As can be seen, a two-dimensional image of a quarter circle in the corner of a square models a sphere in a unit cylinder via rotational operations. The sphere represents the reinforcing Mo phase, while the rest of the cylinder represents the matrix Cu phase.

Materials properties were entered for pure Cu and pure Mo and are listed in Table 5.1. The values of concern were the coefficient of thermal expansion as function of temperature, the elastic modulus as a function of temperature, the plastic properties of the matrix; and the Poisson's ratio, which was assumed to be independent of temperature. The plastic properties

used for Cu corresponded to values obtained experimentally from the pure Cu sample (Figure 4.1 and Table 4.1). Plastic properties of Mo was obtained from Boyer 1987. Mo was assumed to be elastic-perfectly plastic (Boyer 1987). However due to the high flow stress, Mo was expected to remain well within the elastic regime for all values of applied stress. Elastic and creep data for both materials were obtained from Frost and Ashby (1982). Negligible strain rates (approximately 10^{-18} s^{-1}) in the Mo even at the maximum level of stress (125 MPa) indicated that the reinforcing phase would not creep. Coefficients of thermal expansion were obtained from the ASM Metals Handbook (Briggs 1987, Blackwood and Casteras 1987). Table 5.1 lists the relevant data.

The finite element modeling was performed by Dr. Mark Daymond, a co-worker in the strain group at Manuel Lujan Jr. Neutron Scattering Center at the Los Alamos National Laboratory, using the ABAQUS software package. The modeling was based on the author's specification of materials properties as described above.

5.2 Comparison of Finite Element Model and Experimental Results

Finite element models provide a wide range of potentially interesting data, including elastic, plastic and overall stresses and strains. Output may also include deviatoric or hydrostatic stress estimations. Additionally, maps of the distributions of these various properties throughout the unit cell may be obtained.

The main focus of the experimental work has been to obtain overall macroscopic stress and strain, as well as obtaining volume averaged elastic phase strains at various levels of applied stress. Accordingly, these were the output values of interest from the finite element modeling.

Figure 5.2 shows the overall stress-strain curve predicted for the Cu-15%Mo composite together with experimental stress-strain data. The experimental results show a higher stiffness, yield strength, and hardening rate than predicted by FEM.

Figures 5.3. and 5.4. show predicted and experimental room temperature phase strains in the axial and transverse directions, respectively. Satisfactory agreement is achieved in the axial direction (Figure 5.3). For Mo, the phase strain prediction is within the margin of error in the experimental measurement. The slope change seen at approximately 70 MPa is predicted at the correct stress. For Cu, the predicted curve shows a similar shape as the experimental curve, but is shifted to higher strains beyond the margin of error.

In the transverse direction (Figure 5.4), the predicted curve for Cu lies within the margin of error of the experimental curve, and shows the approximately the correct curvature. For Mo, while a straight line can be fitted through the experimental data, a distinct slope change is observed in the finite element model results. The experimental Mo strains are also much more compressive than the predicted strains. Furthermore, the model predicts higher compressive strains in Cu than in Mo, whereas the experimental results indicate the opposite.

Similar predictions and experimental results for steady state phase strains at 300°C are shown in Figures 5.5. and 5.6., in the axial and transverse directions, respectively. Satisfactory agreement is again achieved in the axial direction (Figure 5.5). For Mo, the phase strain prediction is within the margin of error in the experimental measurement, except for one data point. For Cu, the predicted curve shows a similar shape as the experimental curve, but is shifted to higher strains beyond the margin of error.

In the transverse direction (Figure 5.6), the FEM prediction for Mo lies within the margin of experimental error for most of the data points. Both curves show similar slopes and little slope change. For Cu the predicted strains are more compressive than the experimental ones, well beyond the margin of error.

Predictions and experimental results for steady state phase strains at 350°C are shown in Figures 5.7. and 5.8., in the axial and transverse directions, respectively. Good agreement is achieved in the axial direction (Figure 5.7). For Mo, the phase strain prediction is within the margin of error in the experimental measurement. For Cu, the predicted curve shows a similar shape as the experimental curve, but is shifted to higher strains beyond the margin of error.

In the transverse direction (Figure 5.8), the FEM prediction for Mo shows good agreement with the experimental results and lies well within the large margin of experimental error. Both curves show similar slopes and little slope change. For Cu the predicted strains are more compressive than the experimental ones, slightly beyond the margin of error. The curvature in the experimental curves contrast the approximately constant slope of the finite element predictions.

Chapter 5 Figures

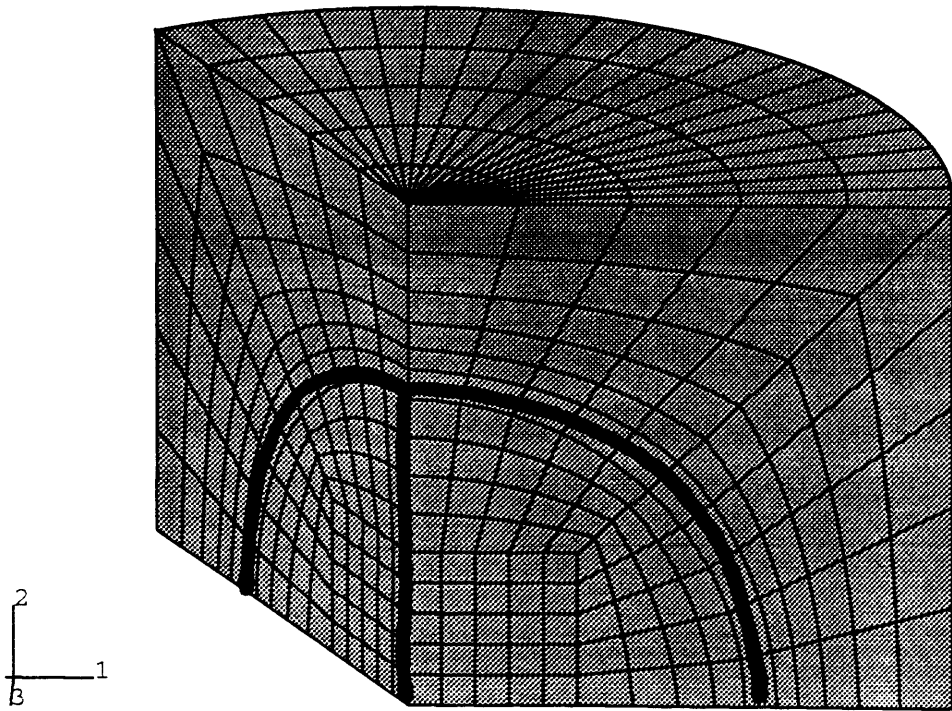


Figure 5.1. Two-dimensional axisymmetric finite element mesh used to model the behavior of the composite; showing a spherical particle (Mo) in a cylindrical matrix unit (Cu).

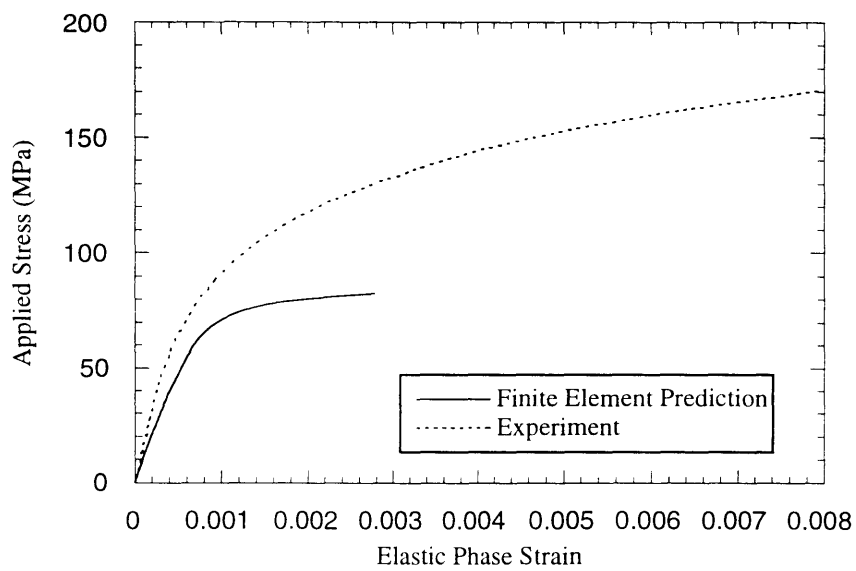


Figure 5.2. Numerical prediction from finite element analysis of room temperature stress-strain behavior of the Cu-15%Mo composite. As shown from the experimental curve, the model underestimates the strengthening observed experimentally.

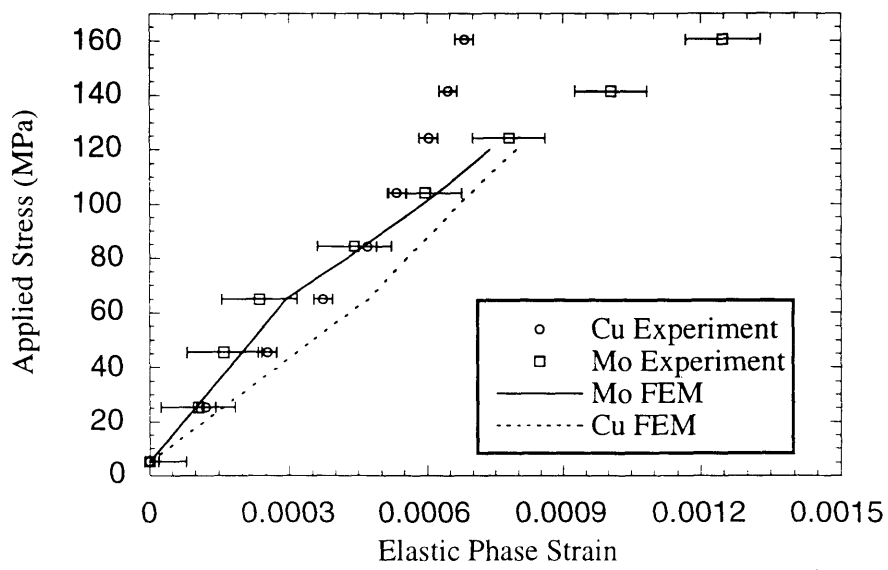


Figure 5.3. Comparison of finite element predictions with experimental results for the evolution of axial elastic phase strains with applied stress at room temperature.

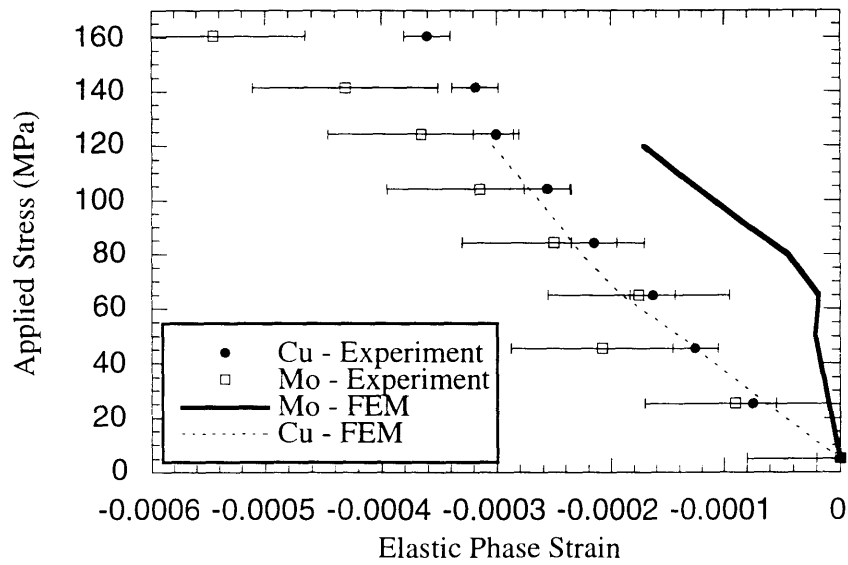


Figure 5.4. Comparison of finite element predictions with experimental results for the evolution of transverse elastic phase strains with applied stress at room temperature.

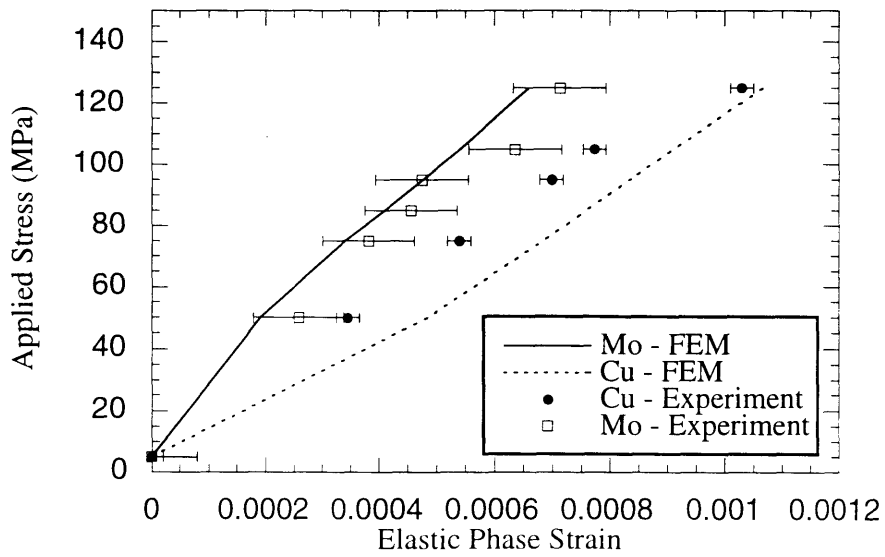


Figure 5.5. Comparison of finite element predictions with experimental results for the evolution of axial elastic phase strains with applied stress at 300°C.

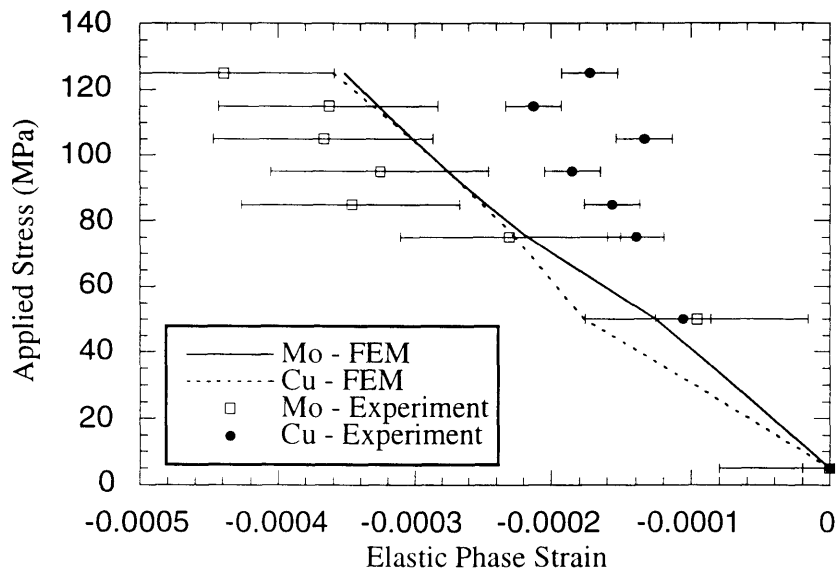


Figure 5.6. Comparison of finite element predictions with experimental results for the evolution of transverse elastic phase strains with applied stress at 300°C.

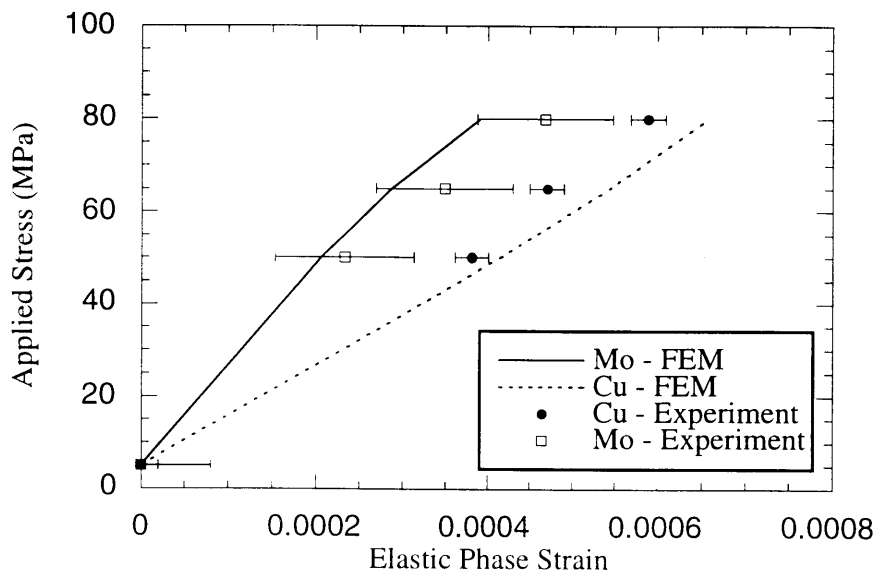


Figure 5.7. Comparison of finite element predictions with experimental results for the evolution of axial elastic phase strains with applied stress at 350°C.

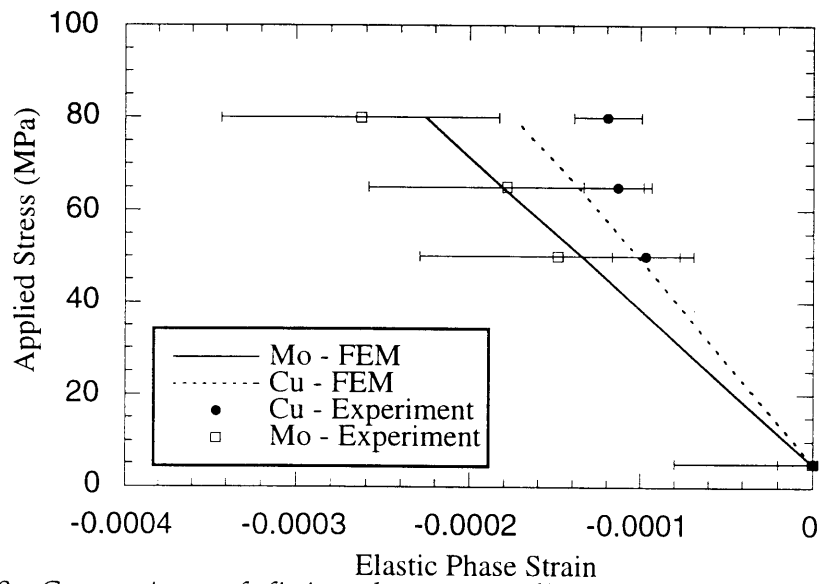


Figure 5.8. Comparison of finite element prediction with experimental results for the evolution of transverse elastic phase strains with applied stress at 350°C.

Table 5.1. Materials properties used in finite element model.

A, Mo Elastic Properties

Elastic modulus (MPa), Poisson's ratio, temperature (°C)

346.62E3,0.293,25
345.27E3,0.29266,50
343.92E3,0.29233,75
342.57E3,0.29199,100
341.22E3,0.29165,125
339.87E3,0.29132,150
338.52E3,0.29098,175
337.17E3,0.29064,200
335.83E3,0.29031,225
334.48E3,0.28997,250
333.13E3,0.28963,275
331.79E3,0.2893,300
330.44E3,0.28896,325
329.1E3,0.28862,350
327.76E3,0.28829,375
326.41E3,0.28795,400
325.07E3,0.28761,425
323.73E3,0.28728,450
322.39E3,0.28694,475
321.05E3,0.2866,500
319.71E3,0.28627,525
318.37E3,0.28593,550
317.03E3,0.28559,575
315.7E3,0.28526,600
314.36E3,0.28492,625
313.02E3,0.28458,650
311.69E3,0.28425,675
310.35E3,0.28391,700

B. Mo Coefficient of Thermal Expansion (CTE)

CTE (K⁻¹), temperature (°C)

5.E-6, 25.
5.E-6, 300.
6.E-6, 400.
6.E-6, 1000.

C. Mo Plastic Properties

Stress (MPa), Plastic Strain, Temperature (°C)

650., 0., 25.
650., 0.2, 25.

Table 5.1. Materials properties used in finite element model. Continued

A, Cu Elastic Properties

Elastic Modulus (MPa), Poisson's ratio, Temperature (°C)

113.17E3, 0.343, 25
111.97E3, 0.34208, 50
110.77E3, 0.34116, 75
109.57E3, 0.34024, 100
108.37E3, 0.33932, 125
107.17E3, 0.3384, 150
105.98E3, 0.33748, 175
104.78E3, 0.33655, 200
103.59E3, 0.33563, 225
102.4E3, 0.33471, 250
101.21E3, 0.33379, 275
100.03E3, 0.33287, 300
98.841E3, 0.33195, 325
97.657E3, 0.33103, 350
96.474E3, 0.33011, 375
95.293E3, 0.32919, 400
94.114E3, 0.32827, 425
92.936E3, 0.32735, 450
91.76E3, 0.32643, 475
90.585E3, 0.32551, 500
89.412E3, 0.32459, 525
88.24E3, 0.32366, 550
87.07E3, 0.32274, 575
85.901E3, 0.32182, 600
84.734E3, 0.3209, 625
83.568E3, 0.31998, 650
82.404E3, 0.31906, 675
81.242E3, 0.31814, 700

B. Cu Coefficient of Thermal Expansion (CTE)

CTE (K⁻¹), Temperature (°C)

16.7E-6, 20.
17.3E-6, 77.
17.6E-6, 127.
18.3E-6, 227.
18.9E-6, 327.
19.6E-6, 427.
20.4E-6, 527.
22.4E-6, 727.
24.8E-6, 927.

Table 5.1. Materials properties used in finite element model. Continued

C. Cu Plastic Properties

Stress (MPa), Plastic Strain, Temperature (°C)

63.4, 0., 25.	79.37, 8.3172e-3, 25.
63.92, 1.1086e-4, 25.	79.43, 8.4606e-3, 25.
64.46, 2.1515e-4, 25.	79.79, 8.8191e-3, 25.
65.27, 4.3025e-4, 25.	80.27, 9.1255e-3, 25.
65.68, 5.6713e-4, 25.	81.01, 9.6469e-3, 25.
66.17, 6.8446e-4, 25.	81.33, 9.9533e-3, 25.
66.42, 7.8223e-4, 25.	81.55, 1.0247e-2, 25.
66.94, 9.1259e-4, 25.	81.74, 1.0364e-2, 25.
67.52, 1.1603e-3, 25.	82.32, 1.0683e-2, 25.
67.93, 1.2841e-3, 25.	82.68, 1.099e-2, 25.
68.29, 1.4145e-3, 25.	83., 1.1283e-2, 25.
68.61, 1.5579e-3, 25.	83.32, 1.1609e-2, 25.
69.25, 1.8317e-3, 25.	83.74, 1.1889e-2, 25.
69.6, 1.962e-3, 25.	84.06, 1.2215e-2, 25.
69.86, 2.1119e-3, 25.	84.15, 1.2352e-2, 25.
70.12, 2.2553e-3, 25.	84.67, 1.2658e-2, 25.
70.47, 2.3987e-3, 25.	84.99, 1.2978e-2, 25.
70.73, 2.5356e-3, 25.	85.38, 1.3327e-2, 25.
71.40, 2.8159e-3, 25.	85.66, 1.3519e-2, 25.
71.63, 2.9658e-3, 25.	85.92, 1.3682e-2, 25.
71.72, 3.1092e-3, 25.	86.08, 1.3838e-2, 25.
71.98, 3.2722e-3, 25.	86.43, 1.421e-2, 25.
72.33, 3.4286e-3, 25.	86.63, 1.4425e-2, 25.
72.69, 3.7089e-3, 25.	87.13, 1.4907e-2, 25.
73.07, 3.8458e-3, 25.	87.4, 1.5083e-2, 25.
73.27, 4.0087e-3, 25.	87.72, 1.5226e-2, 25.
73.49, 4.1521e-3, 25.	87.78, 1.5383e-2, 25.
73.84, 4.3216e-3, 25.	87.94, 1.5546e-2, 25.
74.29, 4.6214e-3, 25.	88.40, 1.5865e-2, 25.
74.26, 4.7648e-3, 25.	88.52, 1.6054e-2, 25.
74.68, 4.9278e-3, 25.	88.68, 1.6198e-2, 25.
74.84, 5.0842e-3, 25.	89.04, 1.6348e-2, 25.
75.1, 5.2341e-3, 25.	89.16, 1.6498e-2, 25.
75.51, 5.5405e-3, 25.	89.36, 1.6797e-2, 25.
75.77, 5.6969e-3, 25.	89.45, 1.6947e-2, 25.
76.0, 5.8403e-3, 25.	89.97, 1.7104e-2, 25.
76.19, 5.9968e-3, 25.	89.77, 1.7241e-2, 25.
76.35, 6.1532e-3, 25.	90.03, 1.7391e-2, 25.
76.86, 6.4661e-3, 25.	90.42, 1.771e-2, 25.
76.93, 6.6225e-3, 25.	90.48, 1.786e-2, 25.
77.59, 6.9797e-3, 25.	90.67, 1.801e-2, 25.
78.05, 7.3395e-3, 25.	90.35, 1.8088e-2, 25.
78.34, 7.6524e-3, 25.	289, .2, 25
78.93, 7.9897e-3, 25.	40, 0, 400
79.05, 8.1543e-3, 25.	50, .002, 400
	200, .2, 400

Table 5.1. Materials properties used in finite element model. Continued

D. Cu Creep Properties

Pre-Exponential, Stress Exponent n, Stress (MPa), Temperature (°C)

4.33999E-15, 5.30948, 0.00000, 300.000
2.37591E-14, 5.12241, 0.00000, 350.000
8.83197e-13, 4.87866, 0.00000, 500.000
1.07401e-12, 4.87234, 0.00000, 510.000
1.26483e-12, 4.86602, 0.00000, 520.000
1.54472e-12, 4.86042, 0.00000, 530.000
2.03244e-12, 4.85650, 0.00000, 540.000
2.52016e-12, 4.85258, 0.00000, 550.000
3.00788e-12, 4.84866, 0.00000, 560.000
3.49560e-12, 4.84474, 0.00000, 570.000
4.17403e-12, 4.84124, 0.00000, 580.000
5.29747e-12, 4.83872, 0.00000, 590.000
6.42091e-12, 4.83620, 0.00000, 600.000
7.54435e-12, 4.83368, 0.00000, 610.000
8.66779e-12, 4.83116, 0.00000, 620.000
1.01675e-11, 4.82891, 0.00000, 630.000
1.25453e-11, 4.82727, 0.00000, 640.000
1.49230e-11, 4.82563, 0.00000, 650.000
1.73008e-11, 4.82399, 0.00000, 660.000
1.96786e-11, 4.82235, 0.00000, 670.000
2.27498e-11, 4.82086, 0.00000, 680.000
2.74392e-11, 4.81974, 0.00000, 690.000
3.21286e-11, 4.81862, 0.00000, 700.000
3.68180e-11, 4.81750, 0.00000, 710.000
4.15074e-11, 4.81638, 0.00000, 720.000
4.74018e-11, 4.81537, 0.00000, 730.000
5.61078e-11, 4.81461, 0.00000, 740.000
6.48138e-11, 4.81385, 0.00000, 750.000
7.35198e-11, 4.81309, 0.00000, 760.000
8.22258e-11, 4.81233, 0.00000, 770.000
9.29214e-11, 4.81164, 0.00000, 780.000
1.08259e-10, 4.81110, 0.00000, 790.000
1.23597e-10, 4.81056, 0.00000, 800.000
1.38935e-10, 4.81002, 0.00000, 810.000
1.54273e-10, 4.80948, 0.00000, 820.000
1.72754e-10, 4.80898, 0.00000, 830.000
1.98566e-10, 4.80858, 0.00000, 840.000
2.24378e-10, 4.80818, 0.00000, 850.000
2.50190e-10, 4.80778, 0.00000, 860.000
2.76002e-10, 4.80738, 0.00000, 870.000
3.10074e-10, 4.80702, 0.00000, 880.000
3.63422e-10, 4.80677, 0.00000, 890.000
4.16770e-10, 4.80652, 0.00000, 900.000

6. DISCUSSION

6.1 Room Temperature Behavior

6.1.1 Macroscopic Behavior

A tensile yield strength increase of 100%, a stiffness increase of 30%, and significant strain hardening was exhibited by the composite as compared to the unreinforced copper. Effective composite strengthening was confirmed by the neutron diffraction data, as described in the next section.

Finite element modeling of the composite stress-strain curve provides an underestimation of its overall macroscopic mechanical properties. A possible explanation is that the mechanical properties of the matrix are different than those of the pure Cu control sample. The possibility of the presence of other strengthening mechanisms than composite strengthening were therefore investigated for the composite.

Transmission Electron Microscopy studies of the as-processed material have been performed by Dr. Christian Verdon at MIT (Verdon 1997). The results from these studies show that significant pinning of dislocations is evident. The pinning must be due to either other dislocations (forest hardening), precipitates (precipitation strengthening), or oxide dispersoids (oxide dispersion strengthening). Forest hardening could not alone provide the degree of strengthening seen. The possibility of precipitation strengthening or dispersion strengthening was therefore investigated.

The phase diagrams currently available for the Cu-Mo system indicates no mutual solid solubility (Subramanian & Laughlin 1990). However slight solubility of Mo in Cu at the processing temperature could have led to some

diffusion of Mo into the matrix. During cooling, supersaturation would lead to the formation of Mo precipitates in the Cu matrix. Precipitation formation would cause pinning of dislocation, thus leading to precipitation strengthening of the matrix, in turn leading to strengthening of the composite beyond composite strengthening. It is possible that slight solubilities may exist at high temperature. The experimental techniques used to establish the phase diagram could lack the resolution to establish these potentially very small but finite solubilities. If the precipitates were small enough, their presence could not be determined using TEM.

The samples were fabricated using a powder metallurgical technique involving hot isostatic pressing (HIPing). Copper powder in air at room temperature is very prone to oxide formation. Powder metallurgical techniques do often cause oxide to be included in the material due to its presence as a coating on particles. This has often been seen in aluminum matrix composites processed in this manner (Dunand and Derby 1993). If oxide dispersion strengthening were to have occurred, it must have been related to the introduction of molybdenum. Indeed, the pure copper samples, processed in the same way as the composites, show no indication of dispersion strengthening.

Although the copper and molybdenum powders were reduced in an H_2 atmosphere just prior to HIPing, some oxide may have remained on the surface of the molybdenum particles. However, the Ellingham diagram in Figure 6.1. confirms that both Cu_2O , but not MoO_2 , would be reduced by the H_2 gas. Since MoO_2 is more stable than the copper oxides, copper oxide would not form from the MoO_3 . The line for CuO is not shown in Figure 6.1, but Reed (1971) shows it to lie above the line for Cu_2O . This would indicate that CuO is even less stable than Cu_2O and would also be reduced by H_2 .

6.1.2 Microscopic Behavior

For applied stresses below the onset of matrix microyielding, the load partitioning remains constant, as evidenced by a linear evolution of axial elastic phase strain with applied stress. The copper phase strains are lower than the copper bulk elastic response, and the molybdenum phase strains are higher, thus indicating that elastic load transfer occurred from the matrix to the reinforcement. As expected from its higher stiffness, molybdenum reinforcement phase is carrying a higher proportion of the total applied stress than the copper matrix phase. The linearity of the strain evolution indicates however that the proportion of load carried by each phase remains constant. No modeling of this load transfer (Clyne and Withers 1993) was attempted.

Upon microyielding, however, significant further load transfer occurs from the matrix to the reinforcement, as evidenced by a more rapid increase in reinforcement axial elastic phase strains with applied stress. At the same time, the matrix axial elastic phase strains are increasing at a slower rate. The portion of the load carried by the reinforcement is in other words increasing beyond the elastic load transfer with applied stress after matrix microyielding has occurred.

As the matrix starts yielding, its ability to carry load becomes much reduced, thus spurring plastic load transfer to the reinforcement, which, with its higher strength, can carry load more efficiently. Given the theoretical values of yield stress for molybdenum of 650 MPa (Metals Handbook), and the experimental maximum phase stress of 403 MPa, the reinforcement remains elastic for all stresses applied in this study. Its ability to carry load elastically is therefore maintained.

In the transverse direction, the results are less conclusive. The molybdenum phase strains are more compressive than the copper phase strains, thus indicating that the reinforcement is becoming more laterally compressed than the matrix. The Poisson's ratios of Cu and Mo are 0.343 and 0.293, respectively. This would contribute to a compressive stress in the reinforcement. No significant changes in slopes of the curves are present. It is not unusual, however, that transverse phase strains provide less useful information than the axial phase strains (Bourke 1996).

Finite element modeling is providing an accurate prediction of qualitative trends of the microscopic axial elastic phase strain evolution with increasing applied stress. The increased load transfer upon matrix microyielding and the resulting slope change is predicted at the correct stress, but shifted to a higher phase strain. For the Mo reinforcement, there is quantitative agreement within the relatively large error of the measurement for axial values. Transverse strain values show larger discrepancies for Mo, although the Cu phase strain is accurately predicted within error.

The discrepancies could be caused by an inaccurate representation of the composite microstructure by the mesh in the finite element model. The mesh assumes evenly distributed spherical Mo particles of the same size in the Cu matrix (Figure 5.1). However, the micrographs shown in Figures 3.5 and 3.6 indicate that the particles are irregular rather than spherical, that there is variation in particle size, and that clustering of particles occurs.

6.2 High Temperature Behavior

6.2.1 Macroscopic Behavior

Creep rates obtained by conventional creep testing show stress exponents of 13 and 14 at 300° and 350°C, respectively. These stress exponents are much higher than what is observed in pure copper. At these temperatures pure copper is in a low temperature power-law regime, indicating that the observed stress exponent is equal to $n + 2$, where n is the true stress exponent equal to 4.8.

While an exact activation energy cannot be determined with two data points, a broad range of 183 - 243 kJ/mol was found. It is clear that, as for n , the activation energy is much higher in the composite than in the pure copper, equal to 121 kJ/mol (Frost and Ashby 1982).

The creep rates determined without extensometer during the neutron diffraction experiments are significantly different from the ones obtained by conventional creep testing with extensometer. At 300°C they are significantly higher, and at 350°C they are significantly lower. The creep data collected during diffraction shows that the strain rate is decreasing slightly when the temperature is increased. This is clearly anomalous. It is believed that the error in these creep measurements is due to the lack of a high-temperature extensometer. If creep occurred in components other than the sample or if thermal expansion occurred in the load train, the creep rates measured would be inaccurate. In any case, the conventional creep testing followed standard procedures and strains were believed to be measured accurately with an extensometer.

The composite material shows improved creep resistance as compared to pure Cu in the range of stresses involved in this study. Lower creep rates are achieved for the composite at both 300°C and 350°C as compared to the theoretical predictions for pure copper (Frost and Ashby 1982). However the higher stress exponent indicates that creep has become more stress-sensitive.

A large increase in composite stress exponents and activation energies over the matrix metal or alloy has been found by many researchers as described in Section 2.1.3. This has however often been attributed to dispersion strengthening of the matrix in addition to the presence of composite strengthening. The issues of oxide dispersion strengthening was discussed in Section 6.1.1. As discussed there, oxide dispersion strengthening is not likely in this material. A fine distribution of Mo precipitates in the matrix may be present as described in Section 6.1.1. This could lead to the introduction of a threshold stress, below which no creep occurs, and above which the apparent stress exponent is very high. Slope change, which would indicate a change in stress exponents, was not observed in the double logarithmic plots of strain rate versus applied stress. However it is possible that the threshold stress is below the stresses probed in this study, thus implying that a threshold stress still may exist to explain the high stress exponents observed.

Using the deformation mechanism map for pure copper of a typical grain size of 0.1 mm, shown in Figure 6.2, and the materials properties listed in Table 4.3, it can be determined that a critical stress exists at 82 MPa at 300°C and 80 MPa at 350°C. Below the critical stress, there is low-temperature power law creep, whereas above it there is power law breakdown. The calculations are shown in Appendix 2. This would indicate that for copper, at any value of

stress above the critical stress, the power law breakdown regime is entered thus causing creep rates much higher than predicted from the power law relationship.

Shown in Figure 6.3 are the copper phase stresses observed via neutron diffraction at elevated temperatures. If no strengthening mechanism other than composite strengthening were available, power law breakdown would be expected when the copper phase stress exceeds the critical values. The phase stresses are consistently less than the applied stress, as expected from load transfer. At 300°C, the copper phase stress exceeds the critical stress for power law breakdown (82 MPa) at an applied stress of 105 MPa (Appendix).

Examining the creep rates obtained (Figures 4.15 and 4.16), it is clear that the rates obtained at higher values of stress are indeed higher than would be predicted by a power law fit to the remaining data. In other words the power law fit excluding the higher stress values would provide lower stress exponents than the ones currently reported. To illustrate this point, Figure 6.4 shows a power law fit that excludes the data collected at 105 MPa or higher. The stress exponent is reduced to 10 at 300°C. No data was collected above 90 MPa at 350°C so the stress exponent at 350°C remains unaffected at 14. Now the discrepancy in stress exponents at these two temperatures has increased from 1 to 4.

The phase stresses in the copper matrix are shown in Figure 6.3. By relating these phase stresses to the corresponding overall steady state creep strain rates, new stress exponents were obtained (Figures 6.5 and 6.6) at both 300°C and 350°C. At 300°C this procedure yields a stress exponent of 11, as compared to 13 when using applied stresses rather than phase stresses. At 350°C, the stress exponent decreases from 14 to 13. The fact that the stress

exponents remain high provides evidence that the high initially determined stress exponent is not due to load transfer, but to some intrinsic strengthening mechanism in the matrix. Such strengthening could have been caused by Mo precipitates in the matrix, as discussed in Section 6.1.1.

6.2.2 Microscopic Behavior

At 300°C as well as 350°C, there are few changes in load partitioning with increasing applied stress (Figures 4.5 and 4.7). A constant load partitioning would indicate that the efficiency of the plastic load transfer is much reduced. There is no evidence that the reinforcement is carrying progressively higher proportions of the total load, which would have been indicated by slope changes in the phase strain curves. No significant slope changes are observed. Indeed a straight line can be fitted through the reinforcement axial phase strain curves at both 300°C and 350°C within the margin of experimental error (Figures 4.5 and 4.7). While at room temperature the reinforcement remained elastic when the matrix was plastically deforming with strong strain hardening, at high temperature the reinforcement again remained elastic while the matrix was deforming by creep.

This contrasts the room temperature results, which indicate that significant plastic load transfer occurs from the matrix to the reinforcement, as evidenced by the rapidly increasing reinforcement axial phase strains and the diminishing rate of increase of the matrix axial phase strain. The less efficient plastic load transfer at 300°C and 350°C is most probably due to creep of the matrix at elevated temperature around the particle reinforcement. This

creeping plastic zone cannot transfer load efficiently and therefore reduces the extent of plastic load transfer between the matrix and reinforcement.

The finite element model is in qualitative agreement with the experimental results in the axial direction. For the reinforcement, there is also quantitative agreement within the margin of error. The model accurately predicts the trend observed in the experiment in that little load transfer is observed at elevated temperatures as compared to efficient load transfer at room temperature. The discrepancies between the model predictions and the experimental results may again be caused by an inaccurate representation of the matrix microstructure by the finite element mesh as described in Section 6.1.2.

The experimental results and the numerical predictions in the transverse direction are more difficult to interpret. The reinforcement is becoming constrained by the flow of the matrix and therefore the reinforcement phase strains are highly compressive. Creeping or plastically deforming copper has an effective Poisson's ratio of 0.5 by conservation of volume, while the elastic Mo Poisson's ratio is 0.293 (Meyers & Chawla). This indicates that the matrix will contract more than the reinforcement and will cause compressive stresses in the reinforcement. For Mo, good agreement is shown between the prediction and the experimental results within the margin of error. For Cu, however, higher compressive strain are predicted than observed well beyond the margin of error.

Chapter 6 Figures

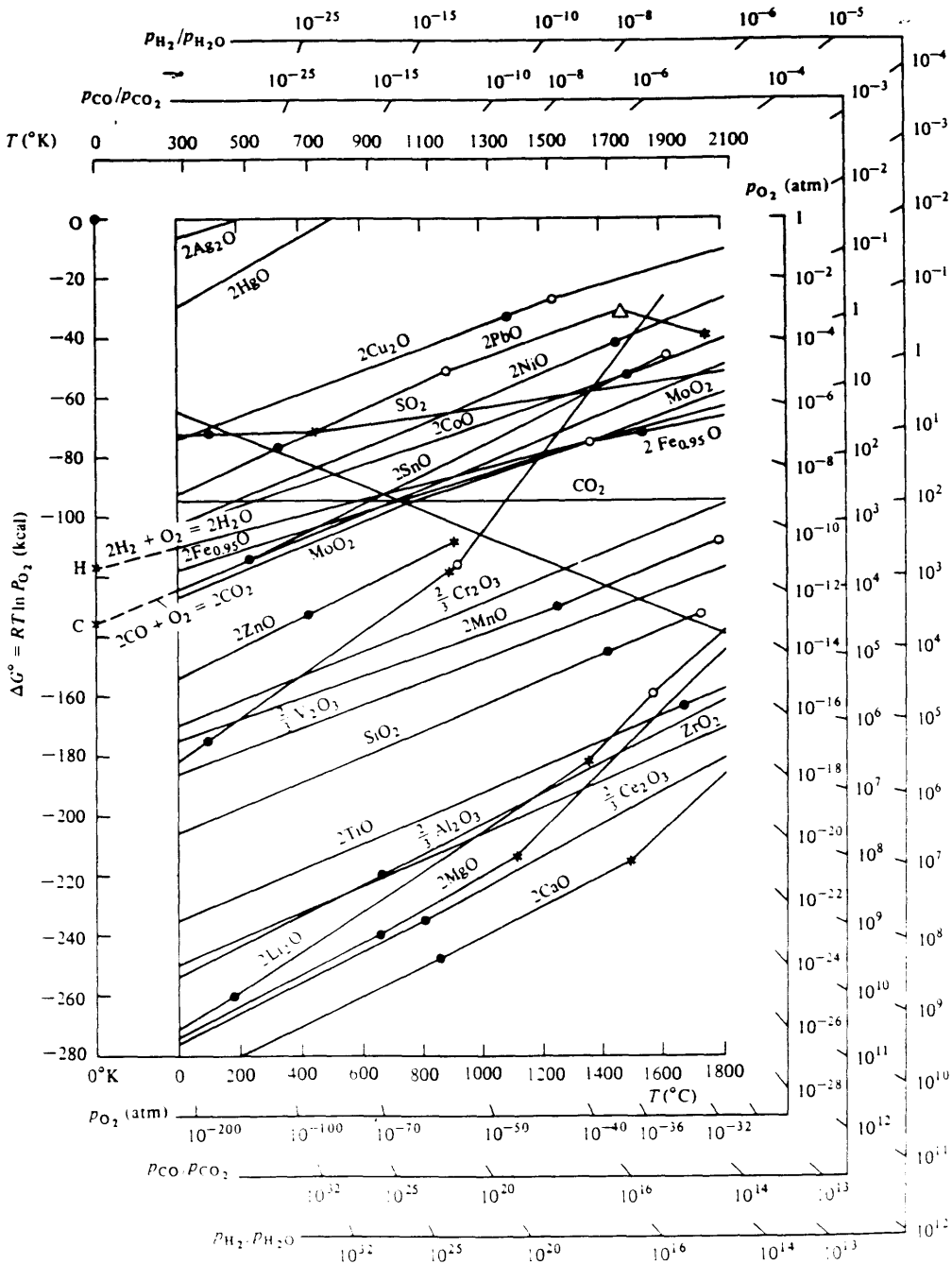


Figure 6.1. Ellingham diagram showing the standard free energy of formation of selected oxides. Stability increases downwards in the diagram. Consequently, cupric oxide Cu_2O is less stable than MoO_2 and water H_2O for all temperatures (Lupis 1983). MoO_2 however is more stable than water H_2O . Thus hydrogen is expected to reduce Cu_2O but not MoO_2 .

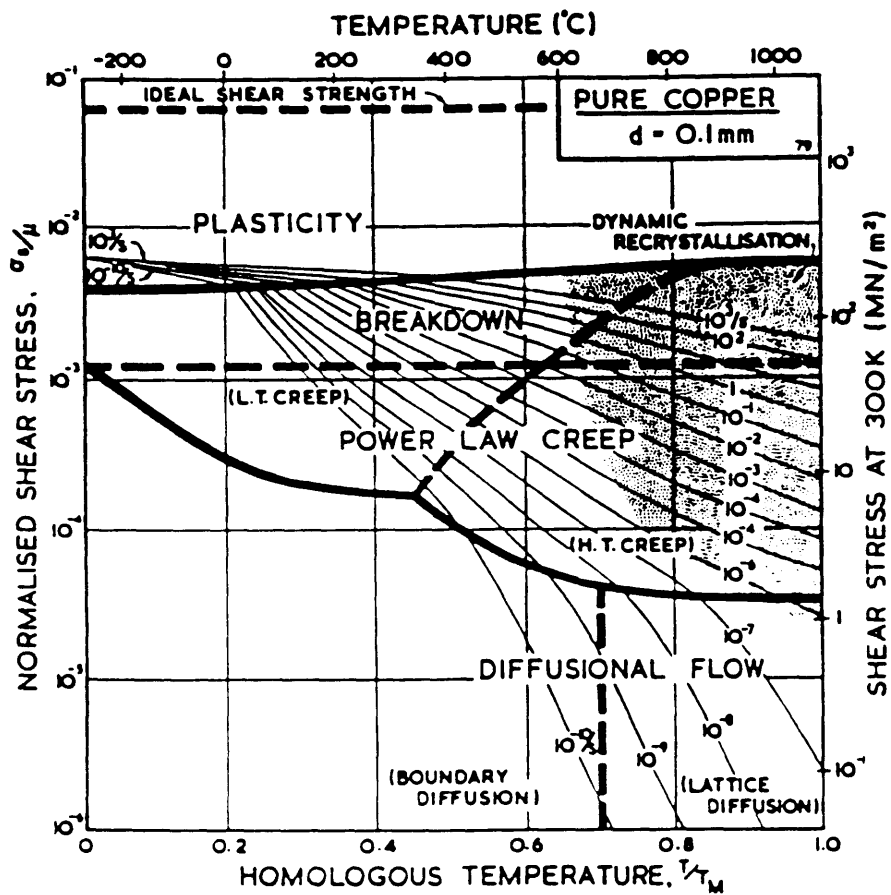


Figure 6.2. Deformation mechanism map for pure copper of grain size 0.1 mm. The power law breakdown region is entered at 82 MPa for 300°C, and at 80 MPa at 350°C (Frost & Ashby 1982).

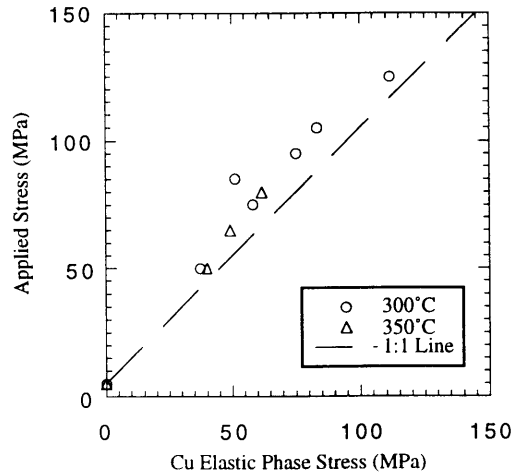


Figure 6.3. Applied stress versus copper matrix phase stresses determined by neutron diffraction. All phase stresses are less than the applied stress due to the load sharing in the composite.

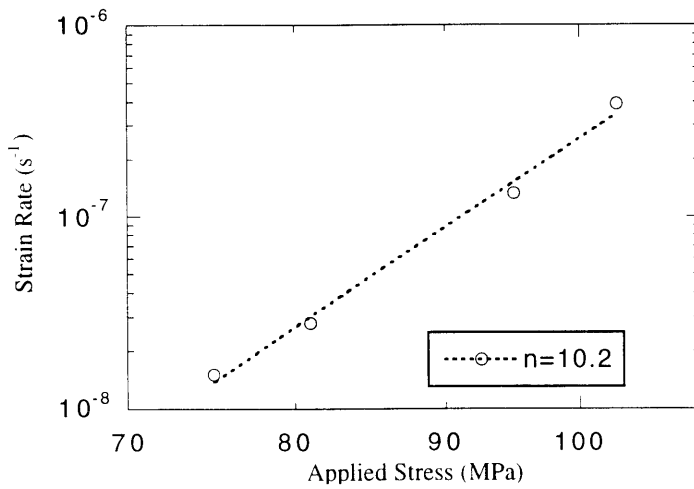


Figure 6.4. Strain rate versus applied stress at 300°C. Stress values of 115 MPa and above are omitted to yield lower stress exponents than previously found. The stress exponent is reduced to 10 from 13.

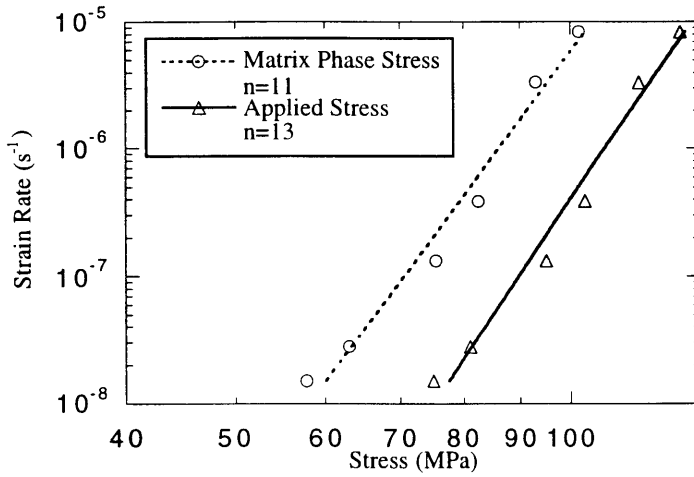


Figure 6.5. Strain rate versus copper matrix phase stress at 300°C. The stress exponent is now 11, as compared to 13 when applied stresses are used.

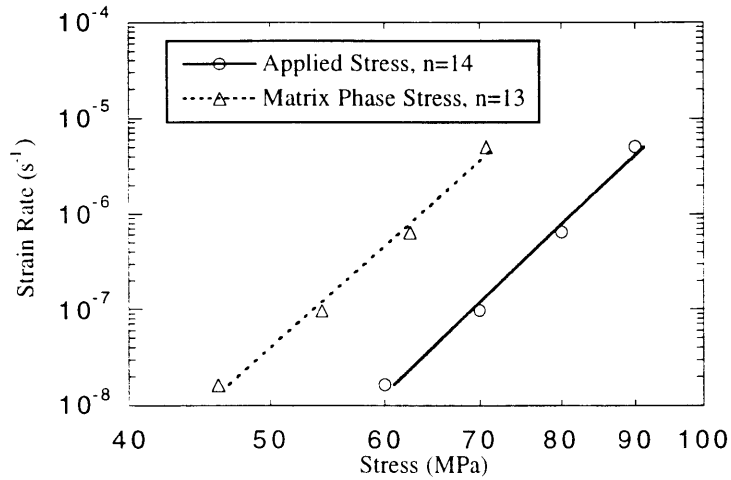


Figure 6.6. Strain rate versus copper matrix phase stress at 350°C. The stress exponent is now 13, as compared to 14 when applied stresses are used.

7. CONCLUSION

Pure copper reinforced with 15% molybdenum particulates by volume was fabricated using hot isostatic pressing. The resulting microstructure shows a moderate clustering of the molybdenum particulates and only a few voids. Conventional mechanical tensile testing was performed at room temperature, yielding stress-strain curves for both pure copper and composite samples. In-situ loading neutron diffraction experiments were performed during static loading at room temperature and during steady state creep at 300°C and 350°C yielding phase strains in both the reinforcement and matrix as a function of the applied stress. Conventional creep testing was also performed at the same temperatures, yielding steady state creep rates, stress exponents and activation energies. Finite element modeling was performed to provide a prediction of the experimental results.

Load transfer is evident in the composite at both room- and elevated temperatures, and is the basic mechanism for composite strengthening. At room temperature, elastic load transfer is followed by efficient plastic load transfer upon matrix microyielding. At elevated temperature, plastic load transfer is much less efficient, but elastic load transfer is still evident.

The presence of molybdenum precipitates in the matrix could explain the increased strengthening in the composite observed experimentally as compared to finite element modeling of the stress-strain curve. Oxide dispersion strengthening is not likely to have occurred.

High apparent stress exponents (13 and 14) and activation energies (183-243 kJ/mol), as compared to pure copper, could be caused by either the introduction of a threshold stress due to the presence of molybdenum precipitates in the matrix, or due to the onset of power law breakdown. The

matrix phase stress is lower than the applied stress due to load transfer, but not low enough to exclude the possibility of power law breakdown.

Stress exponents obtained using matrix phase stresses are only slightly lower than the ones obtained using applied stresses (from 13 and 14 to 11 and 13, respectively). Evidence is thus provided that the high stress exponents are due to the properties of the matrix and not to load transfer.

The finite element predictions of the stress-strain curve at room temperature indicate that there is matrix strengthening that renders the plastic matrix materials data input inaccurate. Finite element modeling results are in good agreement with the microscopic experimental results at both room- and elevated temperature. The discrepancies present are most likely due to differences between the material microstructure and the finite element meshing seeking to represent it.

8. SUGGESTIONS FOR FUTURE WORK

- Future work may involve a more detailed study of the microstructure to more accurately determine the origins of matrix strengthening.

- Finite element modeling could be attempted using different meshes accounting more accurately for the composite microstructure.

- By varying the volume fraction or shape of the reinforcement, the effect on load transfer could be studied. For example, 7.5% or 25% volume fractions could be tested. Discontinuous fibers could be used instead of particulates.

- One could attempt to use a high temperature extensometer during the in-situ loading neutron diffraction measurements. In this way accurate strains could be obtained directly, and would allow for more careful control of the experiment.

- Fracture surfaces could be studied using SEM fractography techniques.

Appendix 1. Determining the Steady-State Creep Stress Exponent and the Activation Energy.

Eqn. 1, introduced in Section 2.1.2, describes the relationship between the shear strain rate and the shear stress:

$$\dot{\gamma} = AD_{\text{eff}} \frac{\mu b}{kT} \left(\frac{\sigma_s}{\mu} \right)^n \quad (\text{A1})$$

The explanation of the different constituents of this equation can be found in Section 2.1.2. From this equation the relationship between the applied tensile stress and the steady-state creep strain rate can easily be deduced (Frost and Ashby 1982):

$$\dot{\epsilon} = K_{\text{PL}} \sigma^n \quad (\text{A2})$$

where $\dot{\epsilon}$ is the steady-state creep strain rate, K_{PL} is a constant, σ is the applied stress, and n is the stress exponent. By taking the logarithm of both sides and differentiating:

$$\frac{d \log \dot{\epsilon}}{d \log \sigma} = n \quad (\text{A3})$$

which implies that the slope of a linear fit through a plot of the strain rate versus the applied stress on a double logarithmic scale yields the stress exponent, n .

The temperature dependence of the strain rate assuming no changes in n with temperature is:

$$\dot{\epsilon} = K_Q \exp\left(\frac{-Q_a}{RT}\right) \quad (\text{A4})$$

where K_Q is a constant and Q_a is the activation energy. By differentiating and rearranging:

$$Q_a = -R \left(\frac{d \ln \dot{\epsilon}}{d \left(\frac{1}{T} \right)} \right) \quad (\text{A5})$$

thereby indicating that when $\ln \dot{\epsilon}$ is plotted versus $1/T$, the resulting slope multiplied by the universal gas constant (8.314 J/molK) gives the activation energy.

Appendix 2. Calculation of Critical Strain for Power Law Breakdown.

The power law breakdown regime is entered when the normalized shear stress exceeds a constant, i.e.:

$$\frac{\sigma_s}{\mu} \geq \frac{1}{\alpha'} \quad (\text{A6})$$

where μ is the shear modulus and σ_s is the shear stress. From Table 4.3, α' for copper is 794, thus providing a critical normalized shear stress of $1.259 \cdot 10^{-3}$.

The shear modulus is related to the Young's modulus E in the following manner:

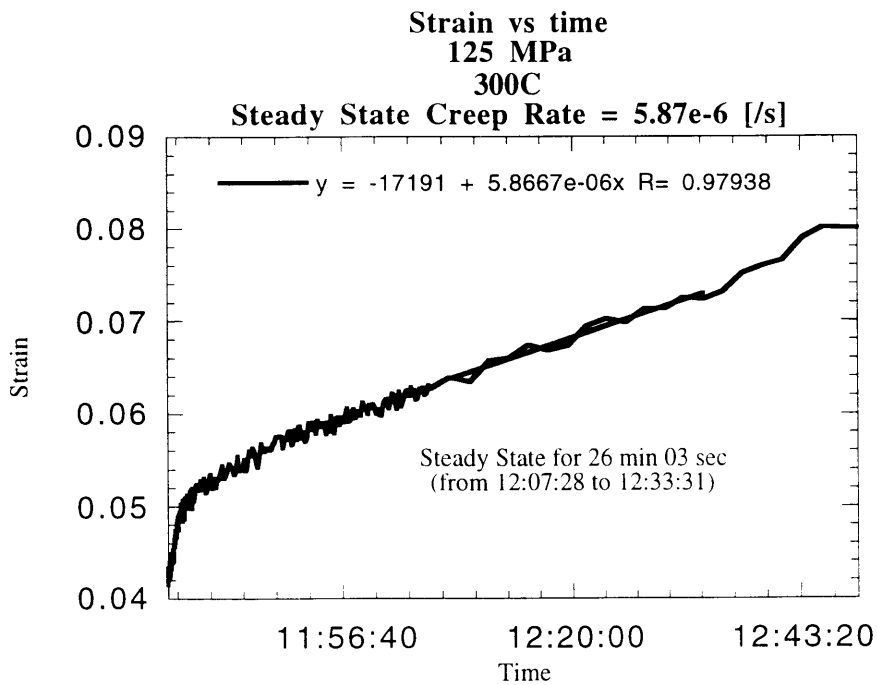
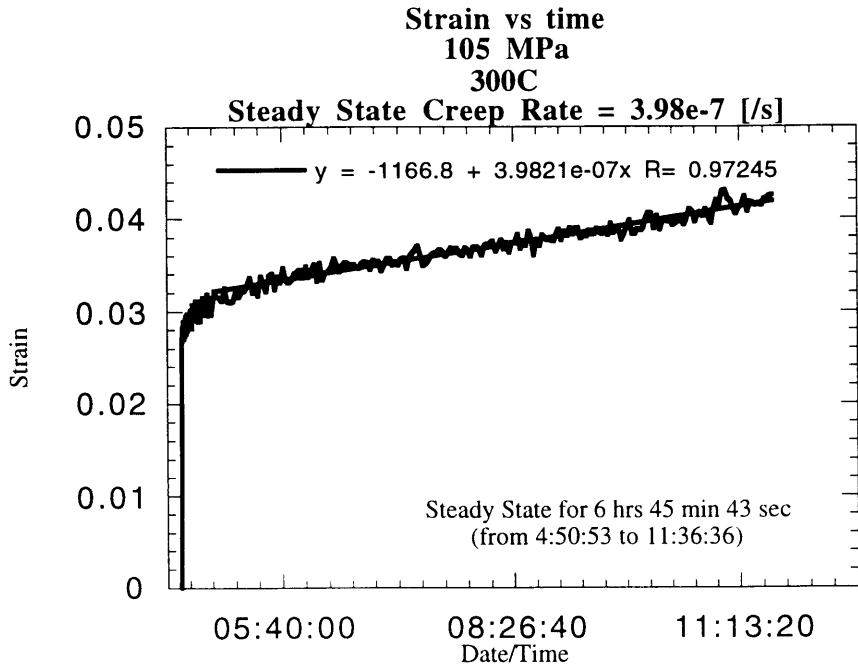
$$\mu = \frac{E}{\sqrt{3}} \quad (\text{A7})$$

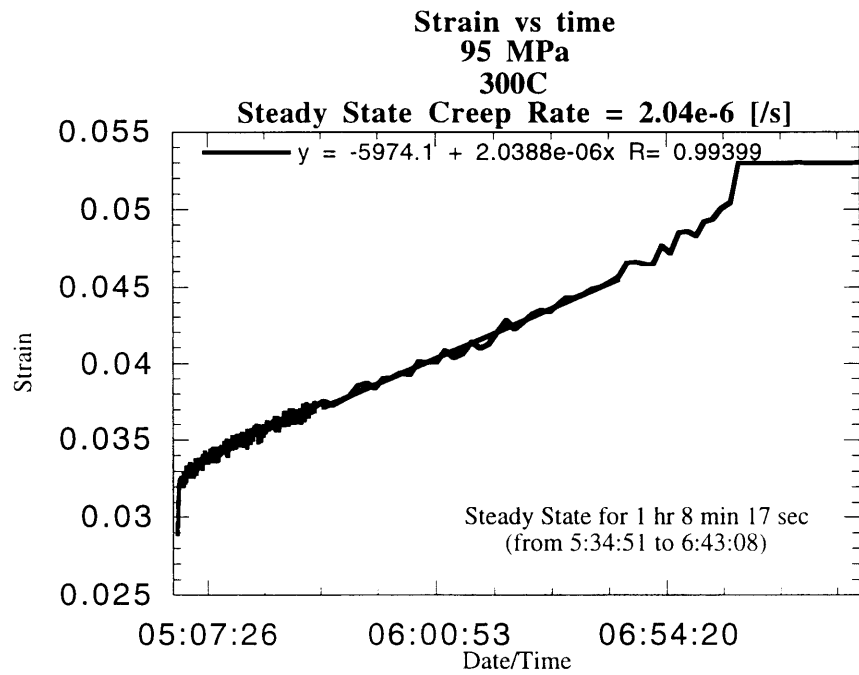
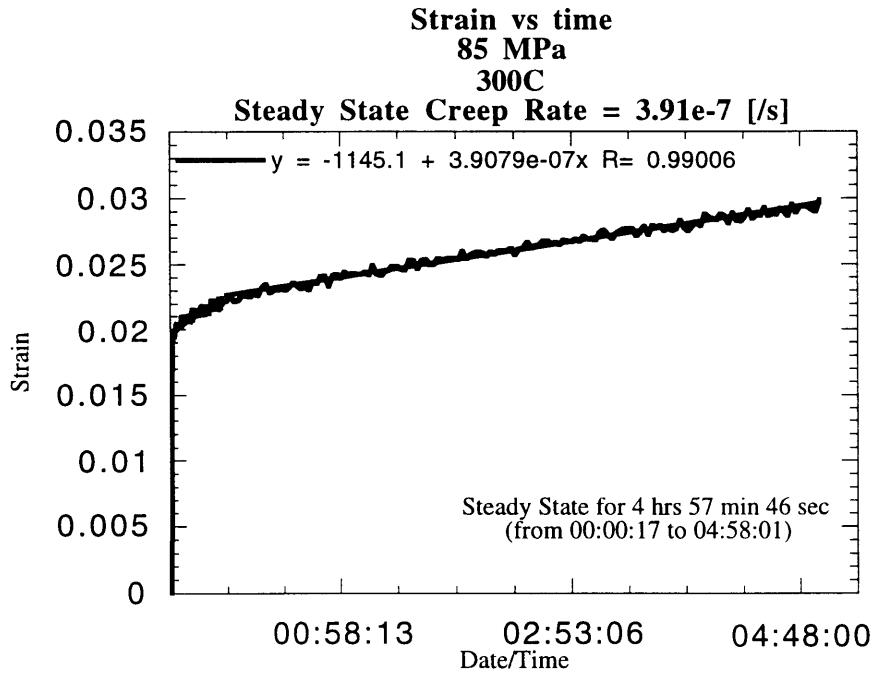
The temperature-dependent elastic moduli were listed in Table 4.2. Given these values, the critical shear stresses σ_s were calculated, and the critical applied tensile stress was determined from:

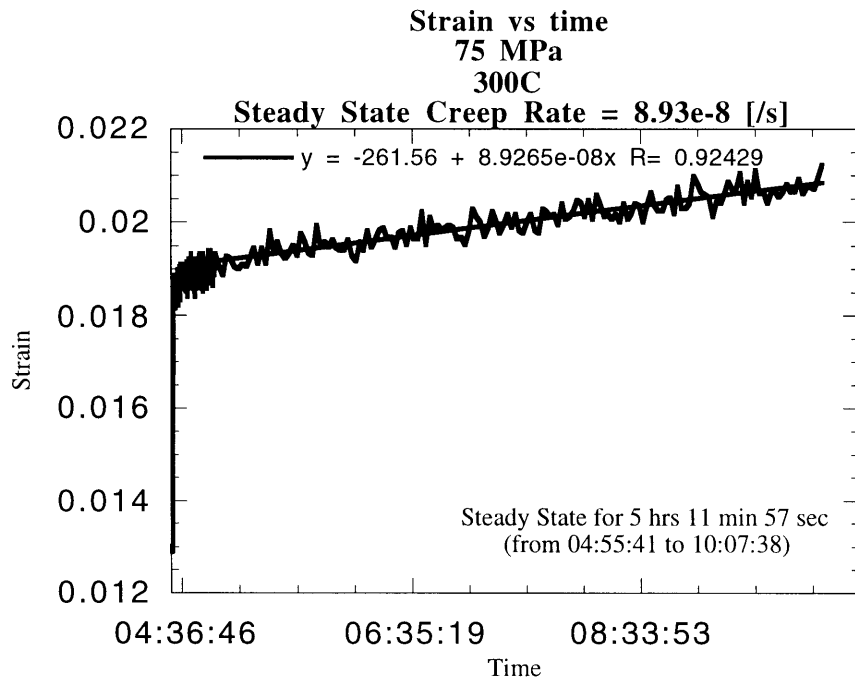
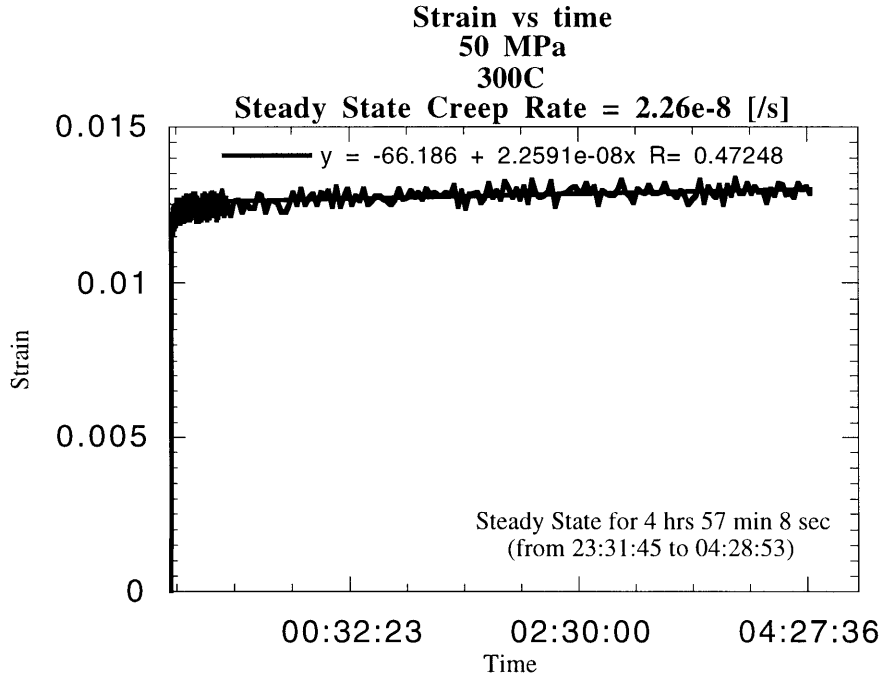
$$\sigma_A = \sigma_s \sqrt{3} \quad (\text{A8})$$

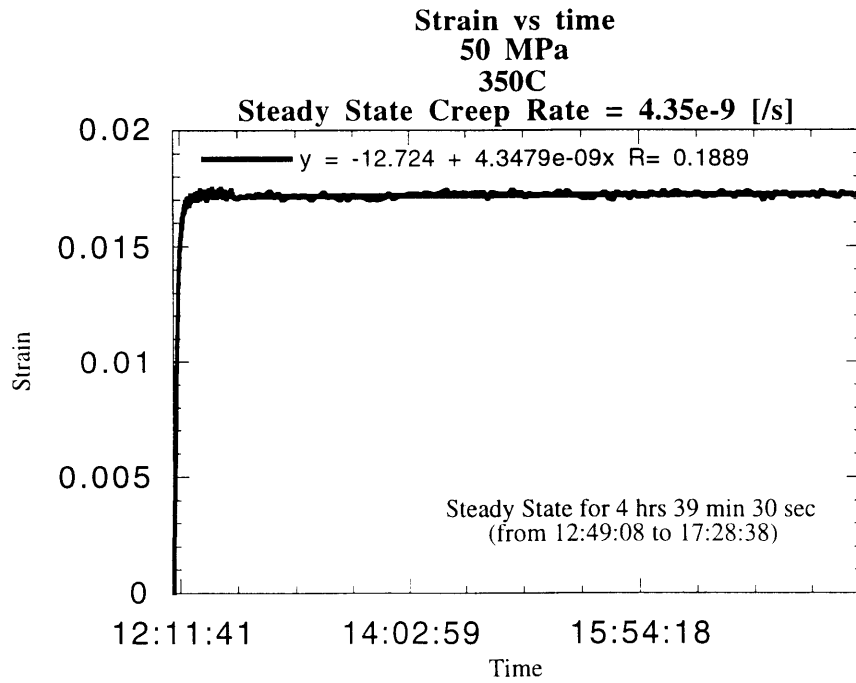
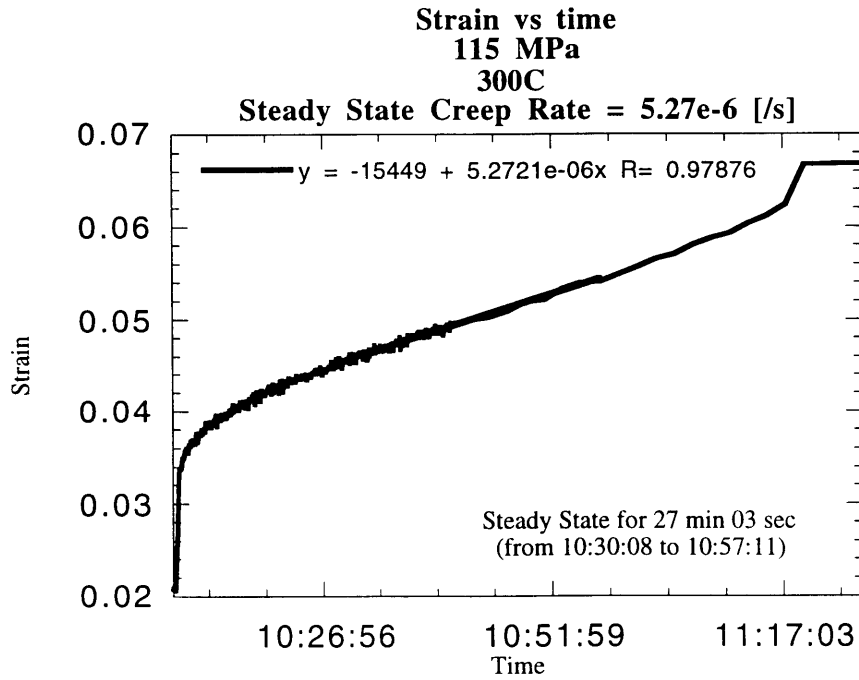
where σ_A is the applied stress. The critical applied tensile stresses were 82 MPa and 80 MPa, at 300°C and 350°C, respectively.

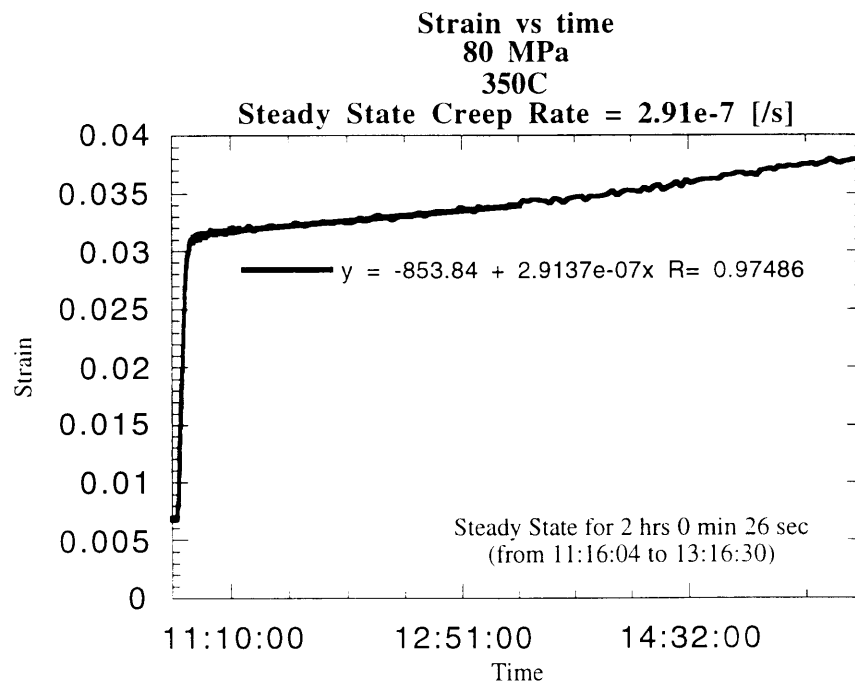
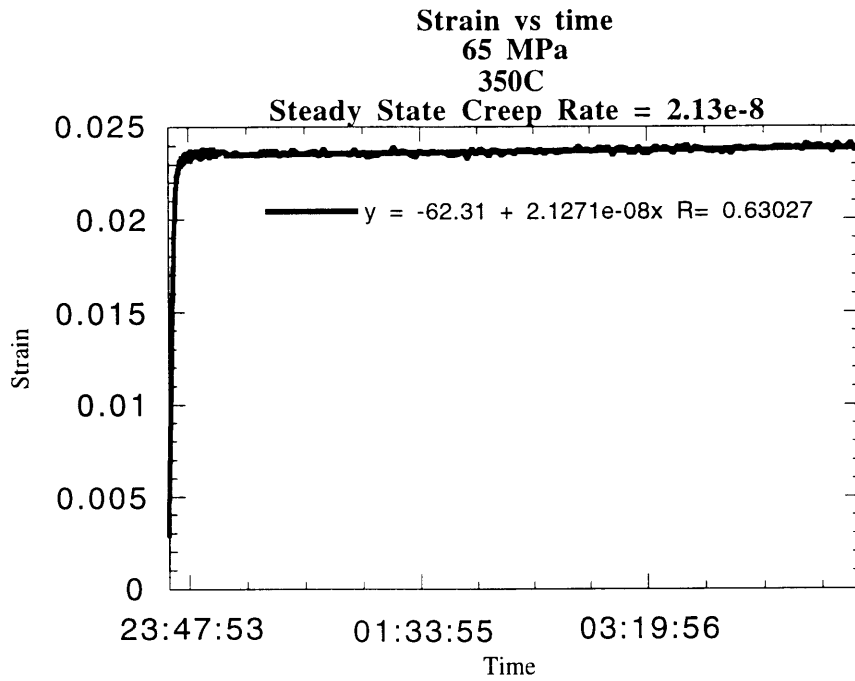
Appendix 3. Creep Curves Collected During Neutron Diffraction Experiments.



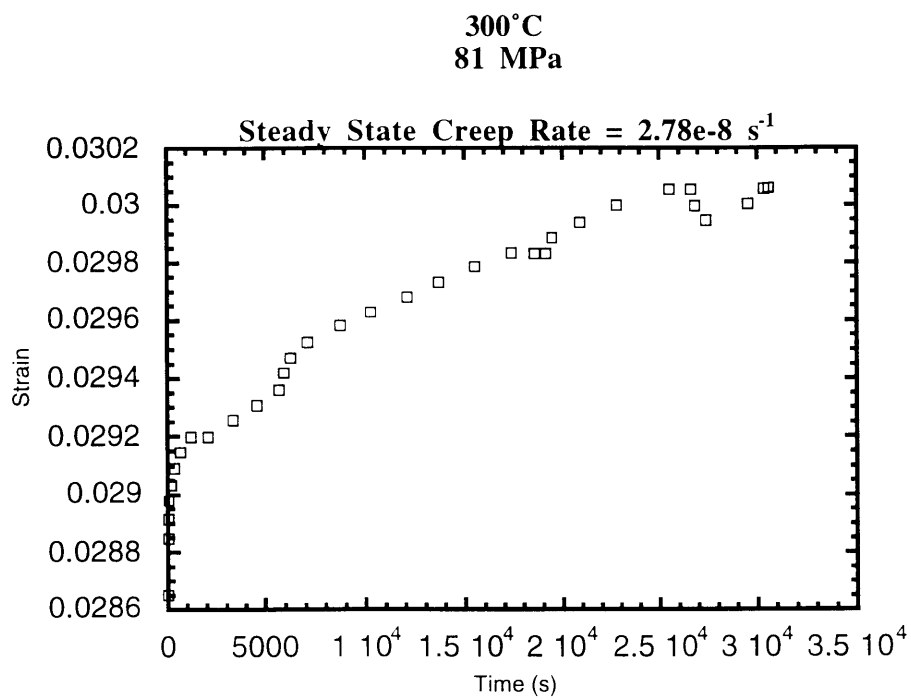
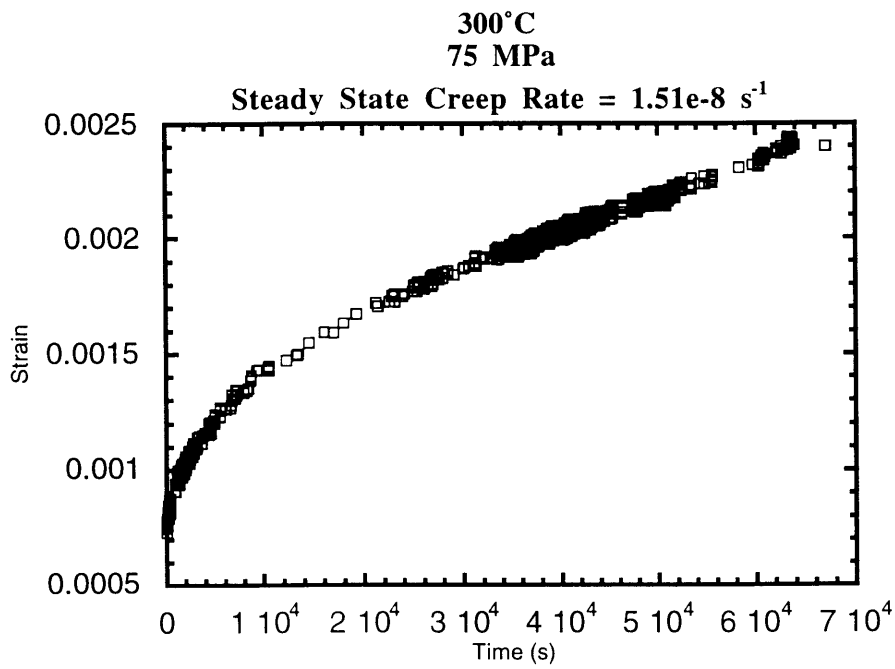




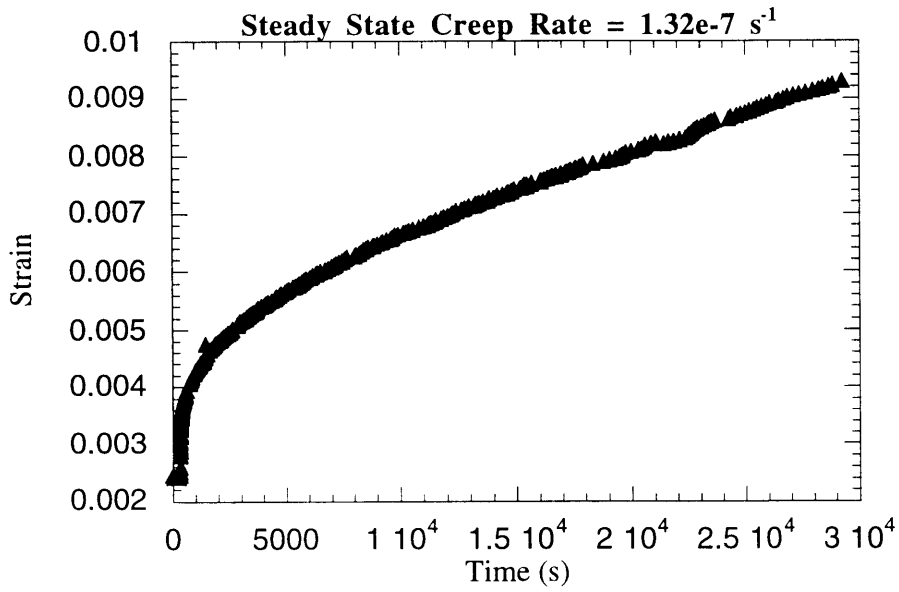




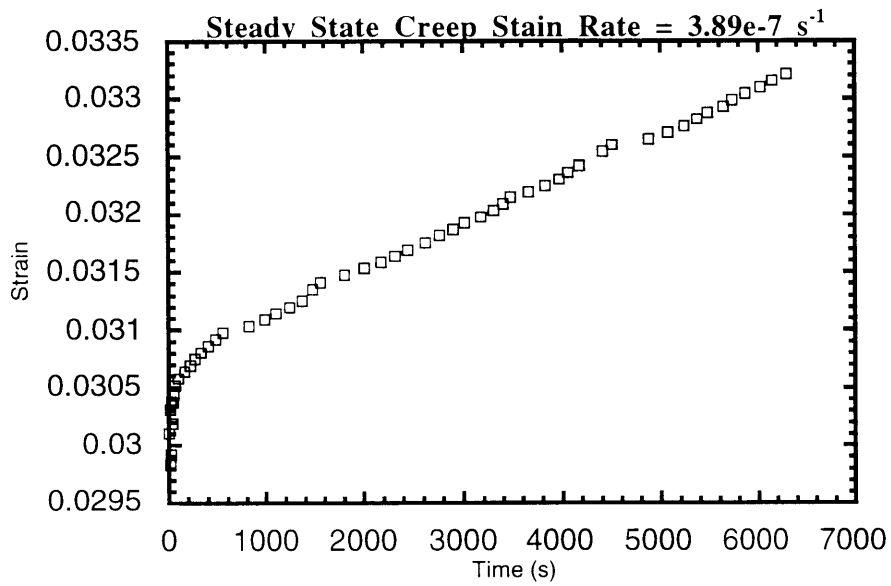
Appendix 4. Creep Curves From Conventional Creep Testing



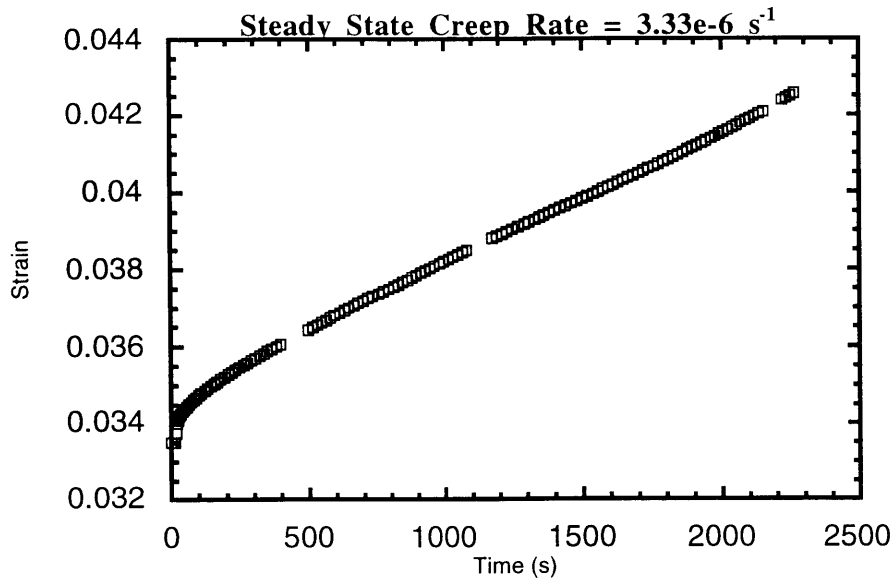
300°C
95 MPa



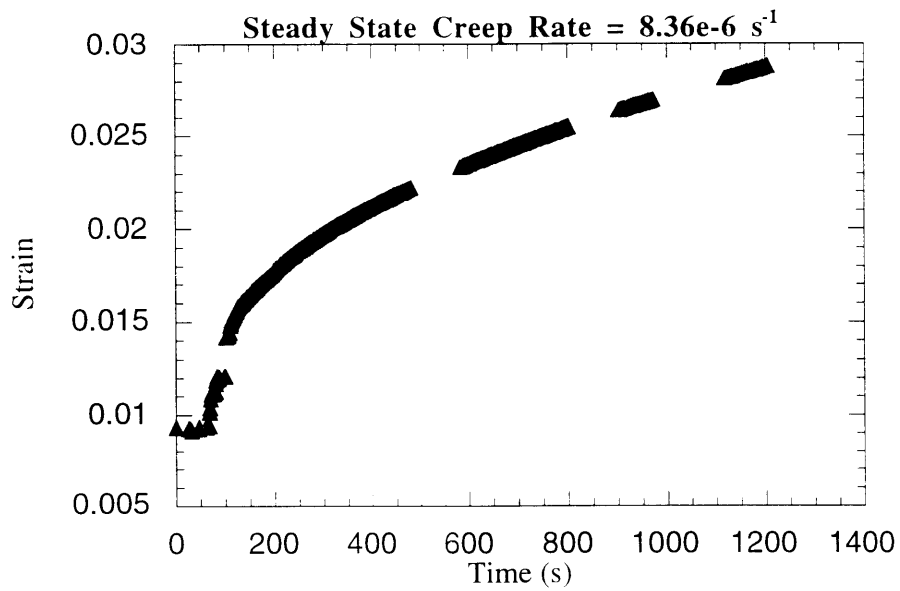
300°C
103 MPa



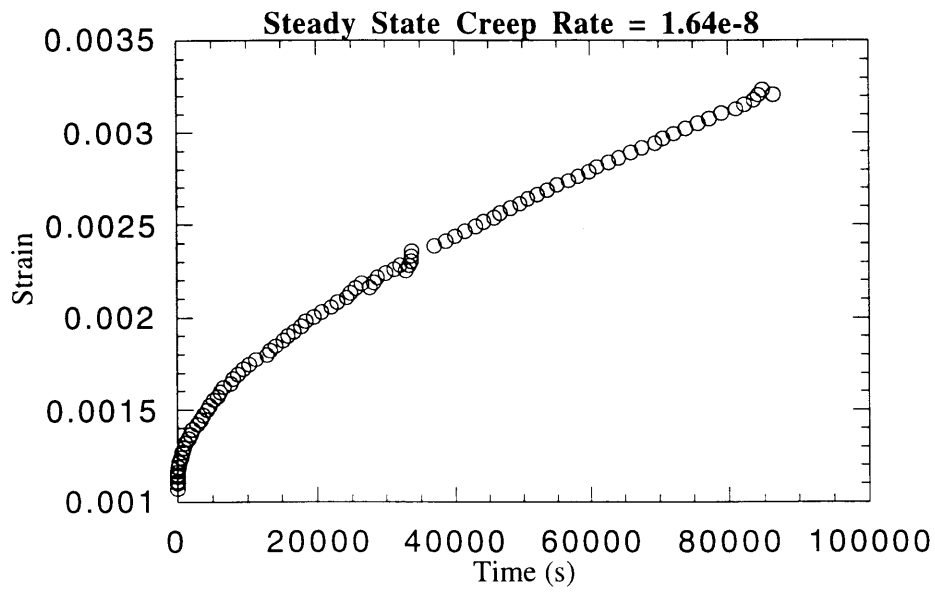
300°C
115 MPa



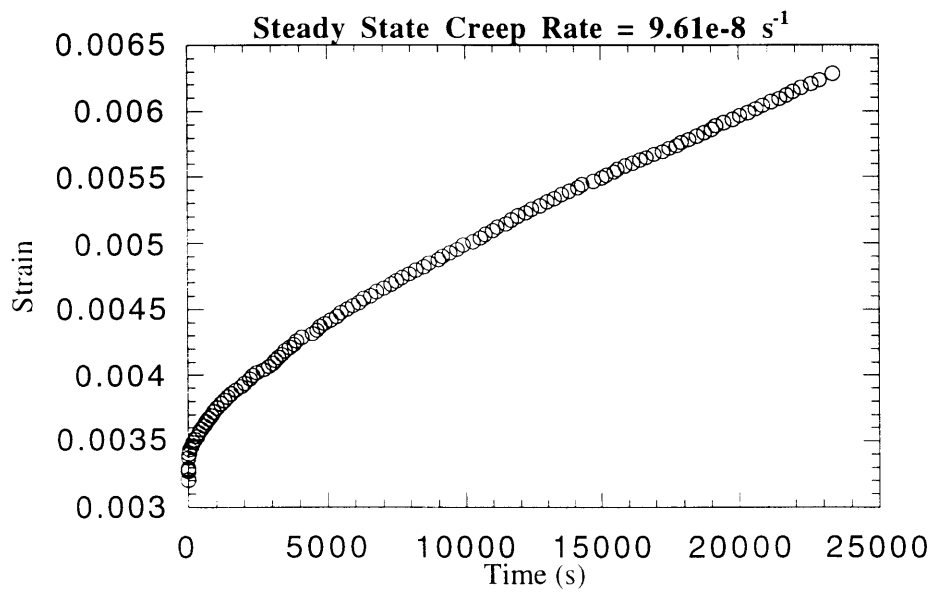
300°C
125 MPa



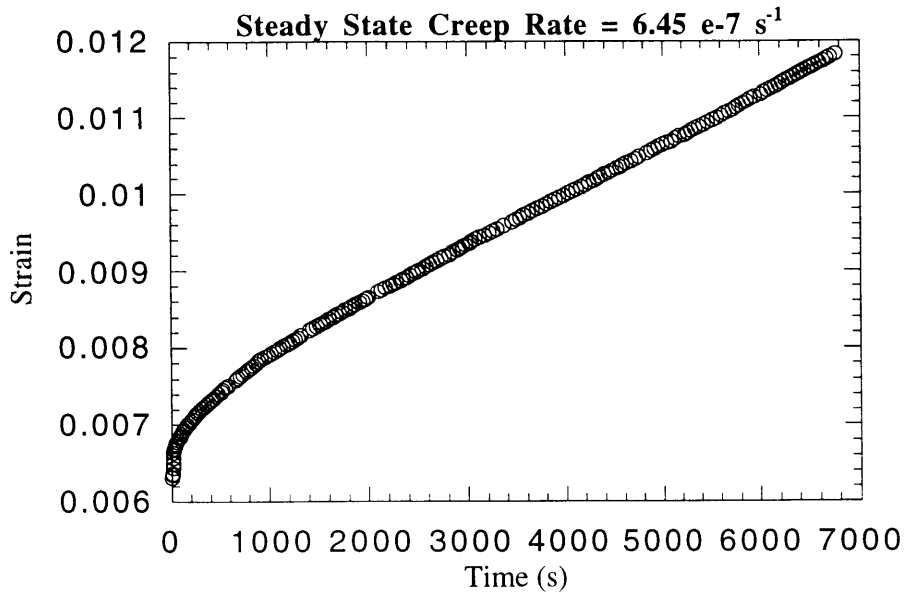
350°C
60 MPa



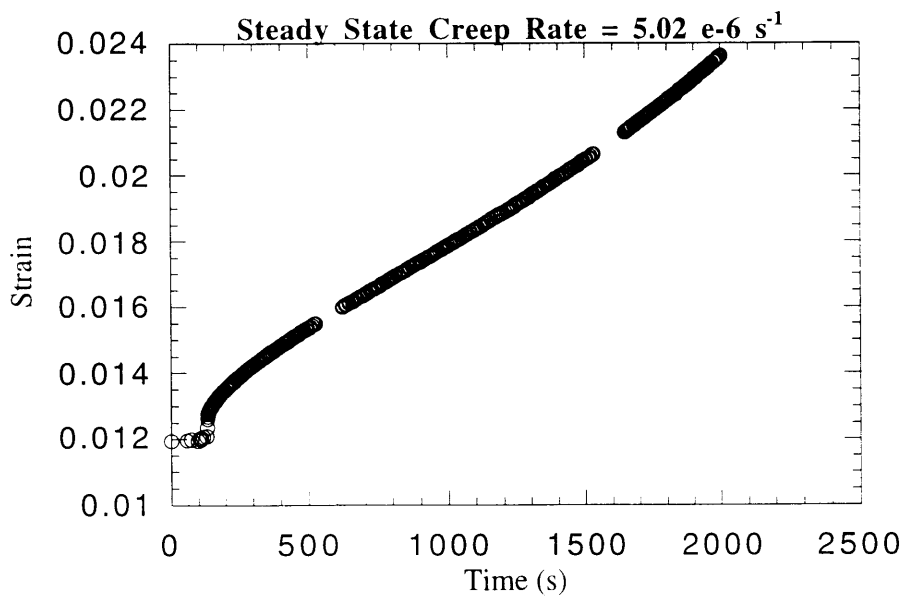
350°C
70 MPa



350°C
80 MPa



350°C
90 MPa



Appendix 5. Tables of Experimental Data.

A. Creep Data - Applied Stress and Strain Rates

300 Conv = Steady State Composite Creep Strain Rate (s^{-1}) at 300°C,
Conventional Test

350 Conv = Steady State Composite Creep Strain Rate (s^{-1}) at 350°C,
Conventional Test

300 Neutron = Steady State Composite Creep Strain Rate (s^{-1}) at 300°C,
Neutron Exp't.

350 Neutron = Steady State Composite Creep Strain Rate (s^{-1}) at 350°C,
Neutron Exp't.

Cu 300 Ashby = Steady State Creep Strain Rate (s^{-1}) at 300°C (Frost and Ashby
1982)

Cu 350 Ashby = Steady State Pure Cu Creep Strain Rate (s^{-1}) at 350°C (Frost and
Ashby 1982)

Stress (MPa)	300 Conv	350 Conv	300 Neutron	350 Neutron	Cu 300 Ashby	Cu 350 Ashby
50			2.2600e-08	4.3500e-09	2.82e-08	2.18e-07
60		1.6400e-08				
65				2.1300e-08		1.28e-06
70		9.6100e-08				
75	1.5100e-08		8.9300e-08		4.41e-07	
80		6.4500e-07		2.9100e-07		5.21e-06
81	2.7800e-08					
85			3.9100e-07		1.03e-06	
90		5.0200e-06				
95	1.3200e-07		2.0400e-06		2.20e-06	
103	3.8900e-07					
105			3.9800e-07		4.34e-06	
115	3.3300e-06		5.2700e-06		8.05e-06	
120						
125	8.3600e-06		5.8700e-06		1.42e-05	

*B. Neutron Cu and Mo Phase Strains and Stresses at RT, 300°C, and 350°C;
Axial Direction*

e = Strain

s = Stress (MPa)

Stress = Applied Stress (MPa)

	Stress	e-Cu-RT#1	e-Mo-RT#1	s-Cu-RT#1	s-Mo-RT#1	e-Cu-RT#2	e-Mo-RT#2
0	5.00	0.00e+00	0.00e+00	0.0000	0.0000	0.00000e+00	0.00000e+00
1	25.00	1.22e+02	1.05e+02	14.738	34.020		
2	45.00	2.54e-04	1.61e-04	30.734	52.164		
3	50.00					3.11000e-04	1.61000e-04
4	65.00	3.73e-04	2.36e-04	45.133	76.464	3.70000e-04	3.53000e-04
5	75.00						
6	80.00					4.40000e-04	5.09000e-04
7	85.00	4.70e-04	4.42e-04	56.870	143.21		
8	95.00						
9	105.00	5.33e-04	5.95e-04	64.493	192.78		
10	125.00	6.03e-04	7.80e-04	72.963	252.72		
11	140.00	6.45e-04	1.01e-03	78.045	325.62		
12	160.00	6.81e-04	1.25e-03	82.401	404.03		

s-Cu-RT#2	s-Mo-RT#2	e-Cu-300C	e-Mo-300C
0.0000	0.0000	0.00e+00	0.00e+00
37.631	52.164	3.46e-04	2.59e-04
44.770	114.37		
		5.39e-04	3.82e-04
53.240	164.92		
			4.56e-04
		6.98e-04	4.75e-04
		7.73e-04	6.36e-04
		1.03e-03	7.13e-04

	s-Cu-300C	s-Mo-300C	e-Cu-350C	e-Mo-350C	s-Cu-350C	s-Mo-350C
0	0.0000	0.0000	0.00000e+00	0.00000e+00	0.0000	0.0000
1						
2						
3	37.368	80.549	3.81000e-04	2.33000e-04	40.005	71.997
4			4.70000e-04	3.49000e-04	49.350	107.84
5	58.212	118.80				
6			5.89000e-04	4.68000e-04	61.845	144.61
7	51.408	141.82				
8	75.384	147.73				
9	83.484	197.80				
10	111.67	221.74				
11						
12						

*C. Neutron Cu and Mo Phase Strains and Stresses at RT, 300°C, and 350°C;
Transverse Direction*

e = Strain

s = Stress (MPa)

Stress = Applied Stress (MPa)

	Stress	e-Cu-RT#1	e-Mo-RT#1	s-Cu-RT#1	s-Mo-RT#1	e-Cu-RT#2	e-Mo-RT#2
0	5.0000	0.00000e+00	0.00000e+00	0.0000	0.0000	0.00000e+00	0.00000e+00
1	25.000	-7.46100e-05	-8.98900e-05	-9.0278	-29.124		
2	45.000	-1.25700e-04	-2.07700e-04	-15.210	-67.295		
3	50.000					-7.50000e-05	-1.31142e-04
4	65.000	-1.63000e-04	-1.75300e-04	-19.723	-56.797	-9.10000e-05	-2.37516e-04
5	75.000						
6	80.000					-1.06000e-04	-2.79431e-04
7	85.000	-2.15000e-04	-2.50300e-04	-26.015	-81.097		
8	95.000						
9	105.00	-2.56200e-04	-3.15100e-04	-31.000	-102.09		
10	115.00						
11	125.00	-3.00700e-04	-3.65600e-04	-36.385	-118.45		
12	141.00	-3.18600e-04	-4.31000e-04	-38.551	-139.64		
13	161.00	-3.60300e-04	-5.45000e-04	-43.596	-176.58		

s-Cu-RT#2	s-Mo-RT#2	e-Cu-300C	e-Mo-300C
0.0000	0.0000	0.00000e+00	0.00000e+00
-9.0750	-42.490	-1.05853e-04	-9.57283e-05
-11.011	-76.955		
		-1.39396e-04	-2.30445e-04
-12.826	-90.535		
		-1.56687e-04	-3.46727e-04
		-1.85001e-04	-3.25493e-04
		-1.33674e-04	-3.67038e-04
		-2.13081e-04	-3.62943e-04
		-1.72731e-04	-4.39621e-04

	s-Cu-300C	s-Mo-300C	e-Cu-350C	e-Mo-350C	s-Cu-350C	s-Mo-350C
0	0.0000	0.0000	0.00000e+00	0.00000e+00	0.0000	0.0000
1						
2						
3	-11.432	-29.772	-9.69413e-05	-1.48899e-04	-10.179	-46.010
4			-1.13419e-04	-1.78362e-04	-11.909	-55.114
5	-15.055	-71.668				
6			-1.19460e-04	-2.62949e-04	-12.543	-81.251
7	-16.922	-107.83				
8	-19.980	-101.23				
9	-14.437	-114.15				
10	-23.013	-112.88				
11	-18.655	-136.72				

BIBLIOGRAPHY

Allen, A.J., Bourke, M.A.M., David, W.I.F., et al, in Proceedings of the Second Conference on Residual Stresses I (Beck, Ed.), pp. 78-83, Elsevier, London, 1988.

Allen, A.J., Bourke, M.A.M., Hutchings, M.T., et al., In Residual Stresses in Science Technology (E. Macherauch, V. Hauk, Eds.), pp. 151-157, DGM Informationsgesellschaft mbH Verlag, Germany, 1987.

Allen, A.J., Hutchings, M.T., Windsor, C.G., Andreanni, C., Advances in Physics, Vol. 34, pp. 445-473, 1985.

Atkins, S.L., Gibeling, J.C., "A finite element model of the effects of primary creep in an Al-SiC metal matrix composite", Met. & Mat. Trans. A, Vol. 26A, pp. 3067-3079, 1995.

Bao, G., Hutchinson, J.W., McMeeking, R.M., "Particle reinforcement of ductile matrices against plastic flow and creep", Acta metall. mater., Vol. 39, No. 8, pp. 1871-1882, 1991.

Blackwood, A.W., Casteras, J.E., in ASM Metals Handbook, Vol. 2 (9th Ed.), ASM International, Metals Park, OH, 1987

Bourke, M.A.M., Goldstone, J.A., Stout, M.G., Needleman, A., "Characterization of Residual Stresses in Composites," in Fundamentals of Metal-Matrix Composites (Suresh, Mortensen, Needleman; Eds.), pp. 61-80. Butterworth-Heinemann, Boston, 1993.

Bourke, M.A.M., personal communication (1996).

Boyer, H.E., "Atlas of Stress-Strain Curves", ASM International, Metals Park, OH, 1987.

Briggs, J.Z., in ASM Metals Handbook, Vol. 2 (9th Ed.), ASM International, Metals Park, OH, 1987

Clyne, T.W., Withers, P.J., "An Introduction to Metal Matrix Composites", Cambridge University Press, Cambridge, Great Britain, 1993.

Davis, L.C., Allison, J.E., "Micromechanics effects in creep of metal matrix composites", Met. & Mat. Trans. A, Vol. 26A, pp. 3081-3089, 1995.

Dragone, T.L., Nix, W.D., "A numerical study of high temperature creep deformation in metal-matrix composites", Metal & Ceramic Matrix Composites: Processing, Modeling & Mechanical Behavior (Bhagat et al., Eds.), The Minerals, Metals & Materials Society, 1990.

Dunand, D.C., Derby, B., "Creep and Thermal Cycling" in Fundamentals of Metal-Matrix Composites (Suresh, Mortensen, Needleman; Eds.), Butterworth-Heinemann, Boston, 1993.

Gonzalez-Doncel, G., Sherby, O.D., "High temperature creep behavior of metal matrix aluminum-SiC composites", Acta metall. mater., Vol. 41, No. 10, pp. 2797-2805, 1993.

Hutchings, M.T., Nondestructive Test. Eval., Vol. 5, pp. 395-411, 1990.

Jansen, A.M., "The Mechanical Properties and Microstructure of Aluminum Containing 25 vol.% of 0.3 μm Alumina Particles", Ph.D. Thesis, MIT, 1996.

- Koczak et al., in *Fundamentals of Metal-Matrix Composites* (Suresh, Mortensen, Needleman; Eds.). Butterworth-Heinemann, Boston, 1993.
- Krajewski, P.E., Allison, J.E., Jones, J.W., "The influence of matrix microstructure and particle reinforcement on the creep behavior of 2219 aluminum", *Met. Trans. A*, Vol. 24A, pp. 2731-2741, 1993.
- Krawitz, A.D., Schmank, M.J., *Metall. Trans.* 13A, pp. 1069-1075, 1982.
- Larson, A.C., Von Dreele, R.B., "GSAS General Structural Analysis System User Manual", Los Alamos National Laboratory, Los Alamos, New Mexico, 1994.
- Lupis, C.H.P., "Chemical Thermodynamics of Materials", Prentice-Hall PTR, Englewood Cliffs, New Jersey, 1983.
- Majumdar, S., Singh, J.P., Kupperman, D., Krawitz, A.D., *J. Eng. Mater. Techn.*, Vol. 113, pp. 51-59.
- Meyers, M.A., Chawla, K.K., "Mechanical Metallurgy: Principles and Applications," Prentice-Hall, Englewood Cliffs, NJ, 1984
- Mishra, R.S., Pandey, A.B., *Metall. Trans.*, 21A, pp. 2089-2090, 1990.
- Mohamed, F.A., Park, K.-T., Lavernia, E.J., "Creep behavior of discontinuous SiC-Al composites", *Mat. Sci. & Eng.*, A150 (1992), pp. 21-35.
- Morimoto, T., Yamaoka, T., Lilholt, H., Taya, M., *Trans. ASME-J. of Eng. Mater. and Techn.*, 110, pp. 70-76, 1988.
- Nieh, T.G., "Creep rupture of a silicon carbide reinforced aluminum composite", *Met. Trans. A*, Vol. 15A, pp. 139-146, 1984.
- Nieh, T.G., Xia, K., Langdon, T.G., *J. Eng. Mater. Techn.*, 110, pp. 77-82, 1988.
- Pandey, A.B., Mishra, R.S., Mahajan, Y.R., "Creep behaviour of an aluminum-silicon carbide particulate composite", *Scripta Metallurgica et Materialia*, Vol. 24, pp. 1565-1570, 1990.
- Pickard, S.M., Derby, B., In *Developments in the Science and Technology of Composite Materials (ECCM3)*; (Bunsell et al., Eds.), pp. 199-204, Elsevier, Amsterdam, 1989.
- Povirk, G.L., Stout, M.G., Bourke, M.A.M., et al., *Scripta Metall. Mater.*, Vol. 25, pp. 1883-1888, 1991.
- Povirk, G.L., Stout, M.G., Bourke, M.A.M., et al., *Acta Metall. Mater.*, Vol. 40, pp. 2391-2412, 1992.
- Ravichandran, K.S., Seetharaman, V., "Prediction of steady state creep behavior of two phase composites", *Acta metall. mater.* Vol. 41, No. 12, pp. 3351-3361, 1993.
- Reed, T.B., "Free Energy of Formation of Binary Compounds", MIT Press, Cambridge, MA, 1971.
- Reed-Hill, R.E., Abbaschian, R., "Physical Metallurgy Principles", PWS - Kent Publishing Co., Boston, 1992.
- Shi, N., Arsenault, R.J., *J. Composites Tech. and Res.*, Vol. 13, pp. 211-225, 1991.
- Shi, N., Arsenault R.J., Krawitz, A.D., Smith, L.F., "Deformation Induced Residual Stress Changes in SiC Whisker Reinforced 6061 Al Composites, *Metall. Trans. A.*, Vol. 24A, pp. 187-196, 1992a.

- Shi, N., Arsenault R.J., Wilner, B., "A FEM Study of the Plastic Deformation Process of Whisker Reinforced SiC/Al Composites," *Acta Metall. Mater.* Vol. 40, pp. 2841-2854.
- Smithells, C.J., "Metals reference book," Butterworth-Heinemann, Boston, 1992.
- Subramanian, P.R., Laughlin, D.E., *Bull. Alloy Phase Diagrams*, Vol 11, No. 2, 1990.
- Suresh, S., Mortensen, A., Needleman, A., "Fundamentals of Metal Matrix Composites", Butterworth-Heinemann, Boston, 1993.
- Sørensen, N., "A planar model study of creep in particulate reinforced MMC's", in *Modeling of Plastic Deformation and its Engineering Applications*, Risø National Laboratory, Roskilde, Denmark, 1992, pp. 457-465.
- Sørensen, N., Needleman, A., Tvergaard, V., "Three-dimensional analysis of creep in a metal matrix composite", *Mat. Sci. & Eng.*, A158 (1992), pp. 129-137.
- Sørheim, O.J., personal communication (1994).
- Verdon, C., personal communication (1997).
- Withers, P., Stobbs., Pedersen, O.B., *Acta Metall. Mater.*, Vol. 37, pp. 3061-3084.